

Dissertation

Hadronic Contributions to the anomalous Magnetic Moment of the Muon

Tobias Göcke

Justus-Liebig-Universität Gießen
Fachbereich 07 – Mathematik und Informatik, Physik,
Geographie
Institut für Theoretische Physik
2012

Dekan: Prof. Dr. Christian Diller

1. Gutachter: Prof. Dr. Christian Fischer (JLU Gießen)

2. Gutachter: Priv.-Doz. Dr. Lorenz von Smekal (TU Darmstadt)

Contents

Danksagung	v
1 Introduction	1
2 The anomalous magnetic moment—an overview	3
2.1 The history of the leptonic $g - 2$	3
2.2 Experimental techniques	5
2.3 Basic concepts	6
2.4 Standard Model prediction for the muon $g - 2$	8
3 Theoretical foundations	14
3.1 Generating functionals and Quantum Field Theory	14
3.2 Functional integral equations of QCD and QED	17
3.3 Symmetries and Ward-Takahashi identities	27
4 Working with a truncation of the DSE's of QCD	31
4.1 Rainbow-ladder truncation	31
4.2 Beyond rainbow-ladder truncation	40
5 Hadronic vacuum-polarisation	42
5.1 Basic definitions	42
5.2 Results	46
6 Hadronic light-by-light scattering	55
6.1 The PS-exchange contribution	61
6.2 The quark loop contribution	66
6.3 Results: meson-exchange contribution	69
6.4 Quark loop: comparing DSE to NJL	71
6.5 Results: Quark loop contribution	79
7 Discussion	89
A Euclidean conventions	93
B Derivation of the photon DSE	96

C	Derivation of Ward-Takahashi identities	99
D	Dispersion relations	102
E	Quark-photon vertex	104
F	Photon four-point function	107

Danksagung

Zuallererst danke ich meinem Betreuer Prof. Christian Fischer dafür, dass er mir diese spannende Arbeit ermöglicht hat. Des Weiteren genoss ich die motivierende und doch entspannte Atmosphäre in der Arbeitsgruppe. Ein großer Dank geht auch an Dr. Richard Williams, der mir besonders in der frühen und mittleren Phase meiner Arbeit eine große Hilfe war. Das mündete schließlich in eine effektive Zusammenarbeit unter Kollegen, von der ich auch weiterhin profitiere.

Ich erinnere mich gerne an die Zeit im 'Kinderzimmer' in Darmstadt. Von lustigen Unterhaltungen, über tiefe philosophische Erkenntnisse bis hin zu argumentativen Grabenkämpfen war alles dabei, und nichts davon möchte ich missen. Hervorzuheben sind hier Klaus Heckmann und Christian Kellermann. Des Weiteren Jens Müller, der nicht Teil des Kinderzimmers war, aber immer für intensive Erörterungen physikalischer und weltlicher Themen zu Verfügung stand.

Mein Dank gilt weiterhin der Gießener Arbeitsgruppe, die aus der Darmstädter Gruppe erwachsen ist, für die angenehme Atmosphäre. Besonderer Dank gilt hier Stefan Strauss für regelmäßige anregende Unterhaltungen sowie private Unternehmungen. Es scheint unmöglich ein Thema zu finden, über das er kein Buch besitzt oder das ihn nicht wenigstens peripher interessiert.

Weiterhin danke ich Sabrina für die Unterstützung und dafür mich daran zu erinnern, dass das Leben nicht nur aus Physik besteht (Der Beweis steht allerdings noch aus).

1 Introduction

The Standard Model (SM) of elementary particles is among the greatest achievements of twentieth century physics. It is by far the best founded theoretical description of our universe at the microscopic level. The huge number of experimental tests that it has passed have led to the confidence that physicists put in this framework. A famous example is the prediction of the magnetic moment of the electron g_e to an experimentally confirmed precision of one part in a billion.

The Standard Model incorporates three different fundamental interactions of nature: the electromagnetic, the weak and the strong force. An observable that is sensitive to all of these is the anomalous magnetic moment of the muon (a_μ). As the anomalous magnetic moment of the electron it has been measured and predicted to a high degree of accuracy. Contrary to the latter one, however, a comparable precision is harder to achieve, both for theory and experiment. On the theoretical side this is due to the fact that the strong force yields sizable contributions to the muon magnetic moment, whereas in the electron case it is not relevant at the current precision. Contrary to the electromagnetic force that is responsible for the current value of a_e alone, the strong force is not accessible withing perturbation theory at the scales relevant to the problem.

One reason for the great interest in the anomalous magnetic moment of the muon lies in the deviation between the Standard Model prediction and experiment. This might be taken as a hint towards new physics beyond the SM, however confirmation requires a further reduction of the uncertainty of both theory and experiment. This reduction requires non-perturbative methods on the theoretical side, since the major uncertainty lies in hadronic contributions to a_μ caused by the strong interaction.

In this work the framework of Dyson-Schwinger equations (DSE's) is utilized to obtain theoretical predictions for the hadronic contributions to a_μ . Several features of the DSE's make them very suited for this calculations. First of all they are applicable to non-perturbative quantum field theoretical processes in general. In particular they provide a description of the relevant Greens functions that is valid on all scales such that no scale-matching procedure is needed like in effective theories. This feature is especially important for one of the hadronic contributions, the so called hadronic light-by-light scattering.

This thesis is organized as follows. In the chapter 2 we give an overview over the main

topic, that is the anomalous magnetic moment of the muon. The reader will find a short historical overview, a short account of the main experimental techniques, the introduction of some elementary concepts and an overview over the different Standard Model contributions to a_μ . Furthermore we compare the experimental results to theoretical predictions.

This is followed by an introduction of the theoretical body in chapter 3 that underlies the work presented later on. There we shortly introduce the concept of quantum field theory (QFT) in general and define the tower of Dyson-Schwinger equations that are the main theoretical tool. We also discuss some Green's functions of the theory and highlight some of their properties that are relevant in order to understand steps we undertake in later chapters. Finally we discuss chiral symmetries of QCD and the local gauge symmetry of QED in a manner that is relevant to the truncation that is used for the numerical calculations. In addition this chapter establishes our notation, some conventions and the definition of certain Green's functions. Going from the general to the particular we discuss the specific truncation of QCD (and QED) that we use in some detail in chapter 4. We explain the model assumptions made, discuss the equations that have to be solved numerically more explicitly and comment on the properties of the applied truncation and highlight some descriptions and predictions of physical observables.

The main results of this work are the numerical treatment of the two most relevant hadronic contributions to the muon anomaly. These are the hadronic vacuum polarisation (HVP) which is presented in chapter 5 and the hadronic light-by-light scattering contribution (LBL) to be discussed in chapter 6.

Finally we give a concluding discussion in the last chapter 7, followed by the appendix.

2 The anomalous magnetic moment—an overview

In the current chapter we give a short overview over the basic ideas, the current status as well as a quick account of the historical development of the subject.

2.1 The history of the leptonic $g - 2$

The present section is to a large extent based on Refs. [1, 2, 3] where more details can be found. Not all original sources will be cited here explicitly in particular those which are easily available online. Instead we refer to the just mentioned overviews .

The history of leptonic magnetic moments is closely tight to the dawn of Quantum Electro Dynamics (QED) and to the development of the Standard Model in general. The early history of QED and the rôle of the electron $g - 2$ is explained in Ref. [4] in detail. In order to explain the observed anomalous Zeeman effect an intrinsic electron spin of two times the expected value ($g = 2$) was postulated in 1925 [5]. On the theoretical side it was Dirac who predicted the same number from the equation that bears now his name in 1928 [6, 7]. It comes out naturally in the relativistic description of spin 1/2 particles there. The fact that the magnetic moment has an anomalous part which is the deviation from this result ($g - 2$) was only realized much later in 1947. For the first time the result $g - 2 \neq 0$ was confirmed experimentally by the authors of Ref. [8]. The first theoretical understanding came from Schwinger in 1948 [9] who calculated the leading contribution $(g - 2)/2 \simeq \alpha/2\pi \simeq 0.00116$ with α the fine structure constant. Intriguingly the true value deviated about 0.12% from the Dirac result. This was (together with the understanding of the Lamb shift) an important milestone on the way that lead to the establishment of QED and the foundation of modern elementary particle physics [4]. The anomalous magnetic moment of the electron has been an interesting observable that played a prominent rôle ever since. Today this quantity has been calculated up to order α^5 [10] and agrees with experiment on the order of 10^{-12} in terms of g [11].

It was realized in 1956 by Berestetskii (see e.g. [1, 3]) that the sensitivity of the anomaly

$\delta a/a$ for a certain lepton l scales as

$$\frac{\delta a_l}{a_l} \propto \frac{m_l^2}{\Lambda^2}, \quad (2.1)$$

where m_l is the lepton mass and Λ is a scale that characterises a given contribution. That is either a heavy particle or a hypothetical cutoff of the theory. We will see later that Λ represents the scale of the strong interaction Λ_{QCD} , the scale of the weak interaction M_W or even a scale of physics beyond the SM. It was realized that due to the dependence of (2.1) on the lepton mass, that the muon anomaly a_μ is much more sensitive than a_e . Since $m_\mu/m_e \simeq 200$ we get a factor of 40 000! Back then it was, however, unclear how to measure a_μ because nobody knew how to produce polarized muons. Soon after, the occurrence of parity violation in the Weak Interaction was noted [12]. This led to the remarkable idea that the decay of pions $\pi \rightarrow \mu + \nu$ would produce muons with positive helicity on the one hand. In the same work also the subsequent muon decay $\mu \rightarrow e + \nu + \nu$ (almost 100% branching ratio) was analysed and found to produce electrons (or positrons) with final momentum highly correlated to the muon spin. These two observations are key to the measurement of the muon g -factor since one can produce polarized muons that can interact with a magnetic field in a definite way, and the second observation allows for a determination of the muon spin via a measurement of the momentum of the decay electron. In fact first observations soon confirmed $g_\mu \simeq 2$. The sensitivity to so far unknown physics, expressed via Eq. (2.1) generated big interest in a_μ so that further measurements were conducted. Theorists apparently expected deviations from QED to be found.

Several experimental investigations were performed at CERN. This started with the CERN cyclotron (1958-1962), followed by a muon storage ring (1962-1968) reaching a precision of 270 ppm. A deviation from the SM of 1.7σ was found which resulted in a deepening and rethinking of the theoretical investigations. Higher order loop calculations were undertaken and triggered the development of algebraic computer systems. A second muon storage ring at CERN started operation (1969-1976) which finally reached a precision of 7 ppm. Here the hadronic vacuum polarisation contribution became important for the first time. The strategy of using the heavy muon as a probe for high scales paid off. The up-to-date experiment is the E821 at Brookhaven that operated until 2003 and reached 0.54 ppm accuracy. At this precision the leading hadronic diagram is a highly significant contribution. In addition the significance of the weak contributions is now established. In this way the anomalous magnetic moment of the muon is an observable that tests the whole SM resulting in a sustained significant deviation between theory and experiment. On the theoretical side two different hadronic contributions are the limiting factors. Since the corresponding calculations are outside the realm of the otherwise remarkably successful perturbation theory, non-perturbative methods are needed.

A new experiment at Fermilab is on the way [13] which aims at a precision of 0.14 ppm. On the side of theory the availability of finally mature non-perturbative techniques such as lattice QCD [14, 15, 16, 17, 18] and the functional methods used in this work [19, 20, 21] rise hope that the QCD contribution to the muon $g - 2$ can be brought under control with the necessary precision.

2.2 Experimental techniques

In the present section we give a short overview over the basic experimental ideas that have been applied in the muon $g - 2$ experiments as for example the most recent E821 at Brookhaven. The experimental principles are explained in detail in [1, 3].

As already said before parity violation in the weak interaction is a key element in these experiments. The muons are produced from decaying pions. Due to P violation the muons appear mainly in one helicity and are thus highly polarised. They are injected into a storage ring, where they circulate subject to a magnetic field that is oriented perpendicular to the plane of the ring. The frequency of that circular motion is

$$\omega_c = \frac{eB}{m_\mu c \gamma}, \quad (2.2)$$

where B is the magnetic field strength, c the speed of light and γ is the Lorentz factor. Due to the magnetic field the spin of the muons that is initially parallel to direction of flight starts precessing with frequency

$$\omega_s = \omega_c + \frac{eB}{m_\mu c} a_\mu. \quad (2.3)$$

It happens to be the case that the precession frequency differs from the cyclotron frequency ω_c by a term that is proportional to the anomalous magnetic moment a_μ . This makes this experimental techniques a smoking gun for this observable. In reality it happens that also an electric field E is needed to keep the muons inside the ring, so that Eq. (2.3) receives additional terms. These terms, however, cancel at the 'magic energy' of $\gamma m_\mu c \simeq 3.098 \text{ GeV}$.

The muons now decay into positrons after many circulations in the storage ring, where the weak force causes a correlation between the spin of the μ^+ and the positron momentum. The e^+ is thus a probe of the muon spin. Several detecting devices along the ring measure the decay positrons and an oscillating signal can be extracted. The oscillation frequency is just the desired

$$\omega_a = \frac{eB}{m_\mu c} a_\mu, \quad (2.4)$$

from which the anomaly a_μ can be extracted. The recent result is [22, 23]

$$a_\mu^{\text{Exp}} = 116\,592\,089(63) \times 10^{-11}. \quad (2.5)$$

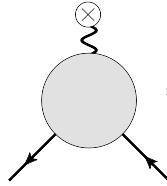
2.3 Basic concepts

In this subsection we give basic ideas and definitions relevant to the subject of $g - 2$. The g -factor is part of the definition of the magnetic moment $\vec{\mu}$ of a particle. It is proportional to the particles spin \vec{S}

$$\vec{\mu} = \gamma \vec{S} = \frac{e}{2m} g \vec{S}, \quad (2.6)$$

with the proportionality constant γ called the gyromagnetic ratio. The latter is in addition given in terms of the charge e and the mass m of that particle. For a magnetic moment caused by orbital motion $g = 1$ and for the case of a spin $1/2$ particle $g = 2$ as can be seen from the Dirac-equation [6] when quantum corrections are neglected.

In a relativistic quantum field theory the magnetic moment is part of the lepton-photon-vertex which is the basic quantity describing the interaction in e.g. Quantum Electrodynamics (QED) the theory of the electromagnetic interaction. Following [24] we define



$$= \bar{u}(p') \left[F_1(q^2) \gamma_\alpha + i F_2(q^2) \frac{\sigma_{\alpha\beta} q^\beta}{2m_\mu} \right] u(p) = \bar{u}(p') \Gamma_\alpha u(p), \quad (2.7)$$

where q is the photon momentum, m_μ is the muon mass and $\sigma_{\alpha\beta} = i/2[\gamma_\alpha, \gamma_\beta]$. The spinor of the incoming/outgoing on-shell muon is denoted as $u(p)$. In addition we have the Dirac form factor F_1 and the Pauli form factor F_2 . In order to obtain the anomalous magnetic moment we consider the matrix element \mathcal{M} with a classical background gauge field $A_\mu^{\text{cl}}(x) = (0, \vec{A}(\vec{x}))$

$$\mathcal{M} = e \bar{u}(p') \Gamma_\mu u(p) A_\mu^{\text{cl}}(\vec{q}), \quad (2.8)$$

which represents a purely magnetic interaction with magnetic field strength $B^k(\vec{q}) = -i\epsilon^{kij} q^i A_{cl}^j(\vec{q})$. The matrix element can be interpreted as originating from an effective potential

$$\vec{V}(\vec{x}) = -(\vec{\mu}) \cdot \vec{B}(\vec{x}).$$

Using now the decomposition from Eq. (2.7) in the expression for the matrix element (2.8) and taking the non-relativistic limit

$$u(p) \approx \sqrt{m} \begin{pmatrix} (1 - \vec{p} \cdot \vec{\sigma}/2m) \xi \\ (1 + \vec{p} \cdot \vec{\sigma}/2m) \xi \end{pmatrix},$$

as well as $q \rightarrow 0$, the identification

$$\langle \vec{\mu} \rangle = \frac{e}{m} [F_1(0) + F_2(0)] \left\langle \frac{\vec{\sigma}}{2} \right\rangle, \quad (2.9)$$

can be made as is detailed in Ref. [24]. Here $\vec{\sigma}$ is a three-vector of Pauli matrices and $\vec{\sigma}/2$ corresponds to the spin operator. Comparison with Eq. (2.6) yields

$$g = 2 [F_1(0) + F_2(0)] = 2 + 2F_2(0), \quad (2.10)$$

where the last line holds since $F_1(0) = 1$ is demanded by charge renormalisation. We thus have

$$a_\mu := F_2(0) = \frac{g - 2}{2}. \quad (2.11)$$

Any contribution to a_μ can thus be obtained by the following procedure

- Write down the Feynman-diagram corresponding to a certain contribution to the vertex (2.7)
- Project onto the Pauli form-factor $F_2(q^2)$
- Take the limit $q \rightarrow 0$

A possible projection method is [25]

$$a_\mu = \frac{1}{48m_\mu} \text{Tr} \left[(\not{p} + m_\mu) [\gamma_\alpha, \gamma_\beta] (\not{p} + m_\mu) \left(\frac{\partial}{\partial q_\alpha} \Gamma_\beta \right) \right] \Big|_{q \equiv 0}, \quad (2.12)$$

where the derivative of the vertex Γ_β appears. Instead the naïve Projector for Eq. (2.7)

$$P_\alpha = \frac{m_\mu^2}{q^2(q^2 + 4m_\mu^2)} \gamma_\alpha - i \frac{m_\mu(2m_\mu^2 - q^2)}{q^2(q^2 + m^2)^2} (p + p')_\alpha, \quad (2.13)$$

can be used

$$a_\mu = \lim_{q \rightarrow 0} \text{Tr}[P_\alpha \Gamma_\alpha(q)]. \quad (2.14)$$

This procedure has the disadvantage of being singular in the limit $q \rightarrow 0$. Furthermore it is numerically more demanding since more independent variables have to be taken into account in the numerical integration. This can be easily understood by recognising the fact that in the case of (2.13, 2.14) the photon momentum is never exactly $q = 0$ and so has to be treated properly as an external scale. This leaves certain scalar products with internal loop variables non-zero which vanish in the case $q = 0$ as is the case with procedure (2.12). The latter is the method we mostly apply while the naïve method serves as a welcome cross check.

2.4 Standard Model prediction for the muon $g - 2$

Here we give an overview over the QED, weak and hadronic contributions to a_μ . The overview is based on [1] where more details can be found.

QED and weak contributions. The dominant contribution to the muon anomalous magnetic moment comes from QED. These contributions have been calculated up to five-loop order (α^5). The leading contribution is the famous Schwinger result coming from



with

$$a_\mu^{\text{QED,leading}} = \frac{\alpha}{2\pi},$$

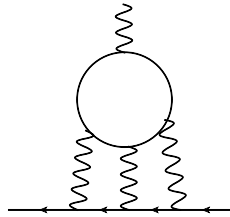
which accounts for about 99% of the anomaly. This contribution is obviously universal since it does not depend on the lepton mass m_l ($l = e, \mu, \tau$). At two loop order there are nine diagrams of which three are non universal. These include lepton loops and turn out to depend on the ratio of masses of the external flavour and the flavour in the lepton loop. Here the first distinction between electron and muon becomes visible. The two-loop result for the muon is

$$a_\mu^{\text{QED,2-loop}} = 413217.621(14) \times 10^{-11}. \quad (2.15)$$

The three-loop contribution incorporates already 72 diagrams giving rise to

$$a_\mu^{\text{QED,3-loop}} = 30141.902(1) \times 10^{-11}. \quad (2.16)$$

This result is dominated by the electron-loop light-by-light contribution



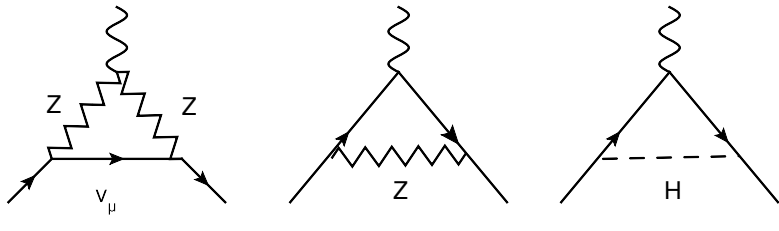
The four-loop calculation is a formidable task since it involves more than thousand diagrams of which most are only known by means of numerical analysis today. The result is

$$a_\mu^{\text{QED,4-loop}} = 380.807(25) \times 10^{-11}, \quad (2.17)$$

which is still significant given the experimental precision obtained today. The contributions up to order α^5 have been evaluated recently [26] giving rise to

$$a_{\mu}^{\text{QED},5\text{-loop}} = 753.29(1.04) \left(\frac{\alpha}{\pi}\right)^5 \approx 5 \times 10^{-11}. \quad (2.18)$$

The precise experimental result also necessitates the knowledge of weak contributions. The leading order contributions, which involve Z and Higgs bosons, in graphical representation are



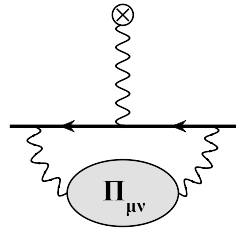
$$(2.19)$$

The weak contributions are known up to two-loop level [27]

$$a_{\mu}^{\text{weak}} = 153.5(1.0) \times 10^{-11}, \quad (2.20)$$

the result is quoted from [2].

Hadronic contributions. The leading order hadronic contributions is the hadronic vacuum polarisation (HVP) that looks like the Schwinger diagram with an additional hadronic one-particle irreducible photon self-energy insertion



This contributions is considered in detail in chapter 5 which is why we won't discuss it here at length. An up to date evaluation of the leading order yields [28]

$$a_{\mu}^{\text{HVP,LO}} = 6949.1(58.2) \times 10^{-11}. \quad (2.21)$$

This leading hadronic contribution is quite significant at the present precision. Since it involves non-perturbative QCD its calculation from first principles is involved. Fortunately it can be extracted from experiment via dispersion relations (see again chapter 5 as well as app. D)

such that it is known in an essentially model independent way. Nevertheless it yields the most dominant contribution to the overall SM uncertainty. This uncertainty is dominated by experimental input from $e^+e^- \rightarrow \text{hadrons}$ data. A systematic improvement is thus possible by refined measurements [28, 2]. Higher order HVP corrections that contain several hadronic photon self-energy insertions contribute [28]

$$a_\mu^{\text{HVP,HO}} = -98.4(1.0) \times 10^{-11}. \quad (2.22)$$

Their contribution to the error is not that important at the moment.

The most problematic contribution finally, is the hadronic light-by-light contribution (LBL)

$$. \quad (2.23)$$

Contrary to the HVP contributions it can not be related to experiment in a straightforward way so far. Existing calculations have been carried out in hadronic models such as the Nambu–Jona-Lasinio model (NJL) [29, 30, 31] or approaches based on effective low energy descriptions of QCD involving hadronic degrees of freedom [32, 33, 34, 35]. In addition this quantity has been looked at from the view point of vector-meson dominance models [36, 37]. No complete calculation based on first principles is available at the moment. Different groups having worked in the effective hadronic picture agreed recently on the result [38]

$$a_\mu^{\text{LBL,EFT}} = 105(26) \times 10^{-11}. \quad (2.24)$$

This is the outcome of an effort that lasted more than a decade. This contribution is in the long run probably the most problematic contribution since contrary to HVP a systematic estimate of the uncertainty is so far not possible. The main purpose for the present work is to start a detailed analysis of the LBL contribution using the method of Dyson-Schwinger equations. We believe that this method is superior to effective field theory in at least two ways. First of all the DSE method needs no scale separation and no separate treatment of high-energy and low-energy contributions of QCD. The approach deals with the fundamental degrees of freedom of QCD, which are quarks and gluons, in such a way that a unified description is possible at all scales. This is extremely useful since the LBL contribution involves the photon four-point function, an object that depends on several external scales thus making a unique scale separation impossible. The other advantage is that the DSE method takes the full tensor structure and momentum dependence of all calculated n -point functions into account, contrary to e.g. the NJL-model that works with a reduced tensor basis and simplified momentum dependence of Green's functions in most cases.

Comparison of theory and experiment. Finally we summarize the theoretical contributions and compare to experiment in table 2.1. In order to obtain the theoretical uncertainty the uncertainties of the separate contributions are added in quadrature. It can be seen that the QED contributions are by far dominant. The leading order hadronic contribution (the leading order hadronic vacuum polarisation LOHVP) is one hundred times larger than the error and is thus of high significance. In fact it is the largest non-QED contribution. The light-by-light (LBL) contribution is significant but only slightly larger than the overall uncertainty which shows that further improvement is mandatory here. In total the hadronic contributions strongly dominate the error of the theoretical prediction. The weak contribution is rather small but already significant at the given precision. The error is supposed to be well under control. The comparison with experiment reveals a deviation that corresponds to 3σ here. Depending on the numbers used for the hadronic contributions and their errors the significance varies slightly [1, 2, 28]. The uncertainty of the comparison arises from the ones from Standard Model prediction and experiment added quadratically.

In order to keep up with the experimental development expected to take place in the current decade [13] the theoretical treatment of the hadronic contributions has to be improved. As already mentioned for the HVP results this depends on experimental input that was used to obtain the contributions shown in table 2.1. For LBL more elaborate theoretical frameworks have to be used. One obvious choice is of course lattice QCD. First promising results for HVP are already available [14, 15, 16]. The calculation of LBL is, however, a difficult and expensive task on the lattice. We thus believe that improved non-perturbative methods like Dyson-Schwinger equations (DSEs) are an important tool for the systematic reduction of the theoretical uncertainty.

In fact DSEs have been successfully used together with the lattice in different research fields. They are complementary to each other in certain ways but they can be formulated in the same language, that is on the level of Euclidean momentum space Green's functions. This allows one to combine these approaches at different intermediate steps. For example can lattice calculations of vertices be used as input for propagator DSE's and thus improve or validate certain truncations. The DSE's can, on the other hand, be used in certain parts of parameter space that are sometimes hard to reach on the lattice. Examples are the infinite volume limit, the chiral limit or simply higher order Green's functions that might be numerically demanding. In addition the DSEs, through typically formulated in Euclidean space time, can be continued back to time-like momenta. And finally there is no problem to convey DSE studies at finite chemical quark potential.

In the case of pure Yang-Mills theory at vanishing temperature, for example, successful truncations exist that compare quantitatively to the propagators of gluon and ghost in Landau gauge calculated from the lattice [39, 40, 41, 42, 43]. Also the properties of quarks derived from self-consistent Yang-Mills input has been investigated [44] as well as unquench-

ing effects caused by dynamical quarks that feed back into the gluon [45]. Furthermore, at times where the lattice calculations had strong finite volume artifacts DSEs were used as a guide to address these [46]. A similar case is the question of the precise value of the critical number of fermion flavours in QED_3 , a theory that exhibits a quantum phase transition as a function of the number of fermion flavours [47]. There DSE studies revealed that a deviation between lattice and continuum results could be explained by finite volume effects [48]. Another example is the QCD phase diagram. Here lattice calculations suffer from the sign problem that so far excludes any direct calculations at finite quark chemical potential. Here DSE studies have been conveyed that themselves use the gluon propagator as a temperature dependent input in the quark DSE [49]. Even a back feeding of the quarks into the gluon degrees of freedom (unquenching) has been possible such that extrapolations of lattice results into the region of non-vanishing chemical potential is possible [50]. This nicely shows that lattice results can be combined with functional continuum methods, such as DSEs and functional renormalisation group equations, in a very effective and productive way.

A similar approach is possible in the case of LBL. Since the calculation of the contribution a_μ^{LBL} is a very demanding task several combined methods seem worthwhile. Of course the lattice could aim for a calculation of the hadronic four point function $\Pi_{\mu\nu\alpha\beta}$ shown as blob in Eq. 2.23. This would be very helpful since it would allow for an essentially model independent definition of the hadronic piece in an otherwise perturbative QED diagram. On the other hand any lattice artifacts that could lurk in $\Pi_{\mu\nu\alpha\beta}$ would have to be brought under control. Examples might be infinite volume extrapolations and extrapolations to physical quark masses. Here DSEs offer themselves as a tool to study these. The hadronic four-point tensor will be described later on in terms of the quark photon vertex and the quark propagator of QCD. As input to calculate these, assumptions about the quark gluon interactions in the form of the quark-gluon vertex have to be made in the currently applied truncation scheme. Lattice calculations of these correlation functions, either as truncation improvements for the case of the quark-gluon vertex, or as comparisons to DSE results for the quark and the quark-photon vertex would be interesting possibilities to improve our understanding of the relevant Green's functions. The hadronic photon four-point tensor can be defined in terms of these 'lattice improved' two and three point functions and compared to direct lattice calculations of the whole object. There are thus several possibilities to combine the two approaches on different hierarchies leading to non-trivial cross checks and improved understanding. In fact first ideas in this direction have been considered.

New physics contributions. The deviation between theory and experiment seen in table 2.1 raises the question what kind of contributions could fill the gap if it is truly there. This can be taken as a constraint for new physics beyond the Standard Model. There have been detailed studies of possible contributions from super-symmetric extensions of the Standard

Table 2.1: Here we give a list of the contributions to a_μ . Shown are different theoretical contributions: QED (up to five loop), weak contributions up to two loops, the leading order hadronic vacuum polarisation (LOHVP), higher orders (HOHVP), the hadronic light by light contribution (LBL), the total Standard Model prediction, the experimental value and finally the comparison between theory and experiment. This gives rise to a 2.9σ deviation if these particular results for LOHVP and LBL are chosen. The error of the SM contribution has been obtained by adding in quadrature the theoretical parts. Analogously the uncertainty of the difference between theory and experiment corresponds to the ones of the two separate ones added in quadrature.

Contribution	$a_\mu \times 10^{11}$	%
QED	116 584 718.1 (0.2)	99.994%
weak	153.2 (1.8)	0.00013%
QCD LOHVP	6 949.1 (58.2)	0.006%
QCD HOHVP	−98.4 (1.0)	0.00008%
QCD LBL	105 (26)	0.00009%
Standard Model	116 591 827.0 (64)	100%
Experiment	116 592 089 (63)	
Exp-Theo	262 (89)	

Model, see for example [51, 52, 53], where it was found that these extensions have the potential to explain a contribution of the required size.

3 Theoretical foundations

In the present chapter the theoretical foundation as well as the methodological prerequisites will be laid out. Since we want to analyse hadronic contributions to an electro-magnetic (EM) observable we introduce below Quantum Chromo Dynamics (QCD) the theory of the strong interaction as well as Quantum Electro Dynamics (QED) which describes the EM properties of the muon in the case of interest.

We will summarize the basics of quantization and renormalization of these theories. The idea of Dyson-Schwinger Equations (DSE's) will be introduced afterwards, followed by a consideration of the appearance of mesons as quark bound states in QCD and the corresponding Bethe-Salpeter Equations (BSE's) for these bound states. In addition we will discuss how electromagnetic properties of hadronic states and hadronic quantities in general can be described via the combined action of QCD and QED. A central object in that respect is the fully dressed quark-photon vertex that describes the coupling of quarks to photons taking into account non-perturbative effects from QCD. In the end we will consider some aspects of the chiral symmetry of QCD and the $U(1)$ gauge symmetry of QED that are relevant for the current investigations.

3.1 Generating functionals and Quantum Field Theory

In the present work two of the quantum field theories (QFT's) that constitute the Standard Model (SM) are relevant. These are Quantum Chromo Dynamics (QCD) the theory of the strong interaction and Quantum Electro Dynamics (QED) the theory of the electro magnetic interaction. They are usually formulated as path integrals, for an introduction see [24, 54]. Let $S[\phi]$ be the action involving the field $\phi(x)$ with x being a shorthand for a space time coordinate x_μ , $\mu \in \{0, 1, 2, 3\}$. The quantum theory of that particular theory is then defined via the generating functional or path integral $Z[J]$

$$Z[J] = \int \mathcal{D}\phi \, e^{-S[\phi] + \int_x J\phi}, \quad (3.1)$$

Here the functional integration measure is heuristically meant to be an integration over the field variable at every spacetime point $\phi(x_i)$

$$\int \mathcal{D}\phi = \lim_{N \rightarrow \infty} \int \prod_{i \in N} d\phi(x_i), \quad (3.2)$$

and $\int_x J\phi$ is a shorthand for $\int d^4x J(x)\phi(x)$ where J is a classical source for the field ϕ . Note that Eq. (3.1) is defined on a Euclidean space-time (\mathbb{R}^4). Throughout this work Euclidean QFT will be used. The conventions are summarized in appendix A.

In Eq. (3.1) the field ϕ is to be considered as a placeholder for different fields. Since we are interested in QCD and QED this will be a fermion field (denoted as ψ) and a gauge field (A_μ) transforming under the $U(1)$ or $SU(3)$ gauge groups.

QCD Lagrangian. QCD is based on the gauge principle for the gauge group $SU(3)$ together with the demand for Poincaré invariance and renormalisability. The Lagrangian of QCD in Euclidean metric reads:

$$\mathcal{L}_{\text{QCD}} = \bar{\psi}(\not{D} + m)\psi + \frac{1}{2}\text{Tr}_c[F_{\mu\nu}F_{\mu\nu}], \quad (3.3)$$

where the covariant derivative is $D_\mu = \partial_\mu - igA_\mu$ and the Lie algebra valued gauge field is $A_\mu = A_\mu^a t^a$. The t^a are the generators of the Lie algebra $su(3)$ with Lie bracket $[t^a, t^b] = if^{abc}t^c$. Here the f^{abc} are the totally screw symmetric structure constants. In the fundamental representations the generators are given in terms of the Gell-Mann matrices as $t^a = \frac{\lambda^a}{2}$. They fulfill $\text{Tr}[t^a t^b] = \delta^{ab}/2$. The Field strength tensor is defined in analogy to the usual curvature tensor as $-igF_{\mu\nu} = [D_\mu, D_\nu]$ which results in

$$F_{\mu\nu} = \partial_\mu A_\nu - \partial_\nu A_\mu - ig[A_\mu, A_\nu]. \quad (3.4)$$

The Lagrangian in Eq. (3.3) is invariant under local $SU(3)$ gauge transformations generated by an element $g(x)$ in the fundamental representation:

$$\psi \rightarrow g\psi \quad A_\mu \rightarrow gA_\mu g^{-1} - (\partial_\mu g)g^{-1}. \quad (3.5)$$

This invariance generates a redundancy, since all gauge fields that differ only by gauge transformations give the same contribution to gauge independent observables and describe the same physics. In the path integral in Eq. (3.1) we currently integrate over all field configuration, including all redundant ones. This is not a problem for gauge invariant observables. In order to have well defined gauge dependent Green's functions (e.g. propagators), however, we have to fix a gauge. This is done with the standard Feddeev-Popov procedure [55].

Renormalization. Since quantum field theories in four dimensions usually suffer from infinities that appear in the loop integrals of many matrix elements, a renormalization prescription has to be applied. QCD is a multiplicatively renormalisable theory that has only a finite number of primitive divergent correlation functions. These are exactly the propagators and vertices that appear in Eqs. (3.3) and (3.6) such that no counter terms involving new operators are needed.

The renormalized Euclidean action of QCD fixed in the covariant gauge family is given as

$$\begin{aligned} \mathcal{S}_{\text{QCD}} = \int_x \Big\{ & Z_\psi \bar{\psi}(\not{\partial} + Z_m m)\psi + \frac{Z_A}{2} A_\mu^a [-\partial^2 \delta_{\mu\nu} + (1 - \frac{1}{\xi}) \partial^\mu \partial^\nu] A_\nu^a + Z_c \bar{c} \partial^2 c \\ & - i Z_{\psi A} g \bar{\psi} \not{A} \psi + g Z_{cA} f^{abc} \bar{c}^a \partial_\mu (A_\mu^c c^b) \\ & + g Z_{3A} f^{abc} (\partial_\mu A_\nu^a) A_\mu^b A_\nu^c + \frac{g^2}{4} Z_{4A} f^{abc} f^{ade} A_\mu^b A_\nu^c A_\mu^d A_\nu^e \Big\}, \end{aligned} \quad (3.6)$$

with the renormalization constants for the quark Z_ψ , the gluon Z_A , the ghost Z_c , the ghost-gluon vertex Z_{cA} , the quark-gluon vertex $Z_{\psi A}$ and the three and four gluon vertices $Z_{3/4A}$. By definition the vertex renormalisation constants are related to the field and charge renormalisation constants

$$Z_{3A} = Z_g Z_A^{3/2} \quad Z_{4A} = Z_g^2 Z_A^2 \quad Z_{cA} = Z_g Z_c Z_A^{1/2} \quad Z_{\psi A} = Z_g Z_\psi Z_A^{1/2}, \quad (3.7)$$

where Z_g is the charge renormalisation. To get QED we neglect the gauge boson self interaction in (3.6) as well as all terms containing the ghost field (of course the gauge group that is left implicit in the remaining terms has to be chosen correct). The gauge-fixed Lagrangian (3.6) is invariant under BRST transformations [56]. From the Slavnov-Taylor identities (STI's) that follow from BRST symmetry the relations

$$\frac{Z_{4A}}{Z_{3A}} = \frac{Z_{3A}}{Z_A} = \frac{Z_{cA}}{Z_c} = \frac{Z_{\psi A}}{Z_\psi} \quad (3.8)$$

between the renormalization constants can be deduced [57, 58]. Furthermore in Landau gauge ($\xi = 0$) the condition

$$Z_{cA} = 1, \quad (3.9)$$

can be maintained due to the non-renormalization of the ghost-gluon vertex in the $\overline{\text{MS}}$ -scheme [58]. This can be carried over to a momentum subtraction scheme, the miniMOM scheme [59], which is suitable for numerical investigations.

In order to define the Green's functions of the theory we need the source terms for the corresponding fields as indicated in Eq. (3.1)

$$\int_x \left\{ J_\mu A_\mu + \bar{\eta} \psi + \bar{\psi} \eta + \bar{\sigma} c + \bar{c} \sigma \right\}. \quad (3.10)$$

Correlation functions. The path integral shown in Eq. (3.1) is the generating functional of correlation functions

$$G^n(x_1, \dots, x_n) = \langle \phi_1 \dots \phi_n \rangle = \frac{\delta}{\delta J(x_1)} \dots \frac{\delta}{\delta J(x_n)} Z[J], \quad (3.11)$$

where G are full Green's functions. The connected Green's functions are obtained from the functional $W[J] = \ln Z[J]$. Especially relevant for the rest of this thesis are the one-particle-irreducible (1PI) vertex functions generated by the effective action Γ :

$$\Gamma[\Phi] := \sup_J \left(\int_x J\Phi - \ln Z[J] \right), \quad (3.12)$$

which due to the Legendre transformation is now a functional of the expectation value of the field $\Phi = \langle \phi \rangle$. In particular one gets $\delta\Gamma/\delta\Phi = J$. The supremum operation in Eq. (3.12) implicitly defines the source as a functional of this field expectation value $J[\Phi]$. The standard functional formalism used here is explained in detail in [60, 54].

3.2 Functional integral equations of QCD and QED

In the present section we introduce the concept of Dyson-Schwinger equations as a method to obtain non-perturbative definitions of 1PI n -point correlation functions. We further elaborate on Bethe-Salpeter equations (BSE's) as descriptions of bound state amplitudes and vertex equations. In particular we present some examples of integral equations that are relevant for the picture underlying the employed truncation. On top of that we give precise definitions of those equations that have to be solved for the scope of the present work. These are the building blocks we need in order to be able to calculate the hadronic contributions to the muon $g - 2$. Further details can be found in [60, 61].

The generating functional of Dyson-Schwinger Equations. We start with the observations that the integral of a total derivative vanishes

$$0 = \int \mathcal{D}\phi \frac{\delta}{\delta\phi} e^{-S+J\phi} = \left[J - \frac{\delta S}{\delta\phi} \left[\frac{\delta}{\delta J} \right] \right] Z[J], \quad (3.13)$$

which is just the second fundamental theorem of calculus, given that surface terms are zero. Using $W[J] = \ln Z[J]$

$$0 = e^{-W} \left[\frac{\delta S}{\delta\phi} \left[\frac{\delta}{\delta J} - J \right] \right] e^W = \left[\frac{\delta S}{\delta\phi} \left[\frac{\delta W}{\delta J} + \frac{\delta}{\delta J} \right] - J \right].$$

Utilizing $\delta\Gamma/\delta\Phi = J$ and the chain rule

$$\frac{\delta W}{\delta J} = \Phi \qquad \frac{\delta}{\delta J} = \left(\frac{\delta J}{\delta\Phi} \right)^{-1} \frac{\delta}{\delta\Phi} = (\Gamma'')^{-1} \frac{\delta}{\delta\Phi}, \quad (3.14)$$

we arrive at

$$\frac{\delta\Gamma[\Phi]}{\delta\Phi} = \frac{\delta S[\phi]}{\delta\phi} \Big|_{\phi=\Phi+(\Gamma'')^{-1}\frac{\delta}{\delta\Phi}}. \quad (3.15)$$

The expression in Eq. (3.15) is the generating functional of DSE's. Written explicitly

$$\Gamma'' = \frac{\delta^2\Gamma[\Phi]}{\delta\Phi_x\delta\Phi_y} = \left(\frac{\delta^2 W}{\delta J_x\delta J_y} \right)^{-1},$$

is the inverse of the full propagator of the theory. In Eqs. (3.12 - 3.15) multiplication of functions always means contraction of all indices (space and internal) as well as integration over common space-time arguments. The generating functional allows for a convenient derivation of DSE's for arbitrary n -point functions (see e.g. Ref. [62]). In order to obtain these further derivatives $\delta/\delta\Phi$ have to be applied to Eq. (3.15) and the sources have to be set to zero in the end. In this way the theory is represented as an infinite tower of equations. Since a complete solution of those is impossible a more modest way has to be pursued. This introduces the idea of truncation, meaning that only a finite number of DSE's is considered at a time. It is a general feature, however, that the equation for an n -point function involves a priori unknown higher order correlation functions. Thus assumptions about the latter ones have to be made. The philosophy is to find a truncation that e.g. respects the symmetries of the theory, is consistent with multiplicative renormalisability, incorporates phenomenological implications and reproduces perturbative QCD (pQCD) at high energies. That the knowledge of all Green's function is equivalent to the solution of a given theory can be seen from the expansion of the effective action in terms of vertex functions

$$\Gamma[\Phi] = \sum_n \int_{x_1 \dots x_n} \frac{1}{n!} \Gamma^{(n)}(x_1, \dots, x_n) \Phi(x_1) \dots \Phi(x_n), \quad (3.16)$$

where each coefficient function $\Gamma^{(n)}$ is determined by its DSE.

The quark DSE. The quark propagator is defined as

$$S(x-y) := \left(\frac{\delta^2 \Gamma_{\text{QCD}}}{\delta\Psi_x \delta\bar\Psi_y} \right)^{-1}. \quad (3.17)$$

The Fourier transform of the propagator $S(p)$ is taken to be

$$S(x) = \int_p S(p) e^{-ip \cdot x}, \quad (3.18)$$

where the momentum-space propagator can be parametrized via two dressing functions A and B as

$$S(p) = \frac{i\not{p}A(p^2) + B(p^2)}{p^2 A^2(p^2) + B^2(p^2)}. \quad (3.19)$$

In order to obtain the DSE for the quark propagator, the generating functional of DSE's (3.15) has to be evaluated for the QCD action (3.6) and the field variable Φ has to be replaced by the quark field $\bar{\Psi} = \langle \bar{\psi} \rangle$. One further derivative of this expression with respect to Ψ yields the quark DSE given in momentum space representation

$$S^{-1}(p, \mu) = Z_\psi(\Lambda, \mu) S_0^{-1}(p, \Lambda) + \Sigma(p, \mu), \quad (3.20)$$

where the dependences on the UV-cutoff Λ and the renormalization scale μ are shown explicitly. Here S^{-1} is the full inverse quark propagator, $S_0^{-1}(p, \Lambda) = -i\not{p} + Z_m(\Lambda, \mu)m(\mu)$ is the inverse bare propagator and the self energy Σ is given as the integral expression

$$\Sigma(p, \mu) = g^2(\mu) Z_{\psi A}(\Lambda, \mu) C_f \int_q^\Lambda D_{\mu\nu}(p - q, \mu) \Gamma_\mu(q, p\mu) S(q, \mu) \gamma_\nu. \quad (3.21)$$

The (colorless part of the) full quark gluon vertex Γ_μ is herein defined as

$$-ig\Gamma_\mu t^a = \frac{\delta^3 \Gamma_{\text{QCD}}}{\delta \Psi \delta A_\mu^a \delta \bar{\Psi}}, \quad (3.22)$$

and the color algebra is already gathered in the Casimir $C_f = t^a t^a$ that in the fundamental representation evaluates to $(N_c - 1/N_c)/2 = 4/3$. Furthermore the fully dressed gluon propagator is denoted as $D_{\mu\nu}(k)$. The colorless part of the gluon looks formally like the photon propagator introduced in the next paragraph in Eq. (3.27). The quark DSE is represented graphically in fig. 3.1.

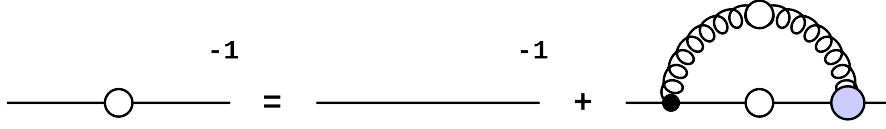


Figure 3.1: The quark DSE from Eq. (3.20). White circles denote fully dressed propagators and the blue blob represents the dressed 1PI quark gluon vertex.

The photon Dyson-Schwinger equation. Another equation that is important in the course of this thesis is the photon DSE. This will be needed to define the hadronic photon self energy which is a vital ingredient for the leading order hadronic contribution to the anomalous magnetic moment of the muon. Therefore we introduce the Lagrangian of QED

$$\mathcal{L}_{\text{QED}} = Z_{\psi}^{\text{QED}} \bar{\psi}(\not{\partial} + m)\psi + ieZ_{\psi A}^{\text{QED}} \bar{\psi} \not{A} \psi + \frac{Z_A^{\text{QED}}}{4} F_{\mu\nu} F_{\mu\nu}. \quad (3.23)$$

Here A_{μ} is a $U(1)$ gauge field and $e = e(\mu)$ is the electric charge renormalized at a certain scale. This scale μ is usually taken to be on-shell. The electron and photon propagators are chosen to be bare at the physical pole masses

$$S^{\text{QED}}(p^2 \rightarrow m_{\text{phys}}^2) = \frac{i\not{p} + m_{\text{phys}}}{p^2 + m_{\text{phys}}^2} \quad m(\mu^2 = m^2) = m_{\text{phys}} \quad (3.24)$$

$$D_{\mu\nu}^{\text{QED}}(p^2 \rightarrow 0) = \left(\delta_{\mu\nu} - \frac{p_{\mu} p_{\nu}}{p^2} \right) \frac{1}{p^2} + \xi \frac{p_{\mu} p_{\nu}}{p^4} \quad e(\mu^2 = 0) = e_{\text{phys}}. \quad (3.25)$$

In order to obtain the photon DSE the QED action corresponding to (3.23) has to be used to construct the generating functional of DSE's (3.15). Here the first and the second variations have to be with respect to the field A_{μ} owing to the definition of the full photon propagator $D_{\mu\nu}$

$$D_{\mu\nu} := \left(\frac{\delta^2 \Gamma_{\text{QED}}}{\delta A_{\mu} \delta A_{\nu}} \right)^{-1}, \quad (3.26)$$

where the Fourier transform of this two-point function can be parametrized as

$$D_{\mu\nu}(p) = \left(\delta_{\mu\nu} - \frac{p_{\mu} p_{\nu}}{p^2} \right) \frac{1}{p^2} \frac{1}{1 + \Pi(p^2)} + \xi \frac{p_{\mu} p_{\nu}}{p^4}, \quad (3.27)$$

where the quantum corrections are described by the dressing function Π and ξ is the covariant gauge fixing parameter for the $U(1)$ symmetry of QED. The DSE for the photon is derived in appendix B and reads in momentum space representation

Figure 3.2: The photon DSE defined in Eq. (3.30). Full Propagators are denoted by white blobs and the red blob marks the full 1PI fermion-photon vertex.

$$D_{\mu\nu}^{-1}(p, \mu) = Z_A^{\text{QED}}(\Lambda, \mu)(D_{\mu\nu}^0(p, \Lambda))^{-1} + \Pi_{\mu\nu}(p, \mu), \quad (3.28)$$

where

$$D_{\mu\nu}^{-1}(p, \Lambda) = \left(\delta_{\mu\nu} - \frac{p_\mu p_\nu}{p^2} \right) p^2 + \frac{p_\mu p_\nu}{\xi}, \quad (3.29)$$

is the bare inverse photon propagator and the self energy given in terms of the vacuum polarization tensor $\Pi_{\mu\nu}$

$$\Pi_{\mu\nu}(p, \mu) = -e^2(\mu) Z_{\psi A}^{\text{QED}}(\Lambda, \mu) \int_q^\Lambda \text{Tr}[S(q_+, \mu) \gamma_\mu S(q_-, \mu) \Gamma_\mu(q_-, q_+, \mu)], \quad (3.30)$$

where the momentum routing is chosen such that $q_\pm = q \pm p/2$. Γ_μ is the full fermion-photon vertex defined analogous to (3.22), with A_μ being the Abelian gauge field and the coupling $-e$ instead of the strong coupling g . See also appendix E and Eq. (B-6). The photon DSE is graphically represented in fig. 3.2.

Bethe-Salpeter equations. The starting point for a consideration of quark anti-quark bound states is the so called T-matrix. In order to define it we start with the following Green's function

$$G(x_1, x_2, y_1, y_2) = \langle 0 | T \psi(x_1) \bar{\psi}(x_2) \psi(y_1) \bar{\psi}(y_2) | 0 \rangle, \quad (3.31)$$

where we use the canonical formulation in Minkowski space for this particular purpose (contrary to the Euclidean functional formalism used in most parts of the thesis). In addition we define the total and relative coordinates

$$X = \frac{x_1 + x_2}{2} \quad Y = \frac{y_1 + y_2}{2} \quad x = x_1 - x_2 \quad y = y_1 - y_2, \quad (3.32)$$

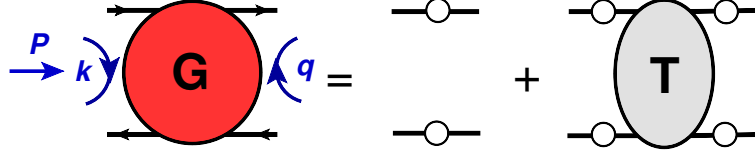


Figure 3.3: The G-Matrix (shown in red) can be decomposed into a disconnected piece given by two propagators and a connected one. The amputated connected part defines the T-Matrix shown in grey. White blobs denote fully dressed propagators. The arrows on the external legs of the G-matrix show the particle/anti-particle content that is omitted in the remaining amplitudes. In addition the momentum routing is indicated in blue.

with their total and relative conjugate momenta $(X, Y) \leftrightarrow P$, $x \leftrightarrow k$ and $y \leftrightarrow q$ where X and Y have the same conjugate momentum P due to momentum conservation. The conjugate momenta of $x_{1/2}$ are k_{\pm} and those of $y_{1/2}$ are q_{\pm} which are defined to be parallel to the spin direction of the fermion lines (see fig. 3.3)

$$P = k_+ - k_- = q_+ - q_- \quad k = \frac{k_+ + k_-}{2} \quad q = \frac{q_+ + q_-}{2} \quad (3.33)$$

This enables us to define the momentum space version of a general four-point function Γ via

$$\Gamma(x_1, x_2, y_1, y_2) = \int_{P, k, q} e^{-iP \cdot (X-Y)} e^{-ik \cdot x} e^{iq \cdot y} \Gamma(P, k, q). \quad (3.34)$$

The T-matrix is the amputated, connected piece of (3.31). Written in a condensed notation where matrix multiplication includes contraction of two-particle legs in all indices the relation reads

$$G_{ij,kl} = S_{ij}S_{kl} + S_{iu}S_{jv}T_{uv,rs}S_{rk}S_{sl}, \quad (3.35)$$

where S represents the full quark propagator. This relation is diagrammatically shown in fig. 3.3. Both four-point functions (G and T) contain quark anti-quark bound states as is detailed in Ref. [63]. This can be seen by inserting a full set of physical states into the matrix element (3.31) under the assumption $x_1^0, x_2^0 > y_1^0, y_2^0$

$$G(x_1, x_2, y_1, y_2) \approx \int dP \theta(P^0) \delta(P^2 - M^2) \langle 0 | T \psi(x_1) \bar{\psi}(x_2) | P \rangle \langle P | T \psi(y_1) \bar{\psi}(y_2) | 0 \rangle, \quad (3.36)$$

where only the lowest lying state $|P\rangle$ has been retained. This defines the Bethe-Salpeter wave function

$$\chi_P(x_1, x_2) = \langle 0 | T \psi(x_1) \bar{\psi}(x_2) | P \rangle, \quad (3.37)$$

which is a strict on-shell quantity $P^2 = M^2$. The behaviour of the Heisenberg-fields under space-time translations together with the invariance of the vacuum yields

$$\chi_P(x_1, x_2) = \chi_P(x/2, -x/2) e^{-iP \cdot X} \Big|_{P^2=M^2},$$

where $P^2 = M^2$ is the dispersion relation of the massive one particle state $|P\rangle$. Defining the momentum space version of the wave function

$$\chi_P(x/2, -x/2) = \int_k e^{-ik \cdot x} \chi(P, k), \quad (3.38)$$

one obtains

$$G(P, k, q) \approx -i \frac{\chi(P, k) \bar{\chi}(P, q)}{P^2 - M^2} + \text{terms regular at } P^2 = M^2. \quad (3.39)$$

In this equation $\bar{\chi}$ is the conjugate of (3.37). Furthermore the identity

$$\int \frac{d^4 p}{(2\pi)^4} \frac{1}{p^2 - m^2} \theta(p^0) e^{-ip \cdot x} f(p) = -i \int \frac{d^3 p}{(2\pi)^3} \frac{1}{2p^0} e^{-ip \cdot x} f(p) \Big|_{p^2=m^2}, \quad (3.40)$$

was used which holds for $x^0 > 0$. The steps starting from (3.36) show that under the assumption that the momentum operator has an eigenstate with mass M and that the total momentum is not far off-shell $P^2 \approx M^2$ (3.39) gives rise to a bound state pole in the matrix element. Turning this argument around, a pole in the four-point function (3.31) signals the existence of the physical state with mass M .

The G-matrix can be shown to obey the following Bethe-Salpeter equation [64]. A derivation from the two-particle irreducible (2PI) effective action (see [65, 66]) perspective using functional techniques can be found in [67].

$$G = SS + GKSS, \quad (3.41)$$

which is graphically represented in fig 3.4. The matrix multiplication in (3.41) is a condensed form of the contractions in (3.35). The interaction kernel K contains only interactions that are 2PI with respect to the quark lines. In the 2PI formalism this corresponds to the second variation of the 2PI part of the effective action with respect to the quark two-point function $\delta^2 \Gamma_2 / \delta S^2$. In order to find the equation for the BSE for the T-matrix we just have to insert (3.35) in (3.41) to obtain

$$T = K + TSSK \quad (3.42)$$

and the corresponding diagram in fig. 3.5. Regarding the definition of the T-matrix (3.35) shown in fig. 3.3 it is obvious that the bound state pole cannot arise from the disconnected part which can at most contain quark-states. Due to confinement even that possibility is

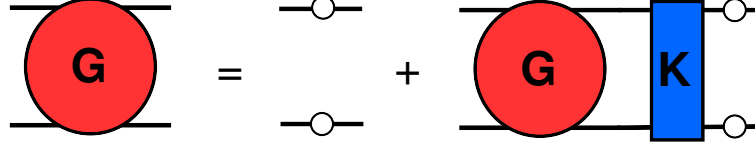


Figure 3.4: The inhomogeneous BSE for the G-matrix. White blobs represent full propagators while the interaction Kernel K is shown in blue.

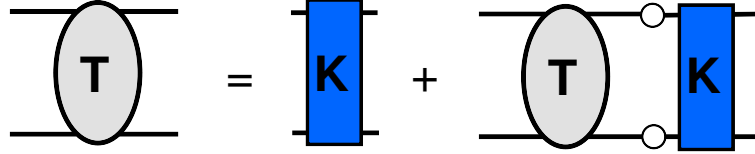


Figure 3.5: The inhomogeneous BSE for the T-matrix. White blobs represent full propagators while the interaction Kernel K is shown in blue.

excluded. Thus the bound-state pole structure must be entirely contained in the T-matrix. In order to obtain a resonance expression for the T-matrix similar to Eq. (3.39) we start with the Bethe-Salpeter amplitude (BSA) that is defined as the amputated version of the wave function

$$\Gamma(P, k) = S^{-1}(k_+) \chi(P, k) S^{-1}(k_-). \quad (3.43)$$

With this definition we can write down the following expansion

$$T(P, k, q) \approx -i \frac{\Gamma(P, k) \bar{\Gamma}(P, q)}{P^2 - M^2} + \text{regular terms}. \quad (3.44)$$

Finally inserting (3.44) into the BSE for the T-matrix (3.42) and equating residues at $P^2 = M^2$ we arrive at an equation for the Bethe-Salpeter amplitude Γ

$$\Gamma = \Gamma S S K, \quad (3.45)$$

which shows that the amplitude Γ is basically an eigenvector of the interaction kernel K with eigenvalue one. Since Eq. (3.45) is a homogeneous equation, the solution Γ needs

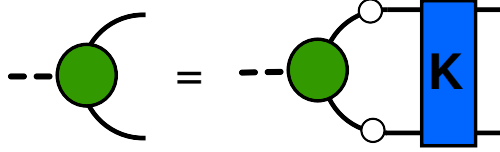


Figure 3.6: The homogeneous BSE for the bound state amplitude (green blob) defined in (3.45). White blobs represent full propagators while the interaction Kernel K is shown in blue.

an additional normalization condition. The normalization which is originally present in the inhomogeneous equation for the G -matrix (3.41) is lost in the process of deriving (3.45). By writing $G = SS + \lambda GKSS$ and $\Gamma = \lambda \Gamma SSK$ a normalization condition can be derived for (3.45) that ensures the consistency for the residue implied by the pole decomposition of G in (3.36)

$$\frac{dM^2(\lambda)}{d \ln \lambda} = i\bar{\Gamma}SS\Gamma, \quad (3.46)$$

where $M_{\text{physical}}^2 = M^2(\lambda = 1)$ is the bound state mass for which the BSE (3.45) has a solution. This is detailed in [68]. Equation (3.45) which is a homogeneous BSE allows for a calculation of mesonic quark anti-quark bound states of QCD for different flavour quantum numbers, spins and discrete symmetries. These quantum numbers are selected by an explicit choice for the representation of the amplitude Γ . In addition higher radial excitations can be considered [69].

The quark-photon vertex BSE. Another equation that is of high relevance for the present thesis is the inhomogeneous BSE for the quark-photon vertex. This vertex is defined as a variation of the effective action of the electro magnetic theory combined with QCD

$$-ie\Gamma_\mu = \frac{\delta^3 \Gamma_{\text{QCD+QED}}}{\delta \Psi \delta A \delta \bar{\Psi}}, \quad (3.47)$$

where the fermions Ψ represent quark degrees of freedom. These represent the spinor degrees of freedom in the QCD action (3.6) as well as in the QED action (3.23) and the gauge field A is the $U(1)$ gauge field (the photon) of QED. The bare Lagrangian is the sum of the bare Lagrangians of both theories. Later on we will work partially in the approximation that the photon field is just an external background field that does not propagate as a virtual degree of freedom inside any loop diagram, but for the moment our statements are completely general. The quark-photon vertex is the key object for investigations of electro-magnetic properties of hadrons like form factors and charge radii [70]. It is the essential link between QCD and QED. The corresponding vertex equation can be obtained from the BSE obeyed by the G -matrix (3.41) by coupling the left two fermion lines to an electromagnetic current $j_\mu = \bar{\psi}\gamma_\mu\psi$ and

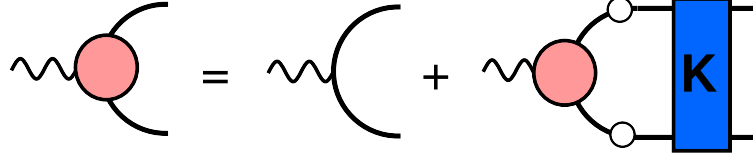


Figure 3.7: The inhomogeneous BSE for the quark-photon vertex (red blob). White blobs represent full propagators while the interaction Kernel K is shown in blue.

removing the external quark leg dressings on the right. This results in the following form of the equation

$$\Gamma_\mu = \gamma_\mu + \Gamma_\mu S S K, \quad (3.48)$$

while the corresponding diagrammatic representation can be found in figure 3.7. A very important property of the vertex amplitude defined via Eq. (3.48) is that it contains dynamically generated quark anti-quark bound states for time-like photon momenta which effectively resembles the phenomenologically very successful idea of vector meson dominance (VMD) [71]. This model assumes that the electromagnetic coupling of quarks to photons is achieved via a mixing of the photon with the vector meson which is the ρ particle. This is quantum mechanically allowed since both have the same quantum numbers $J^{PC} = 1^{--}$. The fact that the vector meson pole is present can be seen by considering the amplitude

$$\langle (\bar{\psi} \gamma_\mu \psi) \psi \bar{\psi} \rangle = \Gamma_\mu S S, \quad (3.49)$$

which equals the quark-photon vertex with to fully dressed quark propagators attached. Now a full set of Hilbert space states can be inserted and a bound state pole can be identified following the procedure of Eqs. (3.36) to (3.39). In this way one arrives at a homogeneous bound state equation (3.45) with a Bethe-Salpeter amplitude carrying vector meson quantum numbers.

It has to be emphasized that the interaction kernel K shown in fig. 3.7 in principle contains QCD as well as QED processes. We will however neglect QED effects inside any self-consistent equation. This is because these are suppressed by an additional factor of $\alpha \approx 1/137$, the fine-structure constant, which defines the electro magnetic interaction strength. We thus rely on the leading perturbative order as far as QED is concerned. QCD contributions, on the other hand, are not suppressed due to the fact that the strong coupling constant g or correspondingly $\alpha_s = g^2/4\pi$ is of the order one at the scale of interest (around and below 1GeV) and perturbation theory is thus not applicable. The result is that the low-energy electro magnetic interaction of quarks is dominated by QCD effects to more than 99%.

3.3 Symmetries and Ward-Takahashi identities

In the present section we will discuss implications from symmetries that have been taken into account to construct the interaction kernel used in this work. Two symmetries are of immediate importance. On the one hand this is the chiral symmetry of QCD which is highly relevant for dynamical mass generation and meson phenomenology. The second is the $U(1)$ gauge symmetry of QED which ensures the conservation of charge. Both symmetries manifest themselves in the form of Ward-Takahashi identities (WTI's) on the level of Green's function and thus can be used to constrain the latter ones. In addition we will discuss the role of anomalous symmetries. The most important phenomenological consequences of anomalies are the rather large η' mass and the $\pi^0 \rightarrow \gamma\gamma$ decay.

Chiral symmetries of QCD In the chiral limit, that is if the bare quark masses in the action of QCD (3.6) are zero, QCD exhibits a special symmetry

$$\psi \rightarrow e^{iT^a \theta^a \gamma_5} \psi \quad \bar{\psi} \rightarrow \bar{\psi} e^{iT^a \theta^a \gamma_5}, \quad (3.50)$$

which is a global $U(N_f)$ rotation in the fundamental representation acting on quark-spinors which are N_f -multiplets. The T^a are the N_f^2 generators of the $U(N_f)$ Lie-group and the θ^a are the parameters of the transformation and coordinates on the group manifold. The Euclidean Dirac matrix is defined as

$$\gamma_5 = \gamma_0 \gamma_1 \gamma_2 \gamma_3. \quad (3.51)$$

Its presence signals the rotation of left-handed and right-handed spinors with opposite phases. In the absence of quark masses the QCD Lagrangian ((3.3) or (3.6)) is invariant under the independent chiral rotation of left-handed and right-handed fields and thus has the symmetry $U_L(N_f) \times U_R(N_f)$. This symmetry can be equally written as $U_V(N_f) \times U_A(N_f)$ where the transformations have been split into vector symmetry (left and right spinors transform alike $\theta_L = \theta_R$) and axial symmetry (left and right spinors transform with $\theta_L = -\theta_R$). The symmetry (3.50) is dynamically broken in QCD which most prominently results in dynamical generation of meson and nucleon masses. Via the Goldstone theorem this leads to the occurrence of (pseudo-) Nambu-Goldstone bosons, which are the most important physical degrees of freedom at low energies [72, 73]. Since each Goldstone boson corresponds exactly to one broken symmetry, an effective low energy theory can be derived on the grounds of symmetry considerations alone, that is independent of the details of QCD [74, 75]. Since the masses of the up and down quarks, while not exactly zero, are small compared to the effect of dynamical chiral symmetry breaking (D χ SB) these can be treated as perturbations in the framework of chiral perturbation theory (χ PT). At very low energies one thus has a firm ground where considerations can rest on. It is imperative to incorporate the consequences of these insights into any truncation of the Dyson- Schwinger equations of QCD if they are supposed to yield a

good description of low-energy QCD and the phenomenology of bound states of light quarks [76, 77].

This means that any model of QCD that has the correct symmetries and symmetry breaking patterns can reproduce many important low energy constraints such as the Gell-Mann–Oakes–Renner relation (GMOR) as for example the Nambu–Jona-Lasinio model [78, 79]. An important consequence of the chiral symmetry is the axial-vector-WTI [80, 77]

$$\begin{aligned} iP_\mu \Gamma_\mu^{5,a}(P, k) &= S^{-1}(k_-) \gamma_5 T^a + \gamma_5 T^a S^{-1}(k_+) \\ &\quad - \Gamma_\mu^{5,a}(P, k) \\ &\quad + C_e \mathcal{F}_{\text{QED}}(P, k) \text{Tr}[T^a Q^2] \\ &\quad + C_g \mathcal{F}_{\text{QCD}}^{ij}(P, k) \text{Tr}[T^a t^i t^j]. \end{aligned} \quad (3.52)$$

Here $k_\pm = k \pm P/2$, T^a are the generators of the axial $U_A(N_f)$ flavour symmetry and the t^i the ones of the $SU(3)$ gauge symmetry of QCD. The following vertices are defined: the axial-vector vertex

$$\Gamma_\mu^{5,a}(x, y, z) = \int_{u,w} S^{-1}(x-u) \langle (\bar{\psi}(z) \gamma_\mu \gamma_5 T^a \psi(z)) \psi(u) \bar{\psi}(w) \rangle S^{-1}(w-y), \quad (3.53)$$

the pseudo-scalar vertex

$$\Gamma_\mu^{5,a}(x, y, z) = \int_{u,w} S^{-1}(x-u) \langle (\bar{\psi}(z) \gamma_5 \{M, T^a\} \psi(z)) \psi(u) \bar{\psi}(w) \rangle S^{-1}(w-y), \quad (3.54)$$

where M is the quark-mass matrix and the quantities $\mathcal{F}(P, k)$ which are terms that are present in (3.52) due to anomalous symmetries

$$\mathcal{F}_{\text{QCD}}^{ij}(z, x, y) = \int_{u,w} S^{-1}(x-u) \langle \mathcal{O}^{ij}(z) \psi(u) \bar{\psi}(w) \rangle S^{-1}(w-y). \quad (3.55)$$

The involved operator is $\mathcal{O}^{ij}(z) = \epsilon_{\mu\nu\alpha\beta} F_{\mu\nu}^i F_{\alpha\beta}^j$ (the Abelian case for QED is similar) and might be identified with the topological charge density [81]. These appear with pre-factors $C_q = \frac{q^2}{16\pi^2}$. The traces of these anomalous terms in (3.52) reduce them to certain flavour channels a . The anomaly involving the non-Abelian fields $F_{\mu\nu}^i$, which is called the Abelian anomaly since it involves the Abelian chiral subgroup $U_A(1)$ i.e. the singlet part, is only present for $a = 0$. This is because $\text{Tr}[T^a] = 0$ for $a \neq 0$. The non-Abelian anomaly owes its name to the fact that it is related to the non-Abelian $U_A(N_f)$ chiral transformation. It

contains the Abelian fields $F_{\mu\nu}$ from QED. The flavour trace reduces its effects to the flavour diagonal channels $a = 0, 3, 8$. For all other channels the trace evaluates to zero with the charge matrix being defined as $Q = \text{diag}(2/3, -1/3, -1, 3)$ for $N_f = 3$. The derivation of (3.52) is detailed in App. C.

The implications of (3.52) that are relevant here are threefold. First of all considering the chiral limit $M(\Lambda^2) = 0$ and neglecting anomalous terms only the first line remains. This version yields an important constraint for phenomenological models since it guarantees consistency with Goldstone's theorem [77] i.e. that the pion becomes massless in the chiral limit. This can be used to formulate a relation between the quark self-energy in (3.20) and the Bethe-Salpeter interaction kernel defined via (3.41) [76] such that the AXWTI is fulfilled. This will be elaborated further in chapter 4.

The last term in (3.52) has the important consequence that the η^0 meson which is the singlet pseudo-scalar particle is not a Goldstone boson, since $U_A(1)$ is not a symmetry of the quantum theory and thus no symmetry breaking can occur. This explains the rather large mass of the η^0 compared to the octet mesons [82, 83]. In the framework of DSEs the topological contribution to the η^0 mass has been considered in Ref. [84] using the Kogut-Susskind mechanism [85]. A phenomenological treatment has been examined in [86].

The anomalous term in the AXWTI involving the photon field gives rise to the $\pi^0 \rightarrow \gamma\gamma$ decay. The predicted decay width agrees quite well with experimental results [87, 80].

The QED Ward-Identity. Another important WTI arises from the $U(1)$ gauge symmetry of QED. It yields a relation between the quark propagator and the quark-photon vertex

$$iP_\mu \Gamma_\mu(P, k) = S^{-1}(k_-) - S^{-1}(k_+). \quad (3.56)$$

Here Γ_μ is the fully dressed quark-photon vertex and S^{-1} is the full inverse quark propagator. The full quark-photon vertex can be decomposed into transverse part Γ_μ^T and a non-transverse part Γ_μ^L

$$\Gamma_\mu = \Gamma_\mu^L + \Gamma_\mu^T, \quad (3.57)$$

where the transverse piece obeys $P_\mu \Gamma_\mu^T = 0$. The vector-WTI constrains the strictly longitudinal part of the vertex (the projection onto P_μ). Using this constraint and imposing regularity for $P^2 \rightarrow 0$ the non-transverse part is uniquely determined in terms of the quark propagator as was shown in [88]. The resulting vertex construction is referred to as the

Ball-Chiu construction

$$\Gamma_\mu^{\text{BC}}(P, k) = \gamma_\mu \Sigma_A + 2\not{k} k_\mu \Delta_A + i k_\mu \Delta_B, \quad (3.58)$$

where the symbols

$$\Sigma_F = \frac{F(k_+^2) + F(k_-^2)}{2} \quad \Delta_F = \frac{F(k_+^2) - F(k_-^2)}{k_+^2 - k_-^2}, \quad (3.59)$$

have been used and A and B are the quark dressings.

4 Working with a truncation of the DSE's of QCD

In the present chapter we explain the truncated versions of Dyson-Schwinger Equations and Bethe-Salpeter Equations introduced in chapter 3 we use in order to obtain results for the hadronic contributions to the muon $g - 2$. In addition we outline the philosophy of the used approach that underlies the definition of certain Green's functions.

As explained in chapter 3 the Dyson-Schwinger equations (DSE's) are an exact representation of a given QFT. In order to provide a tractable framework, however, they have to be truncated. One is then left with a finite number of equations. This requires the introduction of certain assumptions concerning higher order n -point functions.

4.1 Rainbow-ladder truncation

A rather simple yet very successful truncation is the rainbow-ladder truncation (RL). Here the Yang-Mills (YM) sector of QCD is truncated to two-point functions, all high-order functions are ignored which makes the framework essentially Abelian as far as the topology of possible diagrams is concerned. The YM content is combined into an effective, non-local four-fermion interaction that corresponds to a projection of the gluon propagator together with the quark-gluon vertex. In addition the single gauge-boson exchange character is recovered in the high-energy regime ensuring multiplicative renormalisability and the correct limit towards perturbative QCD including $\mathcal{O}(\alpha)$ resummation. In this way certain Green's functions as e.g the quark propagator behave quite similar to their exact, untruncated counterparts, which is actually one condition that constraints this model of the quark-gluon interaction.

The rainbow quark DSE. The starting point is the quark DSE which we show again graphically for the convenience of the reader in fig. 4.1 The RL approximation now takes place on the level of the gluon propagator in Landau gauge ($\xi = 0$ in Eq. (3.6) and (3.27))

$$D_{\mu\nu}(k) = \left(\delta_{\mu\nu} - \frac{k_\mu k_\nu}{k^2} \right) \frac{Z(k^2)}{k^2} \quad (4.1)$$

and the quark-gluon vertex

$$\Gamma_\mu(p, k) = \sum_i^{12} T_\mu^{(i)} \lambda^{(i)}(p, k) \quad (4.2)$$

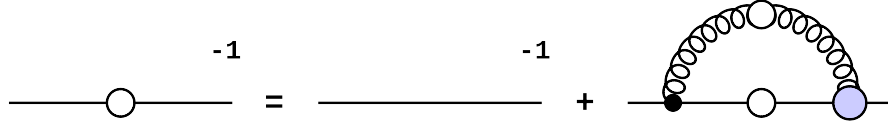


Figure 4.1: The quark DSE from Eq. (3.20). White circles denote fully dressed propagators and the blue blob represents the dressed 1PI quark gluon vertex.

where the gluon dressing function is denoted as $Z(k^2)$, $T_\mu^{(i)}$ are the twelve different possible vertex covariants and $\lambda^{(i)}$ are the corresponding dressing functions. Here p is the momentum of the intermediate quark. A possible basis is given by

$$T_\mu \in \{\gamma_\mu, p_\mu, k_\mu\} \otimes \{\mathbb{1}, \not{p}, \not{k}, [\not{p}, \not{k}]\}. \quad (4.3)$$

Only the perturbative leading structure out of twelve possible ones is retained in the vertex and the dressing function of the vertex is assumed to depend on the gluon momentum k only

$$\Gamma_\mu(p, k) \longrightarrow \Gamma^{\text{RL}}(k^2)\gamma_\mu. \quad (4.4)$$

This enables an ansatz for the combined dressings of gluon and vertex put forward by Maris and Tandy in Ref. [89]

$$\frac{g^2 Z(k^2) \Gamma^{\text{RL}}(k^2)}{Z_c Z_\psi} = 4\pi \left(\frac{\pi}{\omega^6} D k^4 \exp(-k^2/\omega^2) + \frac{2\pi\gamma_m [1 - e^{-k^2/(4m_t^2)}]}{\ln\left(\tau + [1 + k^2/\Lambda_{\text{QCD}}^2]^2\right)} \right), \quad (4.5)$$

where the renormalization constants ensure renormalization group (RG) invariance of the whole expression as is explained below (see [90]). Furthermore we have the parameters $m_t = 0.5 \text{ GeV}$, $\tau = e^2 - 1$, $\gamma_m = 12/(33 - 2N_f)$, $\Lambda_{\text{QCD}} = 0.234 \text{ GeV}$, $\omega = 0.4 \text{ GeV}$ and $D = 0.93 \text{ GeV}^2$. The model interaction features logarithmic running in the perturbative regime $k^2 \gg \Lambda_{\text{QCD}}^2$ where it behaves as

$$g^2 Z(k^2) \Gamma^{\text{RL}}(k^2) \longrightarrow 4\pi \frac{\pi\gamma_m}{\ln(k^2/\Lambda_{\text{QCD}}^2)} = 4\pi\alpha_s(k^2).$$

Here $\gamma_m = 4/b_0$ is the anomalous dimension of the running mass in the perturbative regime

$$m(Q^2) = \left(\frac{\alpha_s(Q^2)}{\alpha_s(\mu^2)} \right)^{\gamma_m} m(\mu^2), \quad (4.6)$$

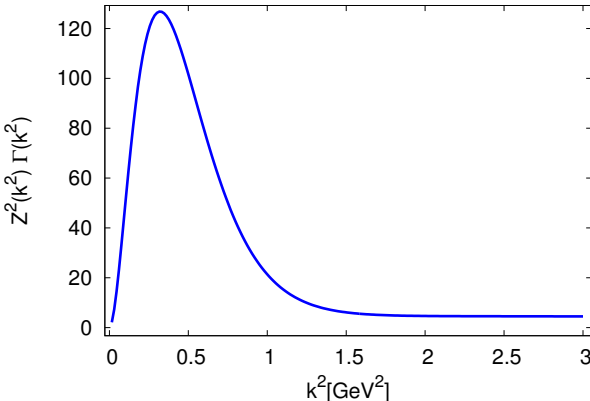


Figure 4.2: A graphical representation of the Maris-Tandy interaction defined in Eq. (4.5). The curve features an enhanced strength in the IR and perturbative running in the UV.

where α_s is the strong running coupling and $b_0 = 11 - 2/3N_f$ is the first coefficient of the beta function [91, 92]. The second term in (4.5) guarantees that this form of the running mass is recovered in the perturbative regime. The exponential term parametrised by ω and D provides enough interaction strength in the infrared for dynamical chiral symmetry breaking to occur. This part triggers the dynamical generation of the quark mass and the formation of a condensate $\langle \bar{\psi}\psi \rangle$ as can be observed in the quark DSE (see below). The interaction is shown graphically in fig. 4.2. The fact that this model interaction vanishes in the IR makes it numerically easier to handle, the deep infra-red is, however, not important for mesonic observables [45]. Using the introduced interaction in the quark DSE ((3.20) and (3.21)) we find

$$S^{-1}(p) = Z_\psi S_0^{-1}(p) + g^2 Z_{\psi A} \frac{4}{3} \int_a \gamma_\mu S(q) \gamma_\nu \Gamma^{\text{RL}}(k^2) D_{\mu\nu}(k^2), \quad (4.7)$$

with $k = q - p$. To make the notation more compact we define the rainbow-ladder interaction kernel as

$$K_{rs,tu}(k) = G(k^2)T_{\mu\nu}(k)[\gamma_\mu]_{rt}[\gamma_\nu]_{us}, \quad (4.8)$$

where $T_{\mu\nu}(k) = \left(\delta_{\mu\nu} - \frac{k_\mu k_\nu}{k^2}\right)$ is the transverse projector and

$$G(k^2) = 1/(Z_c Z_\psi) g^2 Z(k^2) \Gamma^{\text{RL}}(k^2)/k^2 \quad (4.9)$$

Graphically we represent the kernel K as

$$K(k^2) = \text{[diagram: a chain of 10 circles, the first is black, the second is white, and the last is blue, all connected by horizontal lines]}. \quad (4.10)$$

The DSE (4.7) depends on the vertex renormalization constant $Z_{\psi A}$. In a treatment that only models the Yang-Mills sector of QCD the vertex constant $Z_{\psi A}$ is not at our disposal. In order to maintain renormalisability we use the relations

$$Z_{\psi A} = Z_g Z_\psi \sqrt{Z_A} \quad 1 = Z_{cA} = Z_g Z_c \sqrt{Z_A} \quad g \sim 1/Z_g, \quad (4.11)$$

where the choice $1 = Z_{cA}$ is a certain scheme specific to Landau gauge [58, 59]. The first two relations of (4.11) are the definitions of the quark-gluon and ghost-gluon vertex renormalisation constants in terms of field and coupling renormalisation constants, while the third expression just defines the dependence of the renormalized coupling on its renormalisation constant. By definition the gluon transforms as $Z \sim 1/Z_A$ and the vertex as $\Gamma^{\text{RL}} \sim Z_{\psi A}$. A simple manipulation using (4.11) yields

$$Z_{\psi A} = \frac{Z_\psi}{Z_c} = Z_\psi^2 \frac{1}{Z_\psi Z_c}. \quad (4.12)$$

which allows a replacement of the vertex renormalisation constant in the quark self-energy in (4.7). That is why the factor including the renormalization constants for the quark and the ghost has been included in (4.5) and (4.9). Using (4.12) and (4.11) the RG dependence of (4.5) vanishes

$$\frac{g^2 Z(k^2) \Gamma^{\text{RL}}(k^2)}{Z_c Z_\psi} \sim \frac{1/Z_g^2 1/Z_A Z_{\psi A}}{Z_c Z_\psi} = \frac{Z_c^2 Z_A 1/Z_A Z_\psi / Z_c}{Z_c Z_\psi} = 1 \quad (4.13)$$

We thus know that the quark self-energy behaves as $\sim Z_\psi^2$ which is the left-over factor from the replacement we have done in (4.12). We are now in the position to formulate the quark DSE (4.7) in the form

$$S^{-1}(p) = Z_\psi (-i\not{p} + Z_m m) + Z_\psi^2 \frac{4}{3} \int_q \gamma_\mu S(p) \gamma_\nu T_{\mu\nu}(k) G(k^2). \quad (4.14)$$

This equation has the correct behaviour under RG transformations. The fully dressed quark behaves as $S \sim 1/Z_\psi$. Thus the left hand side is proportional to Z_ψ as is the first term on the right hand side. The full quark in the self-energy cancels one factor Z_ψ and the function G is RG invariant such that also the second term goes as Z_ψ . The quark DSE in this truncation exhibits multiplicative renormalisability. It can now be solved since the interaction $G(k^2)$ is known. All that is needed is the parametrization

$$S(p) = \frac{i\not{p} A(p^2) + B(p^2)}{p^2 A^2(p^2) + B^2(p^2)}. \quad (4.15)$$

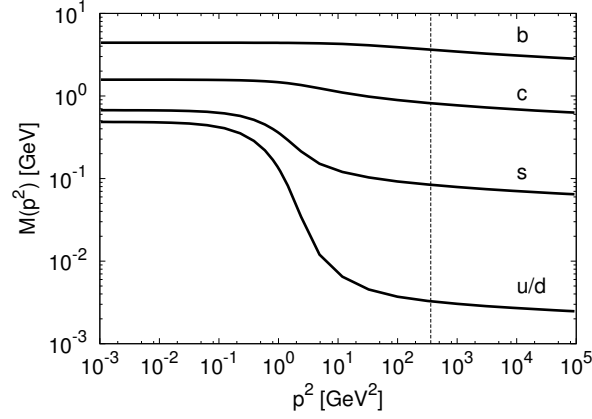


Figure 4.3: The quark mass functions $M(p^2)$ in the Maris-Tandy model as obtained from the quark DSE (4.14). Shown are the functions for the flavours u/d , s , c and b . The vertical line represents the renormalization scale $\mu^2 = (19 \text{ GeV})^2$.

The integral equations for A and B can be obtained by the application of the projections $\text{Tr}[\cdot]$ and $\text{Tr}[\not{p}\cdot]$ on both sides of (4.14). The numerical solution can be obtained by straightforward fixed-point iteration. We choose an initial guess for the functions A and B and then perform the numerical integration until convergence is reached. The criterion is

$$\sup_{p^2} \left| \frac{A^{(n+1)}(p^2) - A^{(n)}(p^2)}{A^{(n)}(p^2)} \right| < \epsilon,$$

where n denotes the iteration step and ϵ is typically of order 10^{-12} . The renormalization conditions are

$$A(\mu^2) = 1 \qquad M(\mu^2) = m_q, \qquad (4.16)$$

where the scale is $\mu^2 = (19 \text{ GeV})^2$ and the quark mass function is just $M = B/A$. The parameter m_q depends on the quark flavour e.g. m_u or m_s . The mass function that is obtained from the DSE (4.14) obeys the relation (4.6) for $p^2 \gg \Lambda_{\text{QCD}}^2$ thus mimicking $\overline{\text{MS}}$ behaviour. The solutions for the quark mass functions for different conditions $M((19 \text{ GeV})^2)$ are shown in figure 4.3. In table 4.1 we show the quark mass at vanishing Euclidean momentum $M(0)$, at the renormalization scale $\mu = 19 \text{ GeV}$ and we compare the mass function at $\mu = 2 \text{ GeV}$ to a mass that is scaled up to 2 GeV from 19 GeV via the perturbative relation (4.6). The mass function behaves logarithmically in the UV according to (4.6). In the IR, however, the dynamical mass generation is clearly visible. Chiral symmetry is dynamically broken. The up and down quarks, for example, acquire dynamical masses of a few hundred MeV consistent

Table 4.1: From left to right we show the quark mass function at the Euclidean origin $M(0)$, the $\overline{\text{MS}}$ masses at 2 GeV $m^{\overline{\text{MS}}}((2 \text{ GeV})^2)$ as well as the mass function at 2 GeV and at 19 GeV. The mass functions are solutions of the DSE (4.14). The $\overline{\text{MS}}$ masses are obtained from $M((19 \text{ GeV})^2)$ via relation (4.6).

[GeV]	$M(0)$	$m^{\overline{\text{MS}}}((2 \text{ GeV})^2)$	$M((2 \text{ GeV})^2)$	$M((19 \text{ GeV})^2)$
u/d	0.477	0.005	0.015	0.0037
s	0.663	0.119	0.16	0.085
c	1.56	1.16	1.25	0.827
b	4.38	5.19	4.32	3.68

with the constituent quark picture. The quark propagator is nevertheless defined on all scales.

Ladder BSE. Using the kernel (4.8) the BSE's for the quark-photon vertex (3.48) and the meson BSE (3.45) can be constructed in ladder truncation. The main constraint is to respect the important symmetries. As already explained in chapter 3 these are the chiral symmetry of QCD and the $U(1)$ gauge symmetry of QED. The former one is closely related to the strong dynamics of QCD and meson observables while the latter one is mandatory for a good description of electro-magnetic form factors of hadrons. The $SU(3)$ gauge symmetry of QCD is not explicitly present in RL truncation, rather it is a global symmetry here. On top of that constructing a quark-gluon vertex that obeys its local STI is a difficult task due to the non-Abelian nature of the relations [44, 93].

Chiral symmetry and $U(1)$ gauge symmetry leave their imprint on the Green's functions in the form of Ward-Takahashi identities (WTIs) as already mentioned. These are the non-anomalous axial-vector Ward-Takahashi-identity (AXWTI) in the chiral limit

$$iP_\mu \Gamma_\mu^{5,a}(P, k) = S^{-1}(k_-) \gamma_5 T^a + \gamma_5 T^a S^{-1}(k_+) \quad (4.17)$$

and the vector WTI (3.56). These symmetries can be guaranteed by using the 2PI formulation of the effective action [65]. In this formulation the Bethe-Salpeter kernel K can be obtained by taking the functional derivative of the quark self-energy Σ with respect to the quark propagator S , schematically

$$K = \frac{\delta \Sigma}{\delta S}. \quad (4.18)$$

It has been shown that this construction principle respects the above mentioned symmetries [76]. Through the AXWTI Goldstones theorem is established such that the pseudo-scalar mesons are the true Goldstone bosons of chiral symmetry breaking (χ SB) while being $q\bar{q}$

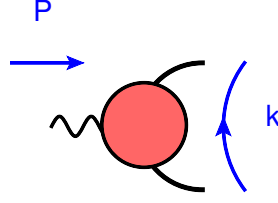


Figure 4.4: The momentum routing for the QED vertex $\Gamma_\mu(P, k)$ from Eq. (4.19). The same routing is used for the meson BSE (4.20).

bound states at the same time. This is further elaborated in [77].

For completeness we give the ladder BSE's for the QED-vertex

$$[\Gamma_\mu]_{rs}(P, k) = Z_{\psi A}^{\text{QED}} \gamma_\mu - Z_\psi^2 \frac{4}{3} \int_q [S(k_+) \Gamma_\mu(P, q) S(k_-)]_{ut} K_{tu,rs}(k - q), \quad (4.19)$$



and the meson bound-state

$$[\Gamma]_{rs}(P, k) = -Z_\psi^2 \frac{4}{3} \int_q [S(k_+) \Gamma(P, q) S(k_-)]_{ut} K_{tu,rs}(k - q), \quad (4.20)$$

explicitly. The momentum routing of the vertices $\Gamma(P, k)$ (QED vertex or meson BSE) is depicted in fig. 4.4. The incoming total momentum is labeled P the relative momentum k . The momenta of the outgoing and incoming quark legs are $k_\pm = k \pm P/2$. The WTI (3.56) ensures $Z_{\psi A}^{\text{QED}} = Z_\psi$ and Z_ψ is determined by the quark DSE.

Numerical solution methods. Numerical solution techniques for truncated DSEs are well known. For the truncation used here we refer to [92, 89]. In order to solve the Bethe-Salpeter equations for the vertex (4.19) and the meson amplitude (4.20) we have to construct the basis decomposition for both amplitudes. In addition we need the projectors that single out the corresponding dressings given a certain vertex amplitude. Using these techniques we can decompose the vertex BSE into twelve coupled integral equations for the dressing functions while four are needed for e.g. the pseudo-scalar mesons. In order to solve the vertex BSEs we make an initial guess for the amplitudes which is just the bare vertex. After that we

Table 4.2: Feynman rules corresponding to the generating functional (4.21, 4.22).

propagator	
interaction	

perform the integral defined in the equation over and over again using a Gaussian quadrature integration rule. This iteration is performed until convergence is reached. For the QED vertex this procedure is detailed in appendix E. The procedure is related but different for the meson amplitudes. There the BSE is formulated as an eigenvalue equation in which the amplitude is the eigenvector. The interaction kernel is basically the matrix whose eigenvalues are to be found. The definition of that matrix is analogous to Eq. (E-11) where it is the usage of numerical integration techniques that make the integration discrete and offer the interpretation as matrix operation.

Rainbow-ladder diagrams. In chapter 5 and 6 we will present our truncation of the relevant hadronic contributions to the muon $g-2$ from the diagrammatic point of view. Therefore it is helpful to have an efficient way to generate the diagrams of rainbow-ladder QCD. The tool we will use is presented in [94]. If the Yang-Mills sector of QCD is truncated to an effective two-point function and only the quarks are treated as dynamical variables the effective generating functional can be cast into the form

$$Z_{\text{RL}} = \int \mathcal{D}[\bar{\psi}\psi] e^{-S_{\text{RL}}}, \quad (4.21)$$

with the rainbow-ladder action

$$S_{\text{RL}} = \int_x \bar{\psi}(\not{\partial} + m)\psi + \frac{1}{2} \int_{x,y} j_\mu^a(x) \tilde{D}_{\mu\nu}(x,y) j_\nu^a(y). \quad (4.22)$$

Here the quark current is defined as $j_\mu^a = \bar{\psi} t^a \gamma_\mu \psi$ and the effective YM-two-point function $\tilde{D}_{\mu\nu}$ represents the rainbow-ladder interaction $\tilde{D}_{\mu\nu} = T_{\mu\nu} G$ from Eq. (4.8). The Feynman-rules of (4.21) and (4.22) are now easy to obtain. Vertices always come in pairs and are connected by an effective gluon as well as joined by bare quark propagators. These rules are graphically represented in fig. 4.2. Furthermore it can be shown that the rainbow quark DSE (4.14) and the ladder meson BSE can be obtained from (4.21) if only planar effective gluon exchanges are taken into account [94].

The truncation just presented is extremely successful phenomenologically. The long list of observables include meson properties like masses and decay constants of light pseudo-scalar mesons [92], light vector mesons [89]. In addition form factors and transition form factors

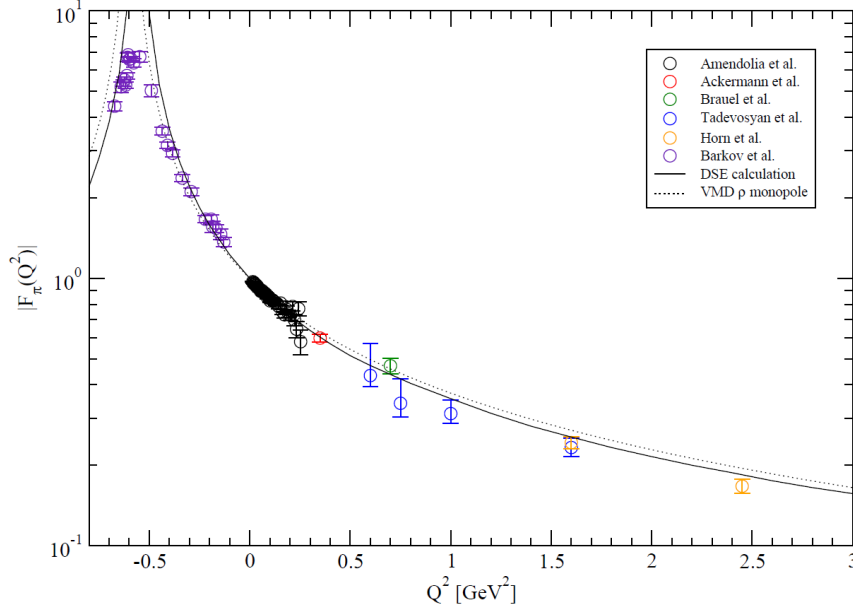


Figure 4.5: The pion form factor $F_\pi(Q^2)$ calculated in the framework used in the present work. It was first calculated in [70]. The version shown here is taken from a talk of A. Krassnigg [109]. It can be seen that the form factor nicely incorporates the ρ -pole. The result is compared to experimental data [110, 111, 112, 113, 114, 115] and to a VMD estimate.

have been calculated [70, 95]. Also heavier mesons have been considered [96]. In addition baryons have also been treated very successfully. Included is the nucleon [97, 98], the Delta and the Omega baryon [99], various baryonic form factors [100] as well as transition form factors [101]. An overview over the approach is given in [102]. A collection of observables calculated withing this framework is presented in table 4.3.

Another example that is highly relevant for the results that will be presented later on is the calculation of the pion form factor $F_\pi(Q^2)$. In the present framework this was first done in [70]. We present an updated version taken from a talk of A. Krassnigg [109] in figure 4.5. The form factor is reproduced at all scales from space-like to time-like. The slope at the Euclidean origin, which determines the pion charge radius, agrees also quite well. Furthermore the ρ -pole in the time-like region is clearly visible. This is a result of the fact that self-consistent quark-photon vertex that is used in this calculation has this bound state dynamically included. Vector meson dominance is thus automatically included, at least for this observable. The ρ pole is at the correct position, since this bound state has vanishing decay width in this truncation, however, the form factor diverges stronger than in reality.

4.2 Beyond rainbow-ladder truncation

Of course it is desirable to establish a truncation that goes beyond the treatment introduced in the last section. Much work has already been devoted to this task. We will give a short account of the main ideas and developments in this direction.

Yang-Mills sector. One of the most desirable features of a beyond the rainbow treatment consists of replacing the completely modelled Yang-Mills sector in (4.5) by a self-consistent dynamical treatment. The two-point functions in that sector, the gluon and ghost propagators, are in fact nicely described by existing Dyson-Schwinger truncations [116, 60, 61]. Taking into account two-loop diagrams [41] or combining the DSE framework with functional renormalisation group techniques [42] the Landau gauge gluon and ghost propagators compare to the lattice propagators on the quantitative level. One ingredient (the $Z(p^2)$ dressing) needed for the interaction kernel (4.9) is thus precisely known.

Matter sector and quark-gluon vertex. Also the coupled equations of the YM sector and the quark sector have been solved self-consistently on the level of propagators [44]. One needs however in addition the quark gluon vertex. The back coupling of matter into that object has been investigated for example in Refs. [45, 117] where the effect of unquenching onto the quark propagator and on pion observables has been studied. The quark gluon vertex has also been investigated from the view-point of its DSE in [93] yielding improved truncation that includes non-Abelian gluon interactions explicitly [118] and furnishes a solution of the $U_A(1)$ problem and the η' mass [84]. Another line of thought makes intensified use of WTIs in order to obtain meson observables in channels that are beyond the scope of the RL truncation [119].

In the present work we stick, however, to the simple but phenomenologically well established model of the quark gluon interaction given through (4.5). One reason is of course its simplicity which facilitates the rather complex calculations. In addition, as will be explained in chapter 6 and appendix F, it allows for an unambiguous definition of the light-by-light scattering contribution that is much more complicated in more advanced truncations. Another reason is the long list of observables that have been calculated in rainbow ladder truncation using the model (4.5) which includes the degrees of freedom and properties we gauge as most important in the present work. These are the mesons in the pseudo scalar and vector channels. In fact it has been shown that beyond rainbow-ladder effects are small in these channels [120]. It is fair to say that no beyond rainbow-ladder truncation has yet superseded the RL treatment in this phenomenological respect.

Pseudoscalar Mesons [92]			Vector Mesons [89]		
	exp.	calc.		exp.	calc.
$-\langle\bar{\psi}\psi\rangle_\mu^0$	$(0.236 \text{ GeV})^3$	$(0.241 \text{ GeV})^3$	$m_{\rho/\omega}$	0.770 GeV	0.742 GeV
m_π	0.1385 GeV	0.138 GeV	$f_{\rho/\omega}$	0.216 GeV	0.207 GeV
f_π	0.0924 GeV	0.093 GeV	m_{K^*}	0.892 GeV	0.936 GeV
m_K	0.496 GeV	0.497 GeV	f_{K^*}	0.225 GeV	0.241 GeV
f_K	0.113 GeV	0.109 GeV	m_ϕ	1.020 GeV	1.072 GeV
			f_ϕ	0.236 GeV	0.259 GeV

Charge Radii [70]			Strong Decays [103]		
r_π^2	0.44 fm^2	0.45 fm^2	$g_{\rho\pi\pi}$	6.02	5.4
$r_{K^+}^2$	0.34 fm^2	0.38 fm^2	$g_{\phi KK}$	4.64	4.3
$r_{K^0}^2$	-0.054 fm^2	-0.086 fm^2	$g_{K^*K\pi}$	4.64	4.1

$\gamma\pi\gamma$ Transition [95]			Radiative Decays [104]		
$g_{\pi\gamma\gamma}$	0.50	0.50	$g_{\rho\pi\gamma}/m_\rho$	0.74	0.69
$r_{\pi\gamma\gamma}^2$	0.42 fm^2	0.41 fm^2	$g_{\omega\pi\gamma}/m_\omega$	2.31	2.07
			$(g_{K^*K\gamma}/m_K)^+$	0.83	0.99
			$(g_{K^*K\gamma}/m_K)^0$	1.28	1.19

Weak K_{l3} Decay [105]			Scattering Length [106]		
$\lambda_+(e3)$	0.028	0.027	a_0^0	0.220	0.170
$\Gamma(K_{e3})$	$7.6 \cdot 10^6 \text{ s}^{-1}$	$7.38 \cdot 10^6 \text{ s}^{-1}$	a_0^2	0.044	0.045
$\Gamma(K_{\mu 3})$	$5.2 \cdot 10^6 \text{ s}^{-1}$	$4.90 \cdot 10^6 \text{ s}^{-1}$	a_1^1	0.038	0.036

Nucleon Properties [107, 99]			Nucleon Form Factors [108, 100]		
M_p	0.938 GeV	0.94 GeV	g_A	1.27	0.99
μ_p	2.79	2.21	r_E^p	0.89	0.75
μ_n	-1.91	-1.33	r_M^p	0.86	0.75

Table 4.3: Examples of the meson and baryon observables calculated in the DSE approach in exactly the truncation used in this work. The Observables in red are used to fix the model parameters in 4.2 ($\langle\bar{\psi}\psi\rangle$ and f_π) while the pion and kaon masses fix the quark masses of the flavours u/d and s at the renormalisation point (see table 4.1). The remaining parameters are predictions.

5 Hadronic vacuum-polarisation

In the present chapter we apply the method of Dyson-Schwinger equations (DSE) detailed in chapter 3 to the hadronic vacuum-polarisation (HVP) contribution to the anomalous magnetic moment of the muon a_μ .

5.1 Basic definitions

First of all we detail our calculational scheme and provide some definitions that will become relevant for the discussion of the results.

The hadronic polarisation tensor. The first step is to utilize the representation of the self-energy expression (3.30) of the photon-DSE (3.28). The representation is shown in fig. 5.1. There we see that the self energy $\Pi_{\mu\nu}$ can be traced back to the quark propagator S and the quark-photon vertex Γ_μ . The non-Abelian nature of these quantities is not visible explicitly but hidden in the defining equations for the quark and the vertex. For the convenience of the reader we state the definition of the self-energy tensor again

$$\Pi_{\mu\nu}(p) = -e^2 Z_\psi \int_q \text{Tr}[S(q_+) \gamma_\mu S(q_-) \Gamma_\nu(p, q)], \quad (5.1)$$

where p is the photon momentum, q the loop momentum and q_\pm are the quark momenta. The quark propagators S are defined via their rainbow DSE (4.14) and the quark-photon vertex via its ladder BSE (4.19) and the momentum flow in the vertex is as shown in fig. 4.4. The factor Z_ψ is the quark renormalisation constant and is obtained via the renormalisation of the quark DSE (4.14). It has to be noted that the hadronic tensor obtained from a Dyson-Schwinger Equation is one-particle irreducible (1PI).

The self-energy tensor is purely transverse by the WTl $p_\mu \Pi_{\mu\nu} = 0$ and can thus be decomposed as

$$\Pi_{\mu\nu}(p) = \left(\delta_{\mu\nu} - \frac{p_\mu p_\nu}{p^2} \right) p^2 \Pi(p^2), \quad (5.2)$$

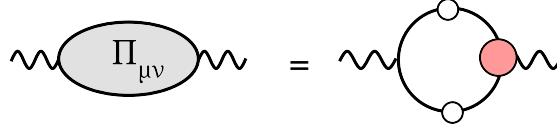


Figure 5.1: The hadronic vacuum-polarisation represented as dressed quark loop with one dressed quark-photon vertex

which serves as a definition of the dimensionless scalar vacuum polarisation function $\Pi(p^2)$. In order to calculate this function numerically we use the transverse projector which has the property

$$\frac{1}{3} \left(\delta_{\mu\nu} - \frac{p_\mu p_\nu}{p^2} \right) \Pi_{\mu\nu}(p) = p^2 \Pi(p^2).$$

Acting with this projector on Eq. (5.1) and performing the integration numerically we obtain the function $p^2 \Pi(p^2)$. The integration is done with straight-forward Gauss-Legendre quadrature in Euclidean spherical coordinates such that only the radial and one angular integration remain nontrivial. This resulting function is however cut-off dependent and has to be renormalised. The divergent terms schematically read

$$p^2 \Pi(p^2) \sim c_1 \Lambda^2 + c_2 p^2 \ln(\Lambda), \quad (5.3)$$

where Λ is the UV cut-off and $c_{1/2}$ are momentum- and cutoff-independent constants. The logarithmic divergence is the one usually seen when dimensional regularisation is used [24, 54]. This is taken care of by the renormalization of the electric charge e and the photon renormalisation constant Z_A^{QED} . On top of that there is an additional quadratic cut-off dependence. This appears since the hard cut-off used in the numerical treatment of the self-energy is a regulator that does not preserve gauge symmetry. This is however not a problem since a non symmetry-preserving regulator can be used in combination with a non symmetry-preserving counter term to maintain the Ward Identities on the level of Green's functions [121]. In other words the non-preservation of gauge invariance is signaled by a photon mass stemming from the term $\Pi(p^2) \sim \Lambda^2/p^2$ in Eq. (5.3). The Euclidean photon propagator has the dressing

$$\frac{1}{p^2(1 + \Pi(p^2))} \sim \frac{1}{p^2(1 + \frac{\Lambda^2}{p^2})} = \frac{1}{p^2 + \Lambda^2}, \quad (5.4)$$

and thus acquires a mass of the order of the cut-off scale Λ . This mass can, however, be renormalised to zero by a non-invariant counter term that would show up as a bare mass in the inverse bare propagator in the photon DSE (3.28) and can be used to subtract the

divergent part. The scheme applied here works excellent as is detailed below. We take care of the quadratic divergences by the prescription

$$[p^2\Pi(p^2)]_{\text{R}} := [p^2\Pi(p^2)] - [p^2\Pi(p^2)]|_{p^2=0}. \quad (5.5)$$

In this way the logarithmic part in (5.3) remains unaffected. Afterwards we obtain the (still Λ -dependent) function

$$\Pi(p^2) := \frac{[p^2\Pi(p^2)]_{\text{R}}}{p^2} \sim c_2 \ln(\Lambda). \quad (5.6)$$

The remaining cut-off dependence can now be removed via

$$\Pi_{\text{R}}(p^2) := \Pi(p^2) - \Pi(0). \quad (5.7)$$

This prescription entails $Z_A^{\text{QED}} = 1$ and $e(\mu^2 = 0) = e_{\text{phys}}$ and thus corresponds to the physical QED on-shell prescription. In order to test the prescription defined above we calculate the perturbative one fermion-loop contribution in QED, which can be found in QFT textbooks (e.g. [54]). In particular we take Eq. (5.1) with bare fermion propagators and two bare vertices. The result is shown in fig. 5.2. It can be seen that the result is cut-off independent for any external momentum sufficiently below the UV-scale. Furthermore the agreement between our numerical prescription and the analytic result is very good. At momenta that are sufficiently below the cutoff the agreement is typically on the order of 0.02 %. In the deep infrared, where $\Pi \approx 0$, the deviation can become large in relative terms. This would become visible if figure 5.2 was shown on a logarithmic scale. The numerical precision in the deep IR is controlled by the quality of the subtraction of the quadratic divergences. We will comment on that in a moment.

Muon $g - 2$ and Adler function. In order to obtain the HVP contribution to the muon $g - 2$ the tensor $\Pi_{\mu\nu}$ has to be folded into the corresponding correction to the muon-photon vertex diagram. This is straightforward since this embedding is perturbative. The resulting expression

$$a_{\mu}^{\text{HVP}} = \frac{\alpha}{\pi} \int_0^1 dx (1-x) \left[-e^2 \Pi_{\text{R}} \left(\frac{x^2}{1-x} m_{\mu}^2 \right) \right], \quad (5.8)$$

can be used once the renormalized function Π_{R} is known [122]. This quantity can also be obtained in a model independent way from experimental data via dispersion relations (DR) [1] which serves as a reference to our calculation. In order to further test our numerics we calculate the well known contribution to $g-2$ from leading order QED vacuum polarisation [2]. This is obtained by using bare vertices, bare electron propagators and $Z_{\psi} = 1$ in the

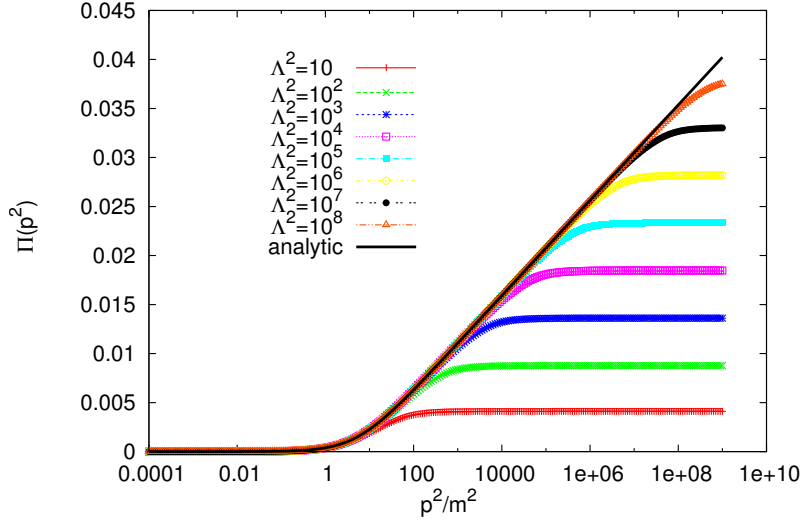


Figure 5.2: Comparison of the numerical definition of the leading QED contribution to the photon vacuum polarisation from a bare fermion loop to the analytic textbook result. The agreement is perfect and the cut-off independence clearly visible. The quantity Π is the renormalised polarisation function and m is the mass of the bare fermion in the loop diagram that defines Π .

definition of $\Pi_{\mu\nu}$ in Eq. (5.1). We reproduce this contribution with a precision of 0.1 %. This indicates that the subtraction of the quadratic divergences and the stability in the deep IR are sufficiently under control.

Another quantity that is a very useful monitoring tool is the Adler function

$$D(p^2) = -\frac{d\Pi_R(p^2)}{d \ln p^2}. \quad (5.9)$$

This function can be extracted from experiment in an essentially model independent way too [1], so that a detailed comparison to 'experiment' is possible that is sensitive to the involved scales, contains non-perturbative, mixed and perturbative regions and allows for an analysis of the contribution of different quark flavours in different momentum regions. The model independent definition of Π_R^{DR} is obtained via the dispersive representation (D-5). From this the corresponding results for the anomaly $a_\mu^{\text{HVP,DR}}$ and for the Adler function $D^{\text{DR}}(p^2)$ can be obtained.

Flavour structure of HVP. Next we want to make some statements about the flavour structure of HVP and the physical degrees of freedom that are important for this object (e.g

mesons in the 1^{--} channel) with regard to the truncation that we work with. As already mentioned before in section 3.2, the fully dressed quark-photon vertex Γ_μ , defined via Eq. (4.19), that appears in (5.1) contains $1^{--}\text{-}\bar{q}q$ bound states for time-like total momenta. Simply speaking this is the case because there is a homogeneous meson Bethe-Salpeter equation that corresponds to any inhomogeneous vertex BSE (the 1^{--} channel in our case). Since this equation has solutions, bound states will automatically occur once a quark anti-quark correlation in the correct channel is part of the Green's function under consideration. The details of how such bound state poles arise have been discussed in section 4.19. This dynamical 'vector meson dominance' in the quark-photon interaction is also a key element for a correct description of the pion form factor, shown in fig. 4.5, as is discussed in [70]. Without this feature the form factor would be very far away from the data for time-like momenta and also much worse in the low-momentum space-like region (e.g. the pion charge radius depends strongly on this feature).

For the calculation of the hadronic tensor $\Pi_{\mu\nu}$ we take into account five flavours, that is u , d , s , c and b quarks. We work in the isospin limit of degenerate u and d flavours. The renormalised masses at $\mu^2 = (19\text{ GeV})^2$ are identical and electro magnetic isospin breaking effects are not present in the truncation. The other, heavier flavours are distinguished by their mass renormalisation condition as shown in table 4.1. Mixing between different flavours does not occur since the interaction kernel (4.5) used in the quark DSE and the BSE's for mesons and for the quark-photon vertex does not depend on flavour. Since the photon does not change flavour quantum numbers, only the flavour-diagonal mesons will appear as intermediate states in $\Pi_{\mu\nu}$. These are the vector mesons ρ , ω and ϕ . In our treatment the ρ and ω are completely degenerate as far as their strong properties are concerned. Their admixture of $\bar{u}u$ and $\bar{d}d$ states are fixed by assigning the correct charge factors. The ϕ is treated as pure $\bar{s}s$ state. In fact we will calculate each contribution to the dressed quark loop separately for every flavour such that the vector states included will be $\bar{u}u$, $\bar{d}d$, $\bar{s}s$ and so on. Since the present truncation is able to describe the vector meson properties with an accuracy on the less than ten percent level (table 4.3) we assume that this will be a reasonable approximation.

5.2 Results

In the present section we show our results for the HVP contribution to anomalous magnetic moment a_μ^{HVP} and the Adler function $D(p^2)$. In particular we take into account five quark flavours u , d , s , c and b . For each flavour the quark DSE (4.14) and the quark-photon vertex-BSE (4.19) are solved and the results are used for the vacuum polarisation (5.1). The charge e is here the charge of the respective quark. The Adler function is obtained via (5.9) and the anomalous magnetic moment via (5.8).

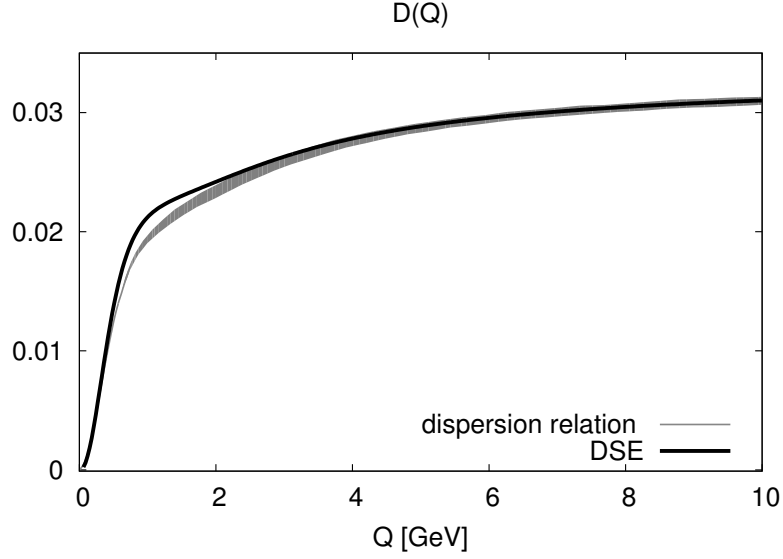


Figure 5.3: The results for the Adler function D calculated with the DSE/BSE framework in this work including five quark flavours (black line) compared to results obtained via dispersion relations in [123, 1] (grey band).

Adler function. In figure 5.3 we show results for the Adler function D calculated in this work within the DSE/BSE approach as well as model independent 'experimental' results that have been obtained via dispersion relations [123, 1]. The DSE/BSE framework in the applied truncation provides a very reasonable description at all scales. The agreement at large momenta is due to the fact that one-loop resummed perturbation theory is included in the effective quark-gluon interaction (4.5) that is used. Also the deeply non-perturbative region is well reproduced. At intermediate scales (around 1 GeV) the DSE result overshoots the DR curve slightly. This is nevertheless a quite reassuring result since all model parameters are fixed previously to meson observables (see table 4.3).

The muon anomaly. In the following we present our result for the muon $g - 2$ from the HVP contribution. This is obtained from the polarisation scalar Π_R via equation (5.8). The integration is performed with straight Gauss-Legendre quadrature. The results for different flavours are summarized in table 5.1. The error quoted for our results is purely numerical and obtained via a variation of the renormalisation prescription from Eq. (5.7). Since we never subtract at exactly zero momentum numerically but at some small scale of $\epsilon = 10^{-7} \text{ GeV}^2$ the condition $\Pi_R(\epsilon) = 0$ could be changed to $\Pi_R(\epsilon) = \delta$ for some small constant δ such that still $\Pi_R(0) = 0$. In fact Π_R exhibits power low behaviour below the mass scale set by

Table 5.1: Results for the anomalous magnetic moment from HVP. Shown are results for different quark flavours as well as their sum as well as the result from dispersion relations (DR) [28]. The parameter set is standard and fixed previously by meson phenomenology. The quark mass definitions used are shown in table 4.1. The error we give for our results is purely numerical is obtained by a variation of the renormalisation condition in the IR, see text.

contribution	ud	s	c	b	$udscb$	DR
$a_\mu^{\text{HVP}} \times 10^{11}$	6740(16)	540(5)	160(34)	3(2)	7440(77)	6949(6)

the internal hadronic degrees of freedom $\Pi(Q^2) \approx \Pi(0) + \Pi'(0)Q^2$, if $\Pi(0) = 0$. We adjust δ such that the power law behaviour continues up to the smallest scales that are accessible to us. The results from this procedure are the ones we quote while the difference to the $\Pi_R(\epsilon) = 0$ result are taken as numerical error. Furthermore we perform this analysis for each flavour separately but the summed result is renormalised only once $\Pi_R^{N_f=5}(\epsilon) = \delta$. This is the reason why the mean values of table 5.1 do not add up exactly. Furthermore the errors are not quite uniform, neither in absolute nor in relative size. But they stay below the 1.1 % level which we take to be our numerical error. The error of all numerical ingredients that are used in the calculation (see Eq. (5.1)) does not exceed that level.

The dominant contribution comes from the up and down quarks which are identical in the isospin limit up to the charge factor. The bottom quark can be completely neglected on the current level of precision. In the Adler function it is, however, important in the perturbative tail at momenta above 6 GeV. The five flavour result is compared to an evaluation using dispersion relations [28]. The deviation is well below ten percent, a systematic uncertainty that is expected given the quality of the model interaction in the vector meson sector that is believed to be closely related to a_μ^{HVP} [124]. In fact the ρ -mass is $m_\rho = 740$ GeV, which is roughly four percent too light. We interpret this as follows: The ρ is slightly too dynamic and can be excited from the vacuum too easily. The contribution the $g - 2$ is thus too large.

The rôle of vector meson dominance. In the following we investigate the rôle of the lowest vector meson states in HVP. As already stated in chapter 3 the quark-photon vertex defined via the BSE shown in Eq. (4.19) has a pole for time-like photon momenta which corresponds to a vector meson bound state. This bound state that appears in the transverse part of the vertex is an important structure of high phenomenological relevance since vector-meson dominance is dynamically included. In particular the vertex can be decomposed into

$$\Gamma_\mu(P, k) = \Gamma_\mu^{\text{BC}}(P, k) + \Gamma_\mu^T(P, k), \quad (5.10)$$

where Γ_μ^{BC} is the Ball-Chiu construction [88] that is dictated by the WTI and regularity. This vertex is thus given in terms of the quark dressing-function only as can be seen in Eq. (3.58). The full basis decomposition used in this work is shown in Eq. (E-4). The transverse part

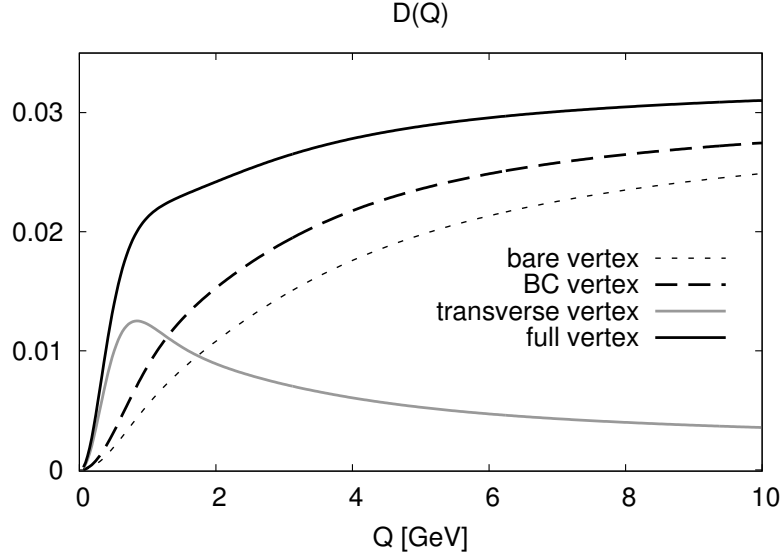


Figure 5.4: The Adler function for different vertices used in the definition of the hadronic tensor (5.1).

obeys $P_\mu \Gamma_\mu^T = 0$. This is the part where the ρ -pole is located. In fact the quark-photon vertex (QPV) can be approximated as

$$\Gamma_\mu(P, k) \approx \Gamma_\mu^{\text{BC}}(P, k) - \frac{f_\rho P^2 \Gamma_\mu^\rho(P \cdot k, k^2)|_{P^2=-m_\rho^2}}{m_\rho(P^2 + m_\rho^2)}, \quad (5.11)$$

which is a reasonable approximation in the vicinity of the pole $-0.4\text{GeV}^2 < P^2 < 0.2\text{GeV}^2$ [70]. Here Γ_μ^ρ is the Bethe-Salpeter amplitude for the respective vector meson, f_ρ the leptonic decay constant and m_ρ the mass of the ρ meson. The relevance of this ρ -pole for the pion charge radius has been investigated in [70] where it was found that it contributes as much as the BC part. A similar analysis has been made for the $\pi^0 \rightarrow \gamma\gamma$ transition form-factor in [95] reaching identical conclusions. In particular this reveals that the quality of the VMD-approximation depends on the relevance of certain kinematic regions.

Now we look into similar matters for the HVP contribution to $g - 2$. In particular we are interested in how different parts of the 'full' vertex from the BSE solution contribute. Therefore we use in the equation for the HVP tensor (5.1) respectively a bare vertex, the Ball-Chiu construction and the transverse vertex. The corresponding Adler functions are shown in fig. 5.4. Obviously neither the bare vertex nor the BC construction are able to reproduce the DR result at low momenta. Instead it is in particular the transverse Vertex Γ_μ^T that contributes dominantly in this regime. Since the vector-meson pole is a dominant feature of the trans-

Table 5.2: Two choices for the light bare quark masses at $\mu^2 = (19 \text{ GeV})^2$ and the resulting meson masses (in MeV) in the pseudoscalar and vector meson sector. For the heavy quarks we always take $m_c = 827 \text{ MeV}$ and $m_b = 3680 \text{ MeV}$ which lead to good results for charmonia and bottomonia in the pseudoscalar and vector channel [96]. Note that the parameters that are changed are the bare quark masses from the Lagrangian of QCD $m_{u/d}$ and m_s . All observables like meson masses follow immediately from that since the true model paraters of the quark-gluon interaction (4.5) are left unchanged.

[MeV]	$m_{u,d}$	m_s	m_π	m_K	$m_{\rho,\omega}$	m_ϕ
set I	3.7	85	138	495	740	1080
set II	11	72	240	477	770	1020

Table 5.3: The leading order HVP contribution to a_μ as obtained by our two sets of bare quark masses for different truncations of the quark-photon vertex.

$a_\mu^{\text{HVP}} \times 10^{11}$	bare	BC	transverse	full
set I	760	1280	6160	7440(77)
set II	720	1120	5640	6760(74)

verse part this result makes a case for VMD since it is the low momentum region that is most relevant for a_μ^{HVP} . In fact the integral (5.8) is already completely saturated below 0.5 GeV. This is further confirmed by the fact that the Adler function from the transverse part has a characteristic bump at a scale close to the ρ -mass at around 800 MeV. It seems natural to assume that this scale is set by the vector meson pole.

Now we look into the contribution of the different vertex parts to a_μ^{HVP} . In addition we consider a second parameter set where we fix the u/d quark mass to obtain the physical ρ -mass of 770 MeV instead of fixing to the pseudo-scalar mass. The s quark mass is fixed to the ϕ -mass. The two parameter sets are for the convenience of the reader summarized in table 5.2. Note that the parameters that are changed are the bare quark masses from the Lagrangian of QCD (renormalised at 19 GeV , shown in red in table 5.2). All observables like meson masses follow immediately through the dynamics of self-consistent equations.

The a_μ^{HVP} results for these two sets are presented in tab. 5.3 where different vertex parts are compared in their importance for this observable. First of all the transverse vertex contributes around 82% to the total result in both cases. Second the result from set II with physical ρ -, ω - and ϕ -masses is closer to the model-independent result from DR (tab. 5.1). Set I deviates about seven percent while Set II has a three percent difference to the DR value. We take this as further evidence for the strong relevance of the vector meson contribution. This is opposite to the conclusion reached within the non-local chiral quark-model (NL χ QM) where the bulk of the contribution was seen in the non-resonant part and the ρ -contribution was found to be negligible [125]. It has to be said, however, that a reasonable result of the

a_μ^{HVP} -contribution there goes at the expense of surprisingly small constituent quark masses. Our result is instead in good agreement with the picture emerging from dispersion relations, since there the ρ and ω resonances are the dominant low-energy features of the cross section $\sigma(e^+e^- \rightarrow \text{hadrons})$. In fact already a simple ansatz for the ρ -part of the cross section gives a result of $a_\mu^{\text{HVP},\rho} = 5400(300) \times 10^{-11}$ and $a_\mu^{\text{HVP},\rho\omega\phi} = 6500(500) \times 10^{-11}$ for the three vector mesons [124]. This is in harmony with our results from the transverse vertex calculation shown in tab. 5.3.

Fitting $\Pi_R(Q^2)$. Furthermore we find that the renormalised scalar polarisation function (taking e.g. up and down flavours only) is very well fitted by $\Pi_{\text{fit}}(Q^2) = \Pi(0) + Q^2 (a/(b + Q^2))$ in the region below $\approx 10 \text{ GeV}$ yielding $\sqrt{b} \approx 880 \text{ MeV}$ for parameter set II. This result is different from the actual mass $m_\rho = 770 \text{ MeV}$. A fit formula of this type is often used in lattice determination of a_μ^{HVP} where sometimes also $b^2 = m_\rho$ is used explicitly. This procedure has been investigated critically in [126] where it was argued that this kind of fitting procedure introduces a model dependence into a calculation that is meant to be *ab initio*. Our findings also suggest that at least taking $b^2 = m_\rho$ could be a source of uncertainty.

Changing the light quark masses. Next we take the idea of changing the bare quark masses in the Lagrangian of QCD a step further and calculate the HVP contribution to the muon anomaly for various quark masses. In particular we change the up/down quark masses leaving the strange quark mass constant and consider the two and three flavour cases only. The motivation is that there is lattice data available for these particular cases [14, 15, 16]. In lattice calculations observables are typically shown as functions of m_π since an extrapolation to the physical point is desired and m_π is typically the smallest physical scale. We show a comparison of our results for $a_\mu^{\text{HVP}, N_f=2,3}$ as function of m_π^2 compared to lattice data in fig. 5.5. Our two curves differ in a constant contribution of 540×10^{-11} coming from the strange quark loop contribution of set I (see table 5.1). It can be seen that there is quite some tension between the data. At least the trajectories towards the physical point seem to be non-universal. In the spirit of what was just said about the importance of vector mesons this can be explained by regarding the dependence of m_ρ on m_π^2 , shown in fig. 5.6. This plot reveals that the relation between vector and pseudoscalar masses is not the same in all approaches. In our interpretation the reason for the fact that some lattice results shown in fig. 5.5 seem to approach the physical point on trajectories that lie quite low is that for these calculations the ρ mass is rather high for certain pion masses (see fig. 5.6). The ρ is thus rather heavy and less dynamical and yields a smaller contribution to a_μ^{HVP} .

Assuming that the vector meson is the important degree of freedom here and that its mass sets the physical scale we investigate the ρ -mass dependence of a_μ^{HVP} . These results are shown in fig. 5.7 and correspond exactly to the data shown before in figure 5.5. That is fig. 5.5 is

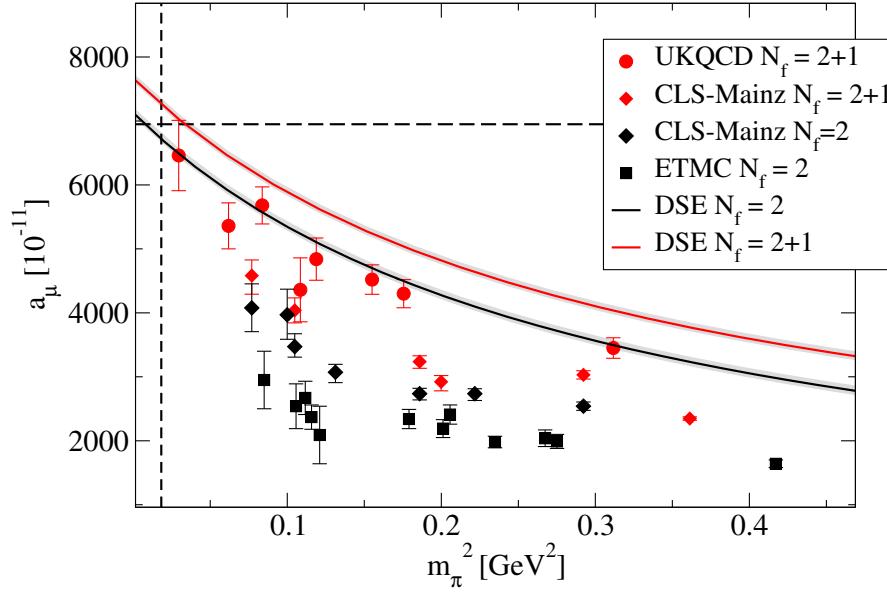


Figure 5.5: The anomaly a_μ^{HVP} as a function of m_π^2 . We compare our DSE results to results from lattice calculations [14, 15, 16]. The physical point ($m_\pi^2 = 0.018$, $a_\mu^{\text{HBP}, N_f=5} = 6949$) is indicated by the dashed lines. The data is divided into the cases $N_f = 2$ and $N_f = 2 + 1$. The grey band represents the numerical error.

translated into figure 5.7 via fig. 5.6. All calculations are done in the isospin-limit of identical up and down masses. Both of our DSE curves ($N_f = 2$ and $N_f = 2 + 1$) are compatible with the corresponding lattice data within error bars. We believe that this nice agreement shows that the DSE approach in the approximation we use captures the dynamics that are relevant for the hadronic contributions to the muon $g - 2$.

In summary we are able to reproduce the dispersion relation result on the less than ten percent level just using the standard parameters of the model that were fixed beforehand to meson phenomenology (see tables 4.3 and 5.2). That is the level of accuracy that is expected by comparison to results in the vector meson sector [89]. We are thus prepared to look into the problem of light-by-light scattering. We expect to be able to reach a similar level of accuracy in this case since we use exactly the same truncation, the same methods, the same objects and the same philosophy there.

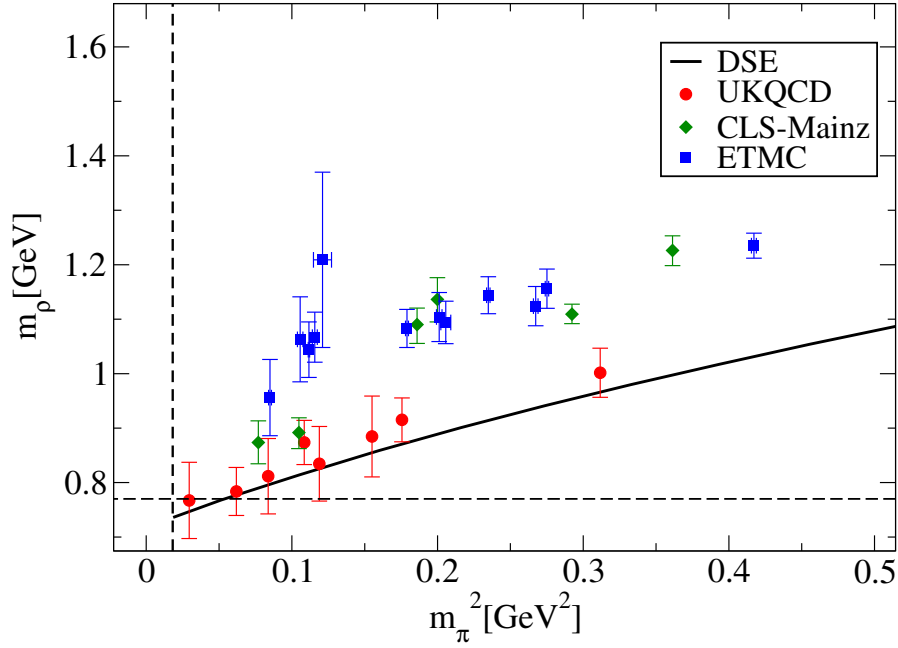


Figure 5.6: The mass of the ρ meson compared to m_π^2 . We compare our DSE results to results from lattice calculations [14, 15, 16]. The physical point is indicated by the dashed lines. The intersection of the DSE curve with the dashed lines defines our two parameter sets (table 5.2), e.g. either choosing m_π or m_ρ to be at its physical value. In the case that we would hit the physical point exactly, the two sets would be identical.

Our final results for the hadronic vacuum polarisation contributions to $g - 2$ are

$$a_\mu^{HVP,I} = 7440(77) \times 10^{-11} , \quad (5.12)$$

$$a_\mu^{HVP,II} = 6760(74) \times 10^{-11} , \quad (5.13)$$

where the error is purely numerical. In set I the u , d and s quark masses are fixed to the pseudo-scalar meson sector while in set II the vector-meson sector is considered. Set I corresponds to the standard parameters of the model (see Eq. (4.5) table 4.3). We take this as evidence that the overall model error can be expected to be on the order of ten per cent.

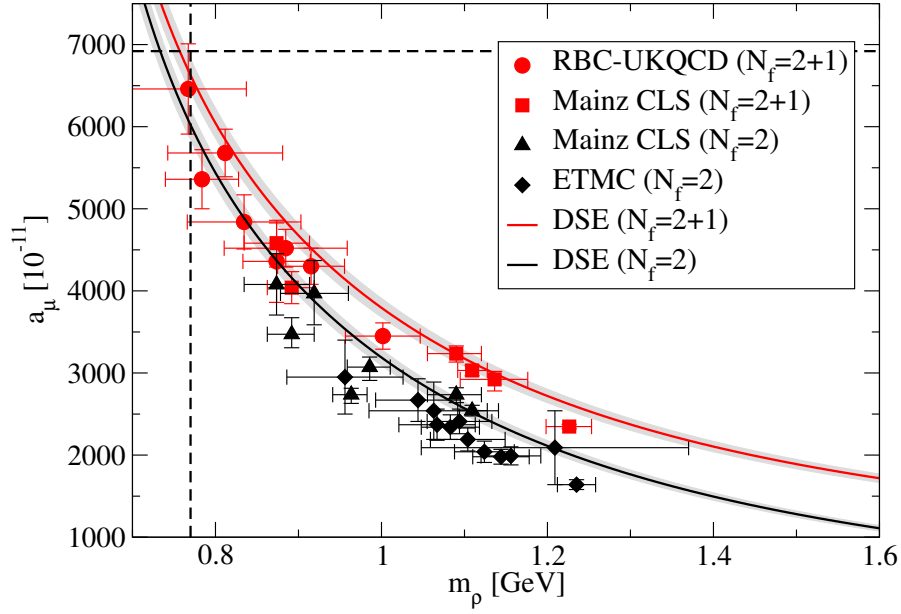


Figure 5.7: The anomaly a_μ^{HVP} is shown for the two flavour and the three flavour case as a function of m_ρ and compared to lattice data from [14, 15, 16]. The $N_f = 2$ data are shown in black and $N_f = 2 + 1$ in red. For the DSE results only the u/d quark masses are changed, the s mass is left constant on $M((19 \text{ GeV})^2) = 85 \text{ MeV}$. The vertical and horizontal lines represents the physical point $(0.77 \text{ GeV}, 6949 \times 10^{-11})$. The curves for the DSE results correspond to a fit through the DSE data points. The grey bands represent the numerical uncertainty .

6 Hadronic light-by-light scattering

In the present chapter we discuss hadronic light-by-light scattering. In particular we elaborate our calculational scheme in detail, discuss further approximations made and present our results. This will be followed by a discussion of our achievement so far, a comparison to results obtained in effective field theory approaches and an outline of future prospects.

The photon four-point function. The central object in the calculation of the hadronic light-by-light (LBL) contribution to the anomalous magnetic moment of the muon is the hadronic photon four-point function $\Pi_{\mu\nu\alpha\beta}$ (see fig. 6.1). This function is a rather complicated object depending on three independent momenta q_1 , q_2 and q_3 with the remaining photon momentum $k = q_1 + q_2 + q_3$. The general tensor decomposition can be summarized as [29]

$$\begin{aligned} \Pi_{\mu\nu\alpha\beta}(q_1, q_2, q_3) = & \Pi_{(1)}(q_1, q_2, q_3)g_{\mu\nu}g_{\alpha\beta} + \Pi_{(2)}(q_1, q_2, q_3)g_{\mu\alpha}g_{\nu\beta} \\ & + \Pi_{(3)}(q_1, q_2, q_3)g_{\mu\beta}g_{\nu\alpha} \\ & + \Pi_{(1)}^{ij}(q_1, q_2, q_3)g_{\mu\nu}q_\alpha^i q_\beta^j + \Pi_{(2)}^{ij}(q_1, q_2, q_3)g_{\mu\alpha}q_\nu^i q_\beta^j \\ & + \Pi_{(3)}^{ij}(q_1, q_2, q_3)g_{\mu\beta}q_\nu^i q_\alpha^j + \Pi_{(4)}^{ij}(q_1, q_2, q_3)g_{\nu\alpha}q_\mu^i q_\beta^j \\ & + \Pi_{(5)}^{ij}(q_1, q_2, q_3)g_{\nu\beta}q_\mu^i q_\alpha^j + \Pi_{(6)}^{ij}(q_1, q_2, q_3)g_{\alpha\beta}q_\mu^i q_\nu^j \\ & + \Pi_{(7)}^{ijkl}(q_1, q_2, q_3)q_\mu^i q_\nu^j q_\alpha^k q_\beta^l. \end{aligned} \quad (6.1)$$

There are three different types of structures in (6.1) depending on whether no, two or four momentum vectors are involved. The indices i, j, k, l take the values 1, 2, 3 so that in the end a total of 138 tensor structures is possible.

The canonical dimension of $\Pi_{\mu\nu\alpha\beta}$ is $D = 0$. On the grounds of naive counting one thus would expect logarithmic divergences in loop contributions. The true degree of divergence is, however, lowered by the correct implementation of the consequences of gauge symmetry. In the case of the perturbative electron-loop contribution to the photon four-point function this can be seen by using dimensional regularisation [24]. Numerically we are bound to use a hard cutoff. This regulator does not preserve gauge symmetry in a similar manner as we already discussed for the case of hadronic vacuum polarisation in section 5 for the photon two-point function $\Pi_{\mu\nu}$ (see Eq. (5.3) and following). There the naive dimension $D = 2$, that is lowered to $D = 0$ for a gauge invariant regulator, resulted in Λ^2 divergences that we had to subtract in order to maintain consistency of gauge symmetry. In the same way a

symmetry-preserving regulator would effectively cause $D = -4$ in the case of LBL [24]. Since all our vertices and propagators approach perturbation theory at high momenta we have the same kind of divergences as in the perturbative QED case just mentioned above. Using a hard cutoff we thus find $\ln \Lambda$ divergences, at least in each of the six possible permutations of diagrams separately. There is however another way in which the finiteness of $\Pi_{\mu\nu\alpha\beta}$ can be deduced from gauge symmetry. Due to Ward-Takahashi identities (WTIs)

$$q_\nu^{(1)}\Pi_{\mu\nu\alpha\beta} = 0 \quad q_\alpha^{(2)}\Pi_{\mu\nu\alpha\beta} = 0 \quad q_\beta^{(3)}\Pi_{\mu\nu\alpha\beta} = 0 \quad k_\mu\Pi_{\mu\nu\alpha\beta} = 0, \quad (6.2)$$

which are a consequence of gauge symmetry, the 138 dressings in Eq. (6.1) are not independent. One can, for example, define all amplitudes as linear combinations of the class (7) amplitudes [29]. Regarding the canonical dimension of $D = 0$ and taking into account the fact that the class (7) amplitudes are accompanied by four momenta $q^{(i)}$ one finds that these must have $D = -4$. Since all other amplitudes follow from these, a finite result can be obtained by a restriction to these tensor structures. This is just another way of understanding how gauge symmetry lowers the naive divergence. This problem will be dealt with in a way laid out in [25, 127] by using the last WTI of Eq. (6.2). This procedure has been already discussed for general contributions in section 2.3 and will be briefly summarized for the case of LBL again below. Further more an exact diagrammatic representation of the four-point function in rainbow-ladder truncation is derived in appendix F.

The muon-photon vertex. For the convenience of the reader we will recapitulate the procedure for projecting the muon-photon vertex onto the anomalous magnetic moment already outlined in section 2.3. In order to obtain the contribution to $g - 2$ we have to consider the corresponding dressing of the muon-photon vertex $\Gamma_\alpha(k)$. That diagram is shown in fig. 6.1. On the muon mass-shell the muon-photon vertex can be decomposed as

$$\bar{u}(p_f)\Gamma_\mu(k)u(p_i) = \bar{u}(p_f) \left[F_1(k^2)\gamma_\mu + iF_2(k^2)\frac{\sigma_{\mu\beta}k^\beta}{2m} \right] u(p_i), \quad (6.3)$$

where u is the muon spinor, $p_{i/f}$ are the incoming/outgoing muon momenta and k is the photon momentum. The muon mass and charge are denoted as m and e . The anomalous magnetic moment corresponds to the form factor $F_2(k^2)$ at zero photon momentum $k^2 = 0$. This can be shown by taking the non-relativistic limit of (6.3) [128, 24]. The result is

$$a_\mu = \frac{g - 2}{2} = F_2(0). \quad (6.4)$$

The expression for Γ_μ corresponding to fig. 6.1 with on-shell muons (momentum $p_{f/i} = p$) and $k = 0$ is

$$\begin{aligned} ie\Gamma_\mu = & \int_{q_1} \int_{q_3} D_{\epsilon\nu}(q_1)D_{\delta\alpha}(q_2)D_{\gamma\beta}(q_3) \times (ie\gamma_\gamma)S(p_1)(ie\gamma_\delta)S(p_2)(ie\gamma_\epsilon) \\ & \times [(ie)^4\Pi_{\mu\nu\alpha\beta}(q_1, q_2, q_3)], \end{aligned} \quad (6.5)$$

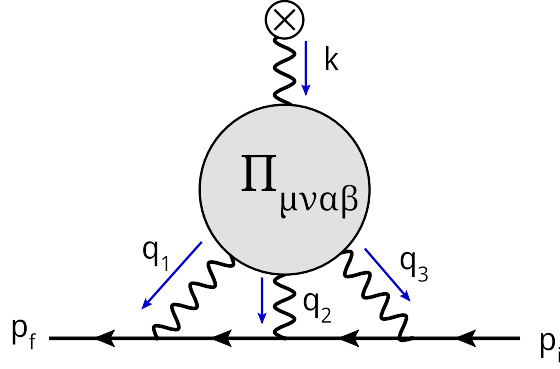


Figure 6.1: The hadronic light-by-light scattering contribution to the anomalous magnetic moment of the muon.

where S are perturbative muon propagators, $D_{\mu\nu}$ perturbative photon propagators and the muon momenta are $p_1 = p + q_1$ and $p_2 = p - q_3$. The photon propagators will be taken to be defined in either Feynman gauge or Landau gauge. Following refs. [25, 127] we use the WTI $k_\mu \Pi_{\mu\nu\alpha\beta} = 0$ to obtain

$$\Pi_{\rho\nu\alpha\beta} = -k_\mu \frac{\partial}{\partial k_\rho} \Pi_{\mu\nu\alpha\beta} =: -k_\mu \tilde{\Pi}_{\rho,\mu\nu\alpha\beta}, \quad (6.6)$$

by taking a derivative of the WTI with respect to k_ρ . The fact that $\Pi_{\mu\nu\alpha\beta}$ is now replaced by its derivative has the advantage of reducing the primitive divergence thus making any contribution explicitly finite. Using the form (6.6) in the expression for the vertex (6.5) one obtains

$$\begin{aligned} ie\tilde{\Gamma}_{\rho,\mu} &= \int_{q_1} \int_{q_3} D_{\epsilon\nu}(q_1) D_{\delta\alpha}(q_2) D_{\gamma\beta}(q_3) \times (ie\gamma_\gamma) S(p_1) (ie\gamma_\delta) S(p_2) (ie\gamma_\epsilon) \\ &\quad \times \left[(ie)^4 \tilde{\Pi}_{\rho,\mu\nu\alpha\beta}(q_1, q_3) \right]. \end{aligned} \quad (6.7)$$

This construction entails that the relation

$$\Gamma_\mu = -k_\rho \tilde{\Gamma}_{\rho,\mu},$$

holds. Finally taking the spin sum for unpolarized muons the desired projection can be shown to be [25]

$$a_\mu = \frac{1}{48m_\mu} \text{Tr} \left[(\not{\epsilon} + m_\mu) [\gamma_\sigma, \gamma_\rho] (\not{\epsilon} + m_\mu) \tilde{\Gamma}_{\sigma,\rho} \right] \Big|_{k=0}, \quad (6.8)$$

which is already written in Euclidean metric here. The relation (6.8) in addition with (6.7) is the one we use in practical calculations.

The content of $\Pi_{\mu\nu\alpha\beta}$. As detailed in appendix F the photon four-point function can be represented in rainbow-ladder truncation of QCD as a sum of two contributions

$$\text{Diagram} = 6 \times \text{Diagram 1} + 12 \times \text{Diagram 2} \quad (6.9)$$

The pre-factors denote the number of permutations that have to be taken into account. These appear automatically during the derivation of the equation though functional derivatives. Later on we will explicitly show the permutations we take into account in the final diagrams that we have to evaluate. The first part is a quark loop that includes dressed quark propagators defined via their Dyson-Schwinger equation (4.14) and quark-photon vertices that are obtained from the vertex-BSE shown in (4.19). Then there is a second class of topologically distinct diagrams that contain additional interactions between opposing quark lines in form of the T-matrix, an object that is defined via its own BSE (3.42). The T-matrix is the connected amputated part of the full $\langle q\bar{q}q\bar{q} \rangle$ Green's function as is explained in section 3.2 and explicitly shown in Eq. (3.35). We wish to emphasize once more that the presentation of the hadronic photon four-point function shown in equation (6.9) is not only consistent with our definition of the hadronic two-point function (5.1) but can be shown to be exactly analogous on the level of truncation that we are considering. This is detailed in app. F.

The essential approximation we will apply to (6.9) and that will be the basis of all considerations and results in the remainder of this chapter is the following: the T-matrix shown in the second diagram in Eq. (6.9) will be approximated via its resonances along the lines of equation (3.44). The fact that this four-point function does contain quark anti-quark bound-state poles can be used to construct an approximation. As is shown in chapter 3 the residues of these poles are given in terms of meson Bethe-Salpeter amplitudes which can be obtained via their Bethe-Salpeter equations. This approximation is much simpler than a calculation of the full T-matrix and makes furthermore contact to previously used approaches such as the ENJL model [29], the chiral constituent quark model (χ CQM) [129], the non-local chiral quark model (NL χ QM) [130, 131], hidden local symmetry models (HLS) [33], effective field theory approaches [36, 37] and holographic models [132]. But it has to be emphasized

at this point that this meson exchange picture in the case of ENJL and $NL\chi QM$ is not a pole approximation. This structure emerges there due to the simplicity of the effective quark four-fermion coupling. Nevertheless the off-shellness of the intermediate mesons is taken into account in full consistency with approximations that are the basis of these models. In our case that is a true approximation that we will overcome in the future. In the meantime we can nevertheless draw some conclusions from a similar case that is known in the literature. Within the same truncation of DSE's a calculation of $\pi\pi$ scattering has been done [133]. There a representation of the four-pion function similar in topology to Eq. (6.9) was found to reproduce Weinberg's low energy results [134]. Furthermore, a resonance approximation of $\pi\pi$ -scattering was carried out [106] where reasonable agreement in the vicinity of the poles was found.

The pole approximation of the T-matrix is exact on the respective meson mass-shell. These poles are of course very dominant features of the function such that a pole-approximation is reasonable in their vicinity. Our assumption here is that especially the pion-pole is close enough to the Euclidean origin that it will be a dominant feature of the T-matrix in the Euclidean domain at low momenta. In particular we denote the poles as in equation (3.44). Graphically this reduces Eq. (6.9) to

$$\text{Diagram} = 6 \times \text{Diagram}_1 + 12 \times \text{Diagram}_2 \quad (6.10)$$

The next step is to take the definition of the $\pi^0\gamma\gamma$ form factor in impulse approximation, consistent with rainbow-ladder truncation [95],

$$F_{\mu\nu}(q_1, q_2) = \text{Diagram}_3 = 2 \times \text{Diagram}_4 \quad (6.11)$$

where two permutations of external photon-legs are included. In this way we arrive at

$$\text{Diagram} = 6 \times \text{Diagram}_1 + 3 \times \text{Diagram}_2 \quad (6.12)$$

The second term includes meson-photon-photon transition form factors as well as meson propagators. In principle all mesons that have the correct quantum numbers, including excitations, have to be included. We limit our selves to the pseudo-scalar channel.

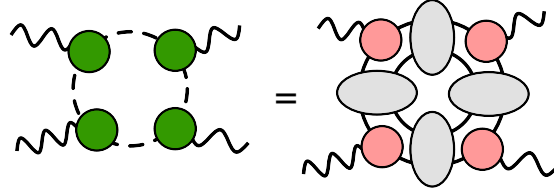


Figure 6.2: Meson loop contributions to LBL as usually considered in hadronic models (see text). On the right side is a corresponding topology given in terms QCD Green's functions. When we approximate the quark-anti-quark T-matrices (grey ovals) on the right side via meson poles (in the same way as described in the text) we arrive at a picture similar to the left side, e.g. similar to hadronic models. The quarks are fully dressed, the graphical representation of the dressing is omitted.

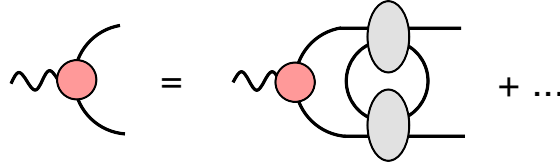


Figure 6.3: Beyond rainbow-ladder QED vertex contribution that gives the ρ meson a finite width self-consistently. The quarks are fully dressed, the graphical representation of the dressing is omitted.

Meson loop topologies. Another class of topologies, that is not included in this truncation, is shown in figure 6.2. The topologies that are generated in the present treatment include infinite, planar gluon ladders. These correspond to the quark loop and the T-matrix diagrams in Eq. (6.9). Internal quark loops are, however, absent. The properties of rainbow-ladder truncation are already built into the decomposition we use (see appendix F). The diagrams corresponding to fig. 6.2 would be generated by a prescription that lies beyond rainbow-ladder. They would show up in an extended interaction kernel that entered e.g. the BSE's for the meson amplitude (fig. 3.6) and the QED vertex (fig. 3.7). The representation of the photon self-energy (5.1) is exact. And the photon four-point function derives from this object (for constant photon background field). The additional diagrammatic ingredients thus have to be hidden in the definition of the quark-photon vertex. The additional interaction kernels would describe a self-consistent decay of the ρ into two pions (see fig. 6.3). On the self-consistent level, the meson loop contributions to LBL would therefore come with vector mesons that have a finite width. This feature is not built in self-consistent in rainbow-ladder truncation.

Using the Feynman rules of rainbow-ladder truncation from table 4.2 we can give example-topologies included in the classes shown above. They are shown in Eq. (6.13), where the

gluons represent effective model gluons, the quarks are bare and the gray dots represent either partial or full summations of gluon ladders.

$$(6.13)$$

Note that only planar gluon ladders are considered in all these diagrams. In terms of an analysis in orders of $1/N_c$, with N_c the number of colours, the upper two classes are of leading order. That is because they contain neither non-planar gluon insertions nor internal quark loops. The third class does contain a quark loop and is therefore $1/N_c$ suppressed. Diagrams with non-planar gluon contributions would be suppressed by $1/N_c^2$ according to the counting scheme [135, 136].

The contribution of pion and kaon loops has been calculated within the ENJL model and was found to be [31]

$$a_{\mu}^{\text{LBL}, \pi/K\text{-loops, ENJL}} = -19(13) \times 10^{-11}. \quad (6.14)$$

We will use this result as an estimate of systematic uncertainties from pieces we are missing in our calculation.

6.1 The PS-exchange contribution.

The π^0 -exchange contribution has been identified as the potentially leading contribution in many studies within the framework of effective field theory [122, 29, 36, 32, 130, 132]. In addition also the η and η' exchange is not negligible [29, 33, 36]. A recent result sees, however, rather tiny contributions of η and η' [131], a reduction that is related to meson off-shell effects. We will discuss this issue later in this chapter. Taken together this contribution will be called the pseudo-scalar (PS) exchange contribution. In general other channels than

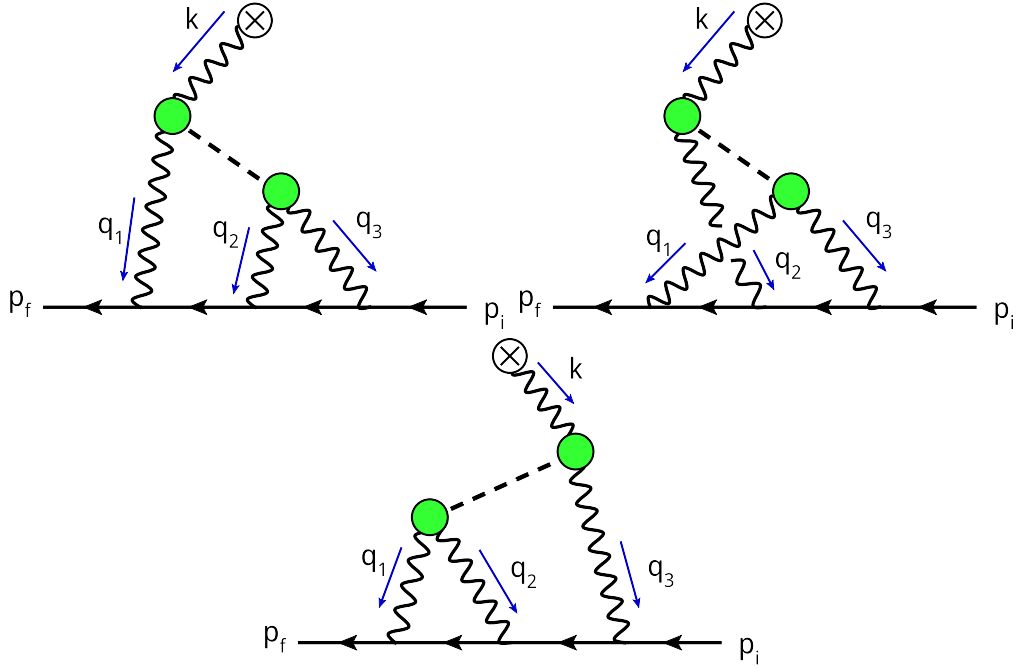


Figure 6.4: Meson pole contributions to light-by-light scattering.

PS do of course contribute. Within the ENJL model scalar and axial-vector meson exchanges have been studied resulting in strongly suppressed contributions [31]. We will not consider them in this work but we will add existing results of the contributions to our systematic uncertainty. In the non-local chiral quark model (NL χ QM) the contribution from scalars was also found to be rather small [137].

The resonant four-point function. The relevant diagrams for meson-exchange, including permutations are shown in figure 6.4. The only object that is needed here is the $\text{PS}\gamma\gamma$ form factor

$$\Lambda_{\mu\nu}^{\text{PS}\gamma\gamma}(k_1, k_2) = i\varepsilon_{\mu\nu\alpha\beta} k_1^\alpha k_2^\beta \mathcal{F}^{\text{PS}\gamma\gamma}(k_1, k_2) . \quad (6.15)$$

The pion form factor is normalised according to

$$\mathcal{F}^{\pi^0\gamma\gamma}(k_1, k_2) = \frac{\alpha_{\text{em}}}{\pi f_\pi} F^{\pi^0\gamma\gamma}(k_1, k_2) , \quad (6.16)$$

where α is the fine structure constant, $k_{1/2}$ are the two photon momenta and f_π the pion decay constant. The normalisation condition holds in the chiral limit for $k_{1/2}^2 = 0$ such that

$F_{\pi^0\gamma\gamma}(0,0) = 1$ [80, 87, 138, 139]. The three diagrams from figure 6.4 have to be evaluated in the form of the five point function $\tilde{\Pi}_{\rho,\mu\nu\alpha\beta}$ in the limit of vanishing photon momentum $k \rightarrow 0$. This result is given in Eq. (6.30) after the introduction of our form factors and a corresponding meson off-shell prescription below.

The $\pi^0\gamma\gamma$ form factor. In order to keep the overview objects that are matrices in flavour-space will be shown with a hat in this section. Within the Dyson-Schwinger approach in rainbow-ladder truncation the $\pi^0\gamma\gamma$ form factor is defined in impulse approximation. It is given as a non-perturbatively dressed quark-triangle (see Eq. (6.11)) [140, 95]

$$\Lambda_{\mu\nu}^{\text{PS}\gamma\gamma}(k_1, k_2) = 2e^2 N_c \int_q \text{Tr} [i \hat{Q}_e \Gamma_\nu(k_2, p_{12}) S(p_2) \times \hat{\Gamma}^{\text{PS}}(p_{23}, P) S(p_3) i \hat{Q}_e \Gamma_\mu(k_1, p_{31}) S(p_3)] , \quad (6.17)$$

where k_1 and k_2 are the outgoing photon momenta, $p_1 = q$, $p_2 = q - k_2$ and $p_3 = q + k_1$ are the quark momenta and $p_{ij} = (p_i + p_j)/2$. The factor two stems from exchange of the two photon vertices and $\hat{Q} = \text{diag}[2/3, -1/3, -1/3]$ is the quark charge matrix, i.e. represents the flavour structure of the quark-photon vertex. Furthermore Γ_μ is the quark-photon vertex obtained from Eq. (4.19) and $\hat{\Gamma}^{\text{PS}}$ the Bethe-Salpeter amplitude for pseudo-scalar mesons. For the relevant flavour diagonal mesons we have the structure

$$\begin{aligned} \pi^0 : \quad \hat{\Gamma}^{\pi^0} &= \frac{1}{\sqrt{2}} \text{diag} [\Gamma^{u\bar{u}}, -\Gamma^{d\bar{d}}, 0] \\ \eta^8 : \quad \hat{\Gamma}^{\eta^8} &= \frac{1}{\sqrt{6}} \text{diag} [\Gamma^{u\bar{u}}, \Gamma^{d\bar{d}}, -2\Gamma^{s\bar{s}}] \\ \eta^0 : \quad \hat{\Gamma}^{\eta^0} &= \frac{1}{\sqrt{3}} \text{diag} [\Gamma^{u\bar{u}}, \Gamma^{d\bar{d}}, \Gamma^{s\bar{s}}] , \end{aligned} \quad (6.18)$$

where the pure quark anti-quark amplitudes $\Gamma^{q\bar{q}}$ are the solutions of the meson-BSE (4.20). In the pseudo scalar channel (0^-) they have the decomposition

$$\Gamma^{\bar{q}q}(P, k) = \gamma_5 [F_1^{q\bar{q}}(P, k) - i \not{P} F_2^{q\bar{q}}(P, k) - i \not{k} (k \cdot P) F_3^{q\bar{q}}(P, k) - [\not{P}, \not{k}] F_4^{q\bar{q}}(P, k)] . \quad (6.19)$$

Since we work in the isospin-limit we have $\Gamma^{u\bar{u}} = \Gamma^{d\bar{d}}$ in addition. In order to rotate the singlet-octet basis to the physical one we apply

$$\begin{aligned} \hat{\Gamma}^\eta &= \cos \theta \hat{\Gamma}^{\eta^8} - \sin \theta \hat{\Gamma}^{\eta^0} \\ \hat{\Gamma}^{\eta'} &= \sin \theta \hat{\Gamma}^{\eta^8} + \cos \theta \hat{\Gamma}^{\eta^0} , \end{aligned} \quad (6.20)$$

where we take $\theta = -15.4^\circ$ [141, 142].

Off-shell prescription. Another fact has to be taken into account. The meson-exchange diagrams in fig. 6.4 clearly show that the momentum that flows through the meson line is in general not on the mass-shell. This is for simple kinematic reasons. The very definition of a meson-exchange thus becomes ambiguous since an off-shell meson does not exist if the underlying theory does not contain mesons as fundamental fields. This is, however, not a conceptual problem in the current framework. The T-matrix is approximated using its dominant pole structure. The residue of these poles happen to correspond to meson Bethe-Salpeter amplitudes. But we don't need to have physical on-shell mesons, rather just branches of poles that reach into Euclidean regime. In order to maintain consistent kinematics we use an off-shell prescription for the meson amplitude. This off-shell prescription is, however, not unique. This fact was already noted in effective mesonic models for LBL [143].

Our reasoning starts with the axial-vector Wari-Takahashi-identity (AXWTI) in the chiral limit that is shown in Eq. (4.17). For the convenience of the reader we show the hereafter needed version in the pion channel ($I = 1$, $I_z = 0$, $a = 3$) again

$$iP_\mu \Gamma_\mu^{5,3}(P, k) = S^{-1}(k_-) \gamma_5 T^3 + \gamma_5 T^3 S^{-1}(k_+), \quad (6.21)$$

where $T^3 = \lambda^3/2$ is the third flavour generator and λ^i are the Gell-Mann matrices. It is obvious that this establishes a relation between the axial-vector vertex and the quark propagator. The axial-vector vertex can be decomposed as [77]

$$\begin{aligned} \Gamma_\mu^{5,3}(P, k) = & \gamma_5 \lambda^3 [\gamma_\mu F_A(P, k) + \not{k} k_\mu G_A(P, k) \\ & - \sigma_{\mu\nu} k_\nu H_A(P, k)] \\ & + \frac{f_\pi P_\mu}{P^2 + m_\pi^2} \hat{\Gamma}_\pi(P, k) + \dots, \end{aligned} \quad (6.22)$$

where the involved pion amplitude is the only non-regular term at $P^2 = -m_\pi^2$. The pion amplitude can be decomposed as

$$\begin{aligned} \hat{\Gamma}_\pi(P, k) = & \lambda^3 \gamma_5 [F_1^\pi(P, k) - i \not{P} F_2^\pi(P, k) \\ & - i \not{k} (k \cdot P) F_3^\pi(P, k) - [\not{P}, \not{k}] F_4^\pi(P, k)]. \end{aligned} \quad (6.23)$$

Note that in the iso-spin limit of degenerate up and down quarks the flavour valued pion amplitude (see (6.18)) is just

$$\hat{\Gamma}_\pi = \frac{\lambda^3}{\sqrt{2}} \Gamma^{\bar{u}u}, \quad (6.24)$$

such that the π amplitude is easily obtained from the pure $\bar{u}u$ amplitude, which is actually defined through the BSE (4.20), via multiplication by a trivial factor. Actually it is the physical

pion amplitude that is normalized according to Eq. (3.44) to reproduce the residue of the pole in the T-matrix. The normalisation of $\Gamma^{\bar{u}u}$ follows via

$$\|\Gamma_\pi\|^2 = \text{Tr} \left[\left(\frac{\lambda^3}{\sqrt{2}} \right)^2 \right] \|\Gamma^{\bar{u}u}\|^2 = \|\Gamma^{\bar{u}u}\|^2. \quad (6.25)$$

Using now the decomposition of the vertex in the chiral limit ($m_\pi^2 = 0$) with explicit pion amplitude in the AXWTI (6.21) together with the parametrisation of the quark

$$S(p)^{-1} = -i\not{p}A(p^2) + B(p^2),$$

one obtains

$$F_1^\pi(P, k) = \frac{B(k_+^2) + B(k_-^2)}{2f_\pi}. \quad (6.26)$$

Here the leading pion amplitude F_1^π is defined also for momenta away from the mass shell $P^2 \neq m_\pi^2$. We extend relation (6.26) by applying it also away from the chiral limit and using it for the sub leading components of the pion (see (6.23)), or rather directly the $\bar{q}q$ amplitudes

$$F_i^{q\bar{q}}(k, P) = \frac{F_i^{q\bar{q}}(k_+, k_+ \cdot P) + F_i^{q\bar{q}}(k_-, k_- \cdot P)}{2}. \quad (6.27)$$

Here the amplitudes $F_i^{q\bar{q}}(k_+, k_+ \cdot P)$ are evaluated on the mass-shell $P^2 = -m_{q\bar{q}}^2$. Similar considerations can be made for the (pseudo) Nambu-Golstone bosons in the other channels. Of course this treatment is less accurate for the η^8 , which is heavier than the π , and even wrong in principle for the η^0 which is no Nambu-Golstone boson in the chiral limit. Since, however, the π^0 is supposed to be dominant, and further the amplitude F_1^π is the dominant piece of the π^0 itself, this approximation seems a reasonable candidate for an off-shell extrapolation. In addition we introduce a damping factor for the three non-leading amplitudes, thus taking note of the mass dimension of these terms. Otherwise the momentum dependent tensor-structure of these amplitudes would cause an unnatural enhancement at high virtualities. The final off-shell meson-amplitude reads

$$\begin{aligned} \hat{\Gamma}^{\text{PS}} = & \gamma_5 \left[\hat{F}_1^{\text{PS}}(p; P) + f(P^2) \left\{ -i\not{P} \hat{F}_2^{\text{PS}}(p; P) \right. \right. \\ & \left. \left. - i\not{p} (p \cdot P) \hat{F}_3^{\text{PS}}(p; P) - [\not{P}, \not{p}] \hat{F}_4^{\text{PS}}(p; P) \right\} \right], \end{aligned} \quad (6.28)$$

where the function f is defined as

$$f(P^2) = \sqrt{\frac{m_{\text{PS}}^2}{P^2 + 2m_{\text{PS}}^2}}, \quad (6.29)$$

thus leaving the on-shell definition of the meson amplitude unaltered. The meson off-shell behaviour is now encoded in the scalar function $\mathcal{F}^{\text{PS}\gamma\gamma}(P^2, k_1^2, k_2^2)$ that depends on three kinematic variables if the on-shell condition for the meson is not demanded. The flavour structure is encoded in the amplitudes \hat{F}_i^{PS} and is given in Eq. (6.18). We are now in the position to define the corresponding five-point function [36]

$$\begin{aligned} \tilde{\Pi}_{\rho, \mu\nu\lambda\sigma}(q_1, q_2, -q_{12}) = & \frac{\mathcal{F}_{\text{PS}\gamma\gamma}(q_{12}^2, q_1^2, q_2^2)\mathcal{F}_{\text{PS}\gamma\gamma}(q_{12}^2, q_{12}^2, 0)}{q_{12}^2 + m_{\text{PS}}^2} \epsilon_{\mu\nu\alpha\beta} q_1^\alpha q_2^\beta \epsilon_{\lambda\sigma\rho\tau} q_{12}^\tau \\ & + \frac{\mathcal{F}_{\text{PS}\gamma\gamma}(q_1^2, q_1^2, 0)\mathcal{F}_{\text{PS}\gamma\gamma}(q_1^2, q_2^2, q_{12}^2)}{q_1^2 + m_{\text{PS}}^2} \epsilon_{\mu\sigma\tau\rho} q_1^\tau \epsilon_{\nu\lambda\alpha\beta} q_1^\alpha q_2^\beta \\ & + \frac{\mathcal{F}_{\text{PS}\gamma\gamma}(q_2^2, q_1^2, q_{12}^2)\mathcal{F}_{\text{PS}\gamma\gamma}(q_2^2, q_2^2, 0)}{q_2^2 + m_{\text{PS}}^2} \epsilon_{\mu\lambda\alpha\beta} q_1^\alpha q_2^\beta \epsilon_{\nu\sigma\rho\tau} q_2^\tau, \end{aligned} \quad (6.30)$$

evaluated in the limit of vanishing external photon momentum $k \rightarrow 0$. This function can now be directly used in Eq. (6.7). The momentum $q_{12} = q_1 + q_2$. The final integration is done with the Monte-Carlo integrator VEGAS [144].

6.2 The quark loop contribution

In the present section we define the non-resonant part of the photon four-point function shown in Eq. (6.12). The corresponding contributions to the muon-photon vertex are shown in fig. 6.5. In addition to these three permutations there are another three, each related to one of the explicitly shown ones by reversion of the spin line. The calculation is conceptually straightforward. The objects that are needed are already to our disposal. These are the same quark-photon vertex (4.19) and the same quark propagator (4.14) as in the hadronic vacuum polarisation (5.1) and in the meson-photon-photon vertex (6.17) above. On the technical side the problem is rather challenging since we have to do a three loop calculation that involves complicated objects that have many tensor structures and non-trivial dressing functions that have been obtained numerically and finally a derivative of that four-point function has to be performed.

In particular the four-point function for the first permutation is defined as

$$\begin{aligned} \Pi_{\mu\nu\alpha\beta}^{(1)}(q_1, q_2, q_3) = & \int_l \\ & \text{Tr}[\Gamma_\mu(k, l + k/2)S(l)\Gamma_\nu(-q_1, l + q_1/2)S(l + q_1) \\ & \times \Gamma_\alpha(-q_2, l + (k + q_1 - q_3)/2)S(l + k - q_3)\Gamma_\beta(-q_3, l + k - q_3/3)S(l + k)], \end{aligned} \quad (6.31)$$

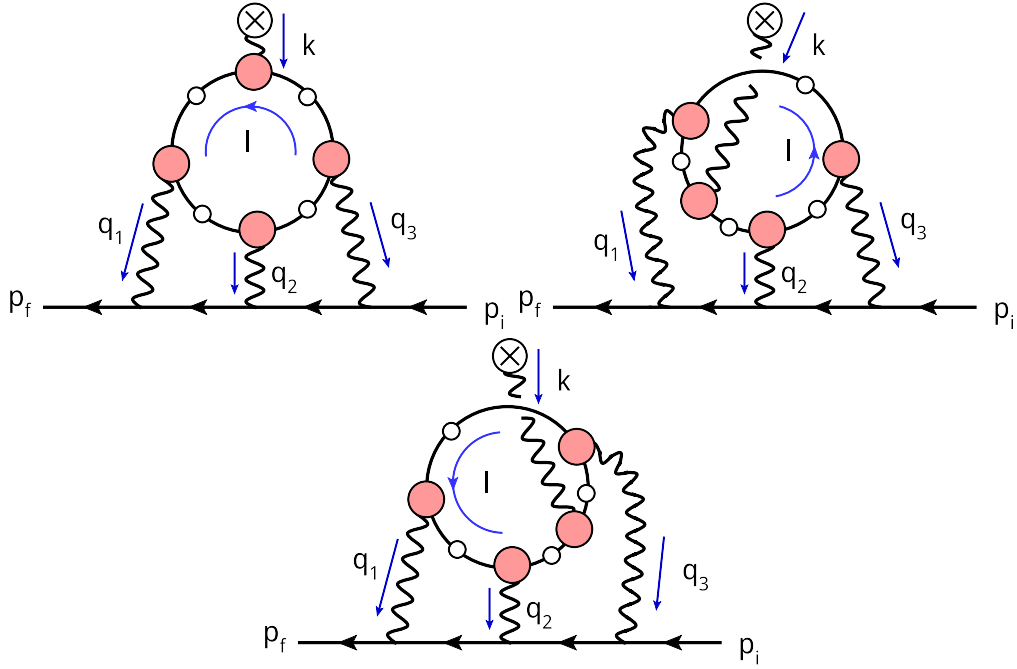


Figure 6.5: Quark loop contributions to light-by-light scattering. In addition to the three permutations shown there is one diagram with reversed fermion spin line for each of the topologies.

where l is the loop momentum, S is the quark propagator and Γ_μ the quark-photon vertex. The other permutations are performed in a similar way by changing the momentum flow and the Lorentz indices. We collect all permutations according to

$$\Pi_{\mu\nu\alpha\beta}(q_1, q_2, q_3) = \sum_i^6 \Pi_{\mu\nu\alpha\beta}^{(i)}(q_1, q_2, q_3).$$

In particular we chose the loop momenta q_1 and q_3 , defined via Eq. (6.7), and l , defined via (6.31) to be

$$q_1 = |q_1| \begin{pmatrix} 0 \\ 0 \\ \sqrt{1 - \eta_1^2} \\ \eta_1 \end{pmatrix}, q_3 = |q_3| \begin{pmatrix} 0 \\ \sqrt{1 - \eta_2^2} \sqrt{1 - \xi_2^2} \\ \sqrt{1 - \eta_2^2} \xi_2 \\ \eta_2 \end{pmatrix}, l = |l| \begin{pmatrix} \sqrt{1 - \eta_l^2} \sqrt{1 - \xi_l^2} \cos \phi_l \\ \sqrt{1 - \eta_l^2} \sqrt{1 - \xi_l^2} \sin \phi_l \\ \sqrt{1 - \eta_l^2} \xi_l \\ \eta_l \end{pmatrix}. \quad (6.32)$$

Here $|q_{1/3}|$ and $|l|$ are further chosen on a logarithmic grid and the angular variables η_i , $\xi_i \in [-1, 1]$. The cutoffs are $|q_i|/|l| \in [10^{-3} \text{ GeV}, 10^3 \text{ GeV}]$. The Monte Carlo routine accepts a D -dimensional array x_i with $x_i \in [0, 1]$ as functional dependence such that a corresponding coordinate transformation has to be used

$$\begin{aligned} |q_1| &= \mu e^{bx_1} & |q_2| &= \mu e^{bx_3} & |q_3| &= \mu e^{bx_6} \\ \eta_1 &= 2x_2 - 1 & \eta_2 &= 2x_4 - 1 & \eta_3 &= 2x_7 - 1 \\ & & \xi_2 &= 2x_5 - 1 & \eta_4 &= 2x_8 - 1 \\ & & & & \phi_l &= 2\pi x_9. \end{aligned}$$

Here $b = \ln \Lambda/\mu$ with μ the infrared cutoff and Λ the ultraviolet cutoff. The final integration measure is

$$\begin{aligned} \mathcal{M} &= Q^4 \frac{d^4 q_1 d^4 q_3 d^4 l}{(2\pi)^{12}} = Q^4 8\pi^2 |q_1|^3 |q_2|^3 |l|^3 \sqrt{1 - \eta_1^2} \sqrt{1 - \eta_2^2} \sqrt{1 - \eta_3^2} \\ &\quad \times b^3 |q_1| |q_3| |l| 2^5 2\pi \frac{d^9 x}{(2\pi)^{12}}, \end{aligned} \quad (6.33)$$

where the first line comes from the hyperspherical coordinate choice and the second line is due to the transformation to the x_i variables. Furthermore Q is the quark charge (i.e. $Q = 2/3, 1/3, \dots$). Note that three trivial angles have been integrated out already that are neglected in (6.32). The quark propagators (4.15) and the quark photon vertices (see app. E) are explicitly defined as Dirac-matrix valued objects in the numerical code. Therefore we make a standard choice of the representation of the gamma-matrices. Objects like $\mathcal{K} = \gamma_\mu l_\mu$ are constructed from that using explicit four vectors like to ones in (6.32). For each momentum configuration the dressings functions are interpolated from a numerical table calculated in advance. We use cubic splines for the quark dressings A and B and trilinear interpolation for the quark photon vertex dressings $\lambda^{(i)}(P^2, k^2, k \cdot P)$. Furthermore the Lorentz indices of the vertices $\Gamma_\mu(P, k)$ are treated explicitly. The contraction of these indices and the Dirac traces are performed numerically inside the code. The same is true for the part that involves the muon and photon lines where we take the photons to be in Landau gauge ($\xi = 0$ in (A-12)). The projector (6.8) is applied to the complete integrand (that is the integrand of (6.7)) before the integration.

The 9 dimensional integrand is then given to the Monte Carlo routine and the integration is performed until convergence on the percent level is obtained. Further more we have to take the derivate of the four point function according to (6.6) and (6.7). Here we perform the derivate numerically on the level of the integrand and integrate numerically afterwards. Writing the hadronic four point function as

$$\Pi_{\mu\nu\alpha\beta}(q_1, q_2, q_3) = \int_l \mathcal{I}_{\mu\nu\alpha\beta}(l, q_1, q_2, q_3), \quad (6.34)$$

we perform the derivate as

$$\left. \tilde{\mathcal{I}}_{\rho,\mu\nu\alpha\beta}(l, q_1, q_3) \right|_{k \equiv 0} = \frac{\mathcal{I}_{\mu\nu\alpha\beta}(l, q_1, \epsilon e^\rho - q_1 - q_3, q_3) - \mathcal{I}_{\mu\nu\alpha\beta}(l, q_1, -q_1 - q_3, q_3)}{\epsilon}, \quad (6.35)$$

where e^ρ is the unit vector in ρ direction and $\epsilon \approx 10^{-5}$ typically. Furthermore $q_2 = k - q_1 - q_3$ was used. The five point function thus becomes

$$\tilde{\Pi}_{\rho,\mu\nu\alpha\beta}(q_1, q_3) = \int_l \tilde{\mathcal{I}}_{\rho,\mu\nu\alpha\beta}(l, q_1, q_3), \quad (6.36)$$

where the l integration is carried out together with the $q_{1/3}$ integration as explained above. To be explicit the final integrand is

$$\mathcal{I}(l, q_1, q_3) = \frac{1}{48m} \text{Tr}[(i\not{p} + m)[\gamma_\mu, \gamma_\rho](i\not{p} + m)\mathcal{I}_{\rho,\mu}(l, q_1, q_3)] \quad (6.37)$$

with

$$\begin{aligned} \mathcal{I}_{\rho,\mu}(l, q_1, q_3) = & \mathcal{M} \times D_{\epsilon\nu}(q_1) D_{\delta\alpha}(q_2) D_{\gamma\beta}(q_3) \\ & \times (ie\gamma_\gamma) S(p_1) (ie\gamma_\delta) S(p_2) (ie\gamma_\epsilon) \times \left[(ie)^4 \tilde{\mathcal{I}}_{\rho,\mu\nu\alpha\beta}(l, q_1, q_3) \right], \end{aligned} \quad (6.38)$$

where $q_2 = -q_1 - q_3$, $p_1 = q + q_1$ and $p_2 = p - q_3$. The external momentum is defined as $p = (0, 0, 0, im)$ with m the muon mass. The integrand $\mathcal{I}(l(x_i), q_1(x_i), q_3(x_i))$ is used by the Monte Carlo routine VEGAS [144] as a function depending on the x_i . The discretized derivative works fine as long as the IR cutoff used in the final integration routine is at least two orders of magnitude larger than ϵ in (6.35), such that the derivative is effectively smooth on all scales that are tested. We have checked the procedure in the case of bare quantities where the derivative can be performed analytically [25] and we were able to reproduce these perturbative results on the permille level. We also compared several cross sections of the nine-dimensional integrands for both cases and found those to agree. Furthermore we compared the numerical derivative technique to analytic derivatives for several cases involving dressed quarks and different vertex dressings. In particular we used either a bare vertex, the first part of the BC vertex or the full BC vertex (3.58). We also found agreement there.

6.3 Results: meson-exchange contribution

Here we present our results for the meson-exchange LBL contribution to the anomalous magnetic moment as obtained in rainbow-ladder truncation of QCD.

First of all we take a look at the off-shell $\pi^0\gamma\gamma$ form factor defined via Eq. (6.17). In particular we plot the function $F_{\pi^0\gamma\gamma}(0, k_1^2, k_2^2)$ (see Eq. 6.16) as a function of $k_{1/2}^2$ and

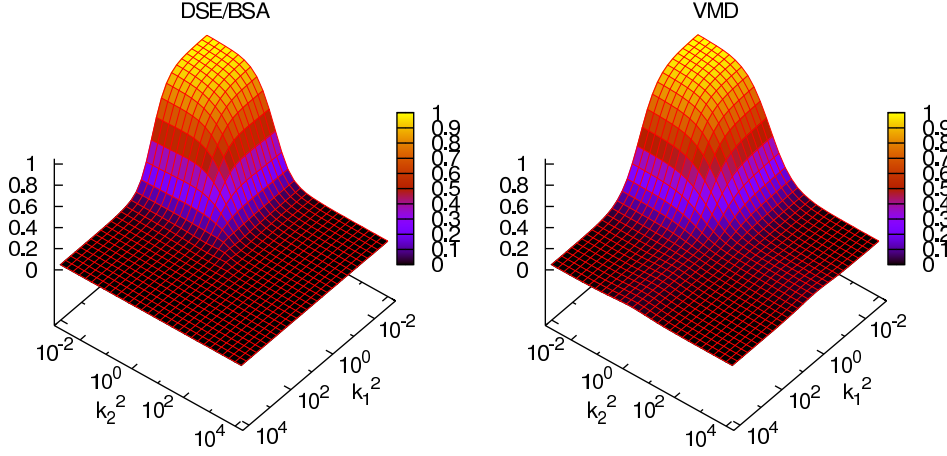


Figure 6.6: On the left are the results obtained in this work for the off-shell $\pi^0\gamma\gamma$ form factor (6.17) compared to a VMD ansatz.

compare to a vector-meson dominance ansatz from Ref. [36]. This comparison is shown in figure 6.6. It can be seen that the general shape is quite similar although there are differences in the details. It has to be noted that $F_{\pi^0\gamma\gamma}(0,0,0) = 1.044 \neq 1$. This is the case since the Euclidean origin $P^2 = 0$ is not the pion on-shell point. The pion on-shell normalization is given by $F_{\pi^0\gamma\gamma}(-m_\pi^2, 0, 0) = 1.004$ [95]. The form factor is thus normalized (on-shell) as expected from considerations stemming from the anomaly [80, 87, 138, 139]. Note that in [131] a suppression of the meson-exchange contribution was found due to off-shell effects. We can not determine these effects consistently in our approach so far. This is because our mesons are not uniquely defined off the mass-shell. In order to answer these issues from the DSE perspective we have to explicitly calculate the T-matrix contribution as shown in Eq. (6.9). This calculation is planned for the future.

The scalar form factor (6.15) can now be used in the representation of the five-point function $\tilde{\Pi}_{\rho,\mu\nu\alpha\beta}$ (6.30) which is then folded into the surrounding QED part as in Eq. (6.7) and projected onto a_μ^{LBL} via (6.8).

The systematic error is determined by the validity of the Maris-Tandy model of the quark-gluon interaction (4.5) as well as the employed off-shell prescription given through (6.27) and (6.29). Since there is no small expansion parameter that could serve as an estimator like in perturbation theory we take the observables that have been calculated successfully as a reference point [94, 102]. In general the model works very well in the Goldstone sector where the numerical error is on the few percent level [92] and quite reasonable in the vector meson sector [89] where the error is typically on the five to ten percent level. In general the masses and decay constants are also well reproduced for the heavier flavours [96]. Note that

the topological contribution to the η and η' masses are not included in the approach in the present truncation. Ways to account for this have, however, already been pursued. In Ref. [84] the $U_A(1)$ problem has been approached from a fairly fundamental point of view. More phenomenological descriptions have been also been presented [86, 81]. The $U_A(1)$ problem is taken into account for in this work by simply taking the experimentally known meson masses in the meson propagators in (6.30).

In addition the flavour decomposition in the meson amplitudes that enter the form factor are phenomenological (see (6.18) and (6.20)). From these considerations we estimate a ten percent systematic error for π^0 contributions and twenty percent for the η and η' . The numerical error has been determined via a variation of the precision of the integration routines and is below the two percent level in the final integration. We take two percent as an estimate. We thus arrive at the following results

$$a_{\mu}^{\text{LBL};\pi^0} = (57.5 \pm 6.9) \times 10^{-11} \quad (6.39)$$

$$a_{\mu}^{\text{LBL};\eta} = (13.6 \pm 3.0) \times 10^{-11} \quad (6.40)$$

$$a_{\mu}^{\text{LBL};\eta'} = (9.6 \pm 2.1) \times 10^{-11} \quad (6.41)$$

$$a_{\mu}^{\text{LBL};\text{PS}} = (80.7 \pm 12.0) \times 10^{-11} \quad (6.42)$$

These results are essentially in good agreement with other approaches. A comparison will be presented below in table. 7.1.

6.4 Quark loop: comparing DSE to NJL

In principal we have all ingredients at our disposal to calculate the quark-loop contribution to LBL in the manner shown in Eq. (6.9). In practice, however, this is quite a difficult task since the numerics are involved. In fact we don't have the full calculation under sufficient control yet and the identification of the sources of numerical error is complicated. Thus we discuss our present understanding of the numerics in detail in order to give the reader an understanding of the technical and physical mechanisms that are associated with the various different propagator and vertex dressings that are part of the non-perturbative three-loop calculation defined through the diagrams of fig. 6.5. In particular the second and third components of the full quark-photon vertex in the basis shown in Eq. (E-4) seem to be the most troublesome. In [20] we showed results for a calculation where these vertex structures have been included. These were results for the Ball-Chiu vertex construction (Eq. (3.58)) which accurately represents the first three structures of the vertex in (E-4). Two independent numerical routines reproduced this result. The contribution was rather large compared to most

estimates. In the meantime we found that in both calculations different sign mistakes have been made that led to the same number in the end. Fixing this sign error, however, yields even negative contributions which seems very unnatural. This indicates that, irrespective of the sign, the contribution from these two vertex structures is not well under control and its size is not determined yet. In addition we found that especially the version with the corrected sign showed unnatural instability under a moderate variation of inputs in form of quark and vertex dressings, which is unexpected. Ultimately we expect the results (for the BC vertex) to be rather stable against variations of the photon gauge parameter and the quark dressing. We thus choose to set this problem aside for the moment and concentrate on the transverse vertex structures (components 5–12 in (E-4)), that we have not analysed in our recent work, in order to get an understanding of what their influence is and from which kinematic regions different contributions come from. In the end we are able to use ten out of twelve vertex structures and we show that their influence can be understood by a detailed comparison to results obtained within the ENJL model and vertex dressings that are inspired by the ENJL model. This is the subject of what follows.

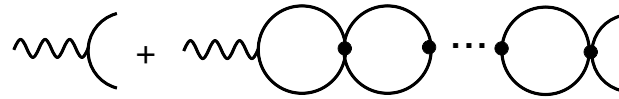
In the following we analyse the influence of different components in the quark propagator as well as the vertex separately and try to give some insight into the different mechanisms that might give important contributions to $g - 2$. In addition we will compare our numerical solutions for the quark propagator and the quark-photon vertex to results obtained withing the ENJL model. In combination with the corresponding results for a_μ^{LBL} this provides additional physical and technical inside into the quark-loop contribution to LBL.

NJL model perspective. A central result obtained withing the ENJL approach [29] is that the vertex dressing of the quark-photon vertex that is associated with transverse vector-meson dominance like form factors gives a rather strong suppression of the quark loop compared to the case of bare vertices. This raises the question whether this mechanism is also found in the DSE approach since, as explained in chp. 4, the vector-meson pole is an important feature in the DSE-vertex. We already saw its influence in the results for HVP in section 5.2.

In the ENJL model the quark propagator is just bare

$$S_{\text{NJL}}(p) = \frac{i\not{p} + m}{p^2 + m^2}, \quad (6.43)$$

for Euclidean momenta p and m the constituent quark mass. The quark-photon vertex is given by a bare vertex and a typical bubble-sum



$$+ \quad \text{wavy line} \text{---} \text{vertex} \text{---} \text{bubble} \text{---} \text{bubble} \text{---} \dots \text{---} \text{bubble} \text{---} \text{vertex} \quad (6.44)$$

where diagrams with any number of loops contribute. The following considerations concerning NJL type models is based on [29, 145]. Thanks to the simple structure of the effective four-quark vertices in that model the bubble-sum does only depend on the Euclidean photon momentum Q and can thus be separated from the left-over bare vertex

$$\Gamma_\mu^{\text{NJL}}(Q) = \gamma_\mu - g_{\text{NJL}} \Pi_{\mu\nu}(Q) \gamma_\nu, \quad (6.45)$$

where g_{NJL} is a coupling derived from the standard NJL couplings and can be found in [145]. The precise form of that coupling won't matter in what follows. The bubble-sum $\Pi_{\mu\nu}$ has the structure

$$\Pi_{\mu\nu}(Q^2) = \left(\delta_{\mu\nu} - \frac{Q_\mu Q_\nu}{Q^2} \right) Q^2 \Pi^T(Q^2) + Q_\mu Q_\nu \Pi^L(Q^2). \quad (6.46)$$

The longitudinal piece $\Pi^L(Q^2)$ vanishes in the limit of identical quark masses [145] and we choose to neglect it for the present purpose. This is essentially what has been done in [29] where the longitudinal pieces have been neglected since $\Pi_{\mu\nu}$ will be contracted with the full photon four-point function which is transverse. The transverse part $Q^2 \Pi^T(Q^2)$ in the VMD limit (see [145]) has the form

$$Q^2 \Pi^T(Q^2) = Q^2 \frac{2f_V^2 M_V^2}{M_V + Q^2}, \quad (6.47)$$

where we neglect also the momentum dependence of the mass function M_V and the decay constant f_V . This VMD limit is a rather good approximation to the momentum dependent case [145]. As far as we can see this is what has been done in the original ENJL work [29]. The expression $2f_V^2 M_V^2$ happens to be equal to $1/g_{\text{NJL}}$ in the limit we consider. Taking everything together the dressed ENJL vertex reads

$$\Gamma_\mu^{\text{NJL}} = \gamma_\mu - \gamma_\mu^T \frac{Q^2}{Q^2 + M_V^2}, \quad (6.48)$$

where the vector meson mass is identified with the ρ mass and γ_μ^T is the transversely projected bare vertex. Under the assumption that the final hadronic photon four-point function is transverse, such that any longitudinal contraction vanishes, the two dressings in Eq. (6.48) can be combined as

$$\Gamma_\mu = \gamma_\mu \frac{M_V^2}{Q^2 + M_V^2} \quad (6.49)$$

which leads to a VMD like suppression that can also be combined with the photon propagator that couples to the four-point function. It is clear that the VMD form factor in Eq. (6.49) gives a suppression compared to the case of using just a bare vertex. This suppression turns out to be quite strong [29]. Corresponding results will be given below. It should be noted

that the bare vertex satisfies the vector Ward-Takahashi Identity (WTI) (3.56) if the quark propagator is a bare constituent propagator with momentum independent mass and trivial wave-function like in the ENJL model. In the following we thus think of (6.48) as a vertex decomposition of a part that follows from the WTI plus a transverse part that has the vector meson pole as a dominant feature. That is exactly what we find in the DSE approach.

While in the work [29] the version (6.49) was taken, we will use (6.48) since it is easier compared with the DSE vertex. These two are identical as long as transversality of the photon four-point function is guaranteed. For a bare vertex (with arbitrary transverse parts in addition) this is the case for bare quarks only. Using dressed quarks does thus violate the WTI if used together with a bare vertex. Only the full BC-vertex (3.58) (the transverse pieces don't matter here) can maintain the WTI if the quarks are fully momentum dependent. The full consistent treatment is of course our goal but, as explained above, not within in reach at the moment. We will nevertheless use several quark and vertex dressings in order to gain an understanding of what their influence is.

Dyson-Schwinger perspective Now we want to compare the DSE solutions to the ENJL case just discussed and see what modifications can be expected. The quark propagator has the covariant decomposition

$$S(p) = \frac{i\not{p} + M(p^2)}{p^2 + M^2(p^2)} Z(p^2), \quad (6.50)$$

with momentum dependent mass function M and the wave function Z . By comparison with Eq. (3.19) we have $M = B/A$ and $Z = 1/A$. It should be noted that the DSE results for the quark propagator are in qualitative agreement with lattice results for the Landau gauge quark propagator [146]. For more advanced truncations even quantitative agreement has been reached [147].

In the truncation used in this work the quark-photon vertex is dressed by a ladder-sum of effective gluons

$$\text{wavy line} \left(\text{quark line} \right) + \text{wavy line} \left(\text{quark line} \right) \cdots \text{quark line} \quad (6.51)$$

If the gluon-exchange interactions are contracted to contact interactions we are back at the NJL picture from Eq. (6.44). Keeping the gluon-exchange character of the interaction makes calculation much more involved. In the NJL case the bubble-sum can be literally resummed as a geometric series of one-loop amplitudes $\sum_n \text{Bubble}^n = 1/(1 - \text{Bubble})$. This does not work in the DSE case. On the other hand a contact interaction effectively reduces the quark anti-quark T-matrix (see fig. 3.5) effectively to a two-point function. It will look like the bubble-sum in (6.44) but with two quark legs on the left instead of the photon. This NJL

T-matrix depends only on one momentum and is also often called a meson propagator. It is in this sense that the T-matrix contribution (6.9) is described as meson-exchange in this model.

The full quark-photon vertex can be written as

$$\Gamma_\mu(Q, k) = \Gamma_\mu^{\text{BC}}(Q, k) + \sum_{i=1}^8 T_\mu^{(i)} \lambda^{(i)}(Q^2, k^2, Q \cdot k), \quad (6.52)$$

where Γ_μ^{BC} is the Ball-Chiu construction (3.58) that follows from the WTI. In addition we have eight transverse pieces that contain the vector meson bound state pole as a dominant feature. An approximation of the quark-photon vertex has been suggested that incorporates the idea of vector-meson dominance (VMD) in Ref. [70]. There the transverse part was approximated by a simple pole term similar to the NJL case (6.47). In the DSE case we have a vector meson Bethe-Salpeter amplitude multiplying the pole such that the relative momentum k of the two quark legs enters the expression. Keeping only the leading part of the meson amplitude (that is γ_μ^{T}) a fit to the transverse part of the quark-photon vertex has been suggested [70]

$$\Gamma_\mu^{\text{fit}}(Q, k) = \Gamma_\mu^{\text{BC}} - \gamma_\mu^{\text{T}} \frac{N_V}{1 + k^4/\omega^4} \frac{f_V}{M_V} \frac{Q^2}{Q^2 + M_V^2} e^{-\alpha(Q^2 + M_V^2)}. \quad (6.53)$$

Here $\omega \approx 0.66 \text{ GeV}$ is a scale that describes the suppression of the amplitude at higher relative momenta, α describes additional suppression at high total momenta and N_V can be extracted by comparison to the vector meson BSA. This formula can be considered to be the VMD limit of the DSE vertex. Nevertheless, as will be seen below, it gives a reasonable representation to the exact self-consistent solution of the function $\lambda^{(1)}$ that is associated with $T_\mu^{(1)} = \gamma_\mu^{\text{T}}$ in Eq. (6.52). Comparing (6.53) to the NJL case (6.48) we see a very similar structure. That is a part that is dictated by the WTI and a part that models the transverse structure as a VMD approximation. The difference is that the WTI part is momentum dependent in the DSE case simply due to the momentum dependence of the quark propagator. In addition mesons are bi-local fields in the DSE case [94] such that the relative momentum dependence is taken into account for both the WTI part and the transverse part.

How will the DSE results differ from the NJL results? Already at this stage we can formulate some expectations that will be tested against numerical calculations below. First of all comparing the quark propagators (6.43) and (6.50) we see some differences. The quark mass function $M(p^2)$ in the DSE case saturates around $M(0) \approx 450 \text{ MeV}$ such that a constituent like mass could be dominant in the integration. But possibly the mass function is tested in different regimes where it is smaller. Actually this will turn out to be the case. In addition $Z(0) < 1$ such that a suppression caused by the wave function is expected,

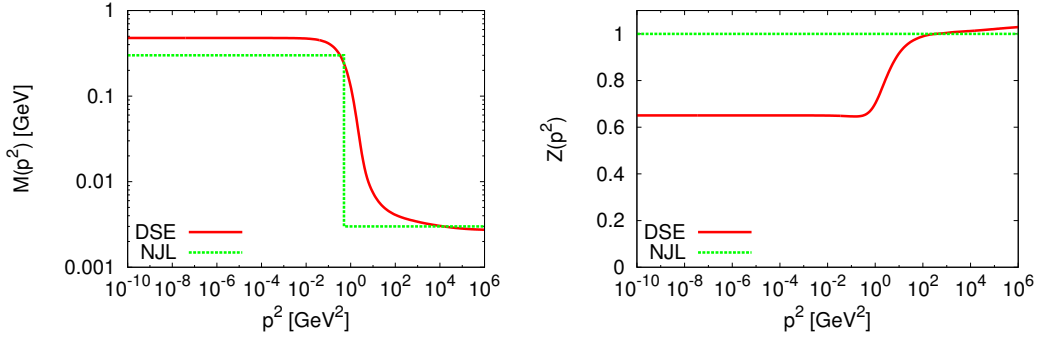


Figure 6.7: Comparison of the mass function M and the wave function Z for DSE and NJL quarks.

depending of course on the momentum regime tested since $Z(p^2 \gg \Lambda_{\text{QCD}}^2) \approx 1$ in Landau gauge. The functions Z and M are shown in figure 6.7. We compare them to NJL type quark dressings which are just constant. That is $Z_{\text{NJL}} = 1$ and the mass changes from a 300 MeV constituent mass to a bare current mass at the NJL cutoff. In accordance with Ref. [29] we choose this cutoff to be at 0.5 GeV .

For the vertices in the VMD limit (6.48) and (6.53) we discuss the 'gauge' part and the 'VMD' part separately. The Γ_μ^{BC} part of the DSE vertex contains additional dressings compared to the bare vertex. The γ_μ structure for example is dressed as

$$\Gamma_\mu^{(1BC)}(Q, k) = \gamma_\mu \frac{A(k_+^2) + A(k_-^2)}{2}, \quad (6.54)$$

with $k_\pm = k \pm Q/2$. Since $Z = 1/A$ so that $A(0) > 1$ this vertex is supposed to give enhanced contributions to a_μ compared to the bare γ_μ . Since furthermore k_\pm are precisely the quark momenta that connect to the vertex a cancellation between the Z -factor of the quark and A -factors of the vertex seems possible (on average). We will argue below that this mechanism is actually observed. The behaviour of the γ_μ part of the quark-photon vertex is also shown in figure 6.8.

For the transverse VMD like parts first of all a suppression is expected also in the DSE case just by comparison to the similar structure of the transverse NJL vertex. In terms of the total momentum Q they look very similar despite the exponential in the DSE part. A comparison is shown in figure 6.9. As can be seen the behaviour as a function of the photon momentum is very similar in the Euclidean low and mid momentum region. The dominant structure arises at the scale $M_V = 0.77 \text{ GeV}$. The exponential suppression of the fit function (6.53) is too fast and the NJL dressing (6.48) has no fall off at all. It will turn out however

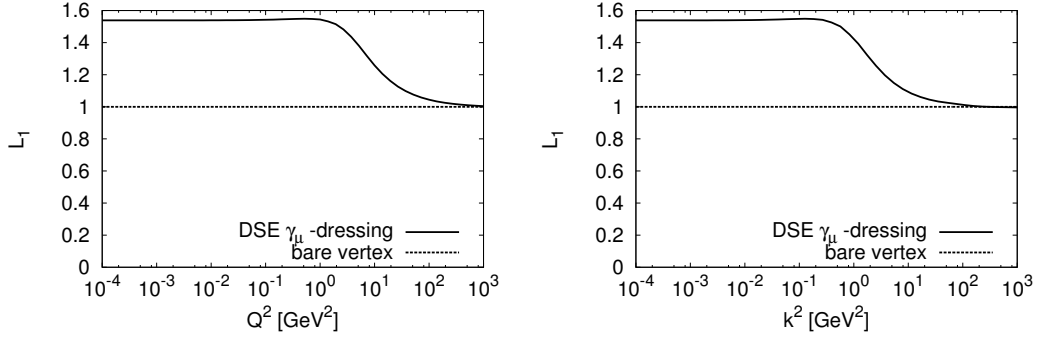


Figure 6.8: Shown is the first dressing (6.54) of the BC vertex (3.58) $L_1(Q, k) = 1/2(A(k_+) + A(k_-))$ as a function of the photon momentum Q^2 and the relative momentum k^2 . To guide the eye we show in addition the constant 'dressing' of the bare vertex used in the NJL model.

that the high momentum behaviour has no strong impact on a_μ such that all three versions are expected to have a similar effect as far as the Q^2 dependence is concerned. A clear difference is marked by the fact that the DSE function depends on the relative momentum as indicated in (6.53). This means that at momenta $k^2 \gtrsim \omega^2 \approx \Lambda_{\text{QCD}}^2$ a suppression of any VMD like effects will take place. In particular this implies the following. Since within the NJL model a suppression due to the transverse structures arise, as is most clearly seen in Eq. (6.49), and since the transverse DSE-vertex parts are supposed to have similar effects (as just explained), we expect a smaller suppression here due to the dependence on the relative momentum. At least if this region (k^2 large) would contribute to the integral significantly otherwise. Just to be explicit we expect less suppression from transverse vertex structures as has been seen in the ENJL model. Of course we can just neglect the k -dependence e.g. $\lambda^{(1)}(Q^2, k^2, k \cdot Q) \rightarrow \lambda^{(1)}(Q^2, 0, 0)$ and thus make the DSE vertex as much NJL-like as possible for the sake of comparison. Also these effects will be studied below.

In order to get an understanding of the regions where the dominant contributions arise we calculate a_μ^{LBL} with various vertex constructions. These include the bare vertex γ_μ the first part of the BC construction (called 1BC) (3.58) as well as the 1BC part together with the transverse piece of the self consistent vertex calculated from its Bethe- Salpeter equation (BSE) (4.19). In other words to most sophisticated vertex we will use differs from the fully self-consistent vertex in that components two and three (the second and third BC parts) are neglected. In addition we analyze the several components and combinations of them. We are interested in the effects the 'gauge' part determined by the WTI has and what the influence of the transverse parts are. Furthermore we consider the running quark dressings. We calculate the momenta and dressings for quark and vertex that the Monte-Carlo routine VEGAS tests

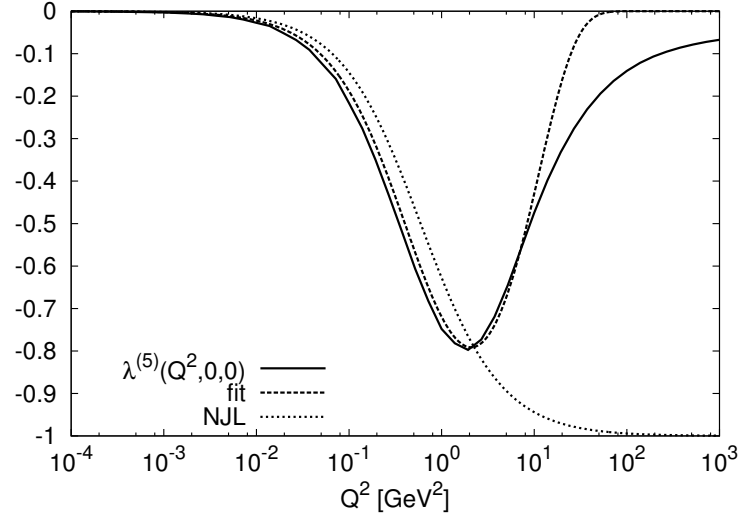


Figure 6.9: Shown is the solution to the dominant transverse dressing $\lambda^{(1)}$ of the quark-photon vertex (6.52) obtained from its BSE (4.19) together with a fit corresponding to (6.53) and the transverse part of the NJL vertex (6.48). Shown is the dependence on the photon momentum Q^2 .

on average. We simply take the mean of these contributions over the Monte-Carlo steps assuming that on average the routine tests the important regions more frequently. Then we repeat the calculations with the dressings replaced by the constant value that turned out to be the mean value in the corresponding case before. If this procedure is able to reproduce the original momentum dependent version this shows that it is reasonable to speak of averaged quantities at all. That is effective quark masses and effective vertex dressings. In addition we can test whether averaged momenta and averaged dressings lie close to the original functions. This would be a useful consistency in the sense that dressings might be not relevant because they are mainly tested in kinematic regions where they are small. In addition it strengthens the trust in our numerics since constant functions are supposed to be numerically more stable. In particular we are able to reproduce for example the perturbative muon- and electron-loop contributions to the muon anomaly with satisfactory precision. This calculation has trivial dressings only.

This method of replacing dressings by their averages has of course some drawbacks. First of all the probability measures for the averaging processes are not known. These are set by the MC routine by looking at the integrand in total. The measures are also not unique. For example we can average the momenta on a linear scale or on e.g. a log-scale. It turns out

that a log-scale is a better choice. This can be seen by the much better correlation between log-averaged momenta and the corresponding dressings. That is we find e.g.

$$\langle M(p^2) \rangle \approx M(10^{\langle \log p^2 \rangle}) \quad (6.55)$$

$$\langle M(p^2) \rangle \not\approx M(\langle p^2 \rangle), \quad (6.56)$$

which seems reasonable since all dressings show characteristic behaviour on log-scales not on linear scales. Furthermore an inconsistency might arise due to the fact that an averaged dressing changes the integrand such that the integration routine feels forced to look in different regimes than in the case of momentum dependent dressings. In order to make sure that a sensible interpretation of the results is possible from that averaged perspective we will carefully look at all the different results discussed below.

To be precise we illustrate the averaging a little more explicit. In the case of the quark propagator we will work with the expression

$$S_{\text{av}}(p) = \frac{i\not{p} + \langle M \rangle}{p^2 + \langle M \rangle^2} \langle Z \rangle, \quad (6.57)$$

where the averaging is always done under appropriate conditions. That is if we do the averaging for M and Z with 1BC vertex dressing then these averages $\langle M \rangle_{\text{1BC}}$ and $\langle Z \rangle_{\text{1BC}}$ are only used together with the 1BC vertex dressing in a calculation. If another vertex is used together with an averaged quark we do the averaging with this other vertex. Furthermore if we do calculations with $M = \langle M \rangle$ and $Z = 1$ in Eq. (6.57) then the averaging for the mass function M is also done with $Z = 1$, that is $\langle M \rangle = \langle M \rangle_{Z=1}$.

Note that the averaging is only used as a tool to obtain information about the influence of certain dressings. It helps to 'project' complicated problems onto simpler ones. We try to answer certain questions in this way, for example, whether our momentum dependent quark can be considered to be related to a constituent quark with a certain mass in an approximate sense. In this way statements about e.g. the quark being tested mainly in certain kinematic regimes become more precise. For our final calculations we take of course all momentum dependence into account.

6.5 Results: Quark loop contribution

Now we come finally to the presentation of our LBL quark-loop results which we discuss along the lines developed in the preceding section. We will consider the contribution of up and down quarks only here since these typically yield the major contribution of about 90% [20] and we are interested in the qualitative and semi-quantitative behaviour of the different

Table 6.1: Results for the quark loop LBL contribution using a bare vertex and various dynamical and averaged or constant quark dressings. In the case of dynamical Z and M we always took the solutions of the quark DSE for up/down quarks. The averaged quantities are then calculated on the fly.

	Dressing	$\langle p \rangle [GeV]$	$\langle Z \rangle$	$\langle M \rangle [GeV]$	$\sqrt{\langle M^2 \rangle} [GeV]$	$a_\mu \times 10^{11}$
1	Z and M dynamical	2.9	0.83	0.072	0.14	53
2	$Z = 1$, M dynamical	1.5	1	0.12	0.18	102
3	$Z = 1$, $M = 0.477$	1.9	1	0.477		22
4	$Z = 1$, $M = 0.21$	0.9	1	0.21		91
5	$Z = 1$, $M = 0.3$	1.2	1	0.3		51

vertex components. We assume that for each case that will be considered the heavier flavours will increase the result by about 10%.

Bare vertex. We first of all consider bare vertices in order to analyze the influence of the quark propagator. In particular we are interested in the separate behaviours of the dressings Z and M defined in Eq. (6.50). The results for various averaged and dynamical dressings are shown in table 6.1. Note that the dynamical Z and M functions are always the solution of the quark DSE (4.14) where the mass function renormalisation condition corresponds to the light up/down quarks. We first consider the case $Z = 1$ and perform the Monte-Carlo integration. The result (second line of table 6.1) is $a_\mu \approx 100 \times 10^{-11}$. This does not correspond to an effective mass close to the infrared limit $M(0) = 0.477 GeV$, as one might have thought given the behaviour of the mass function. This effective mass yields a much smaller number (third line in the table). Instead the result corresponds to a mass of $M_{\text{eff}} \approx 0.2 GeV$ (compare to line 4). Thus it seems that the momentum dependent mass is tested at momenta above the infrared plateau (see fig. 6.7). This is in rough agreement with the quadratic average of $\sqrt{\langle M^2 \rangle} = 0.18$ in line 2. Also the averaged quark momentum seen in table 6.1 points in that direction. It should be noted, however, that the averaged mass for the $Z = 1$ case is $\langle M \rangle \approx 0.12 GeV$ which is clearly not compatible with the effective mass being $0.2 GeV$. The quadratic averaging thus seems to be preferable here. Now we look into the influence of the wave function Z . The result for fully dynamical quarks is found in line one and yields $a_\mu \approx 50 \times 10^{-11}$. The wave function apparently leads to a suppression by a factor $1/2$. This seems reasonable since $\langle Z \rangle = 0.83$. There are four quarks in the loop and thus the wave function enters the calculation four times, resulting in $0.83^4 \approx 0.5$. This explains the difference to the case of $Z = 1$ shown in the second line.

We thus note two things. The result with bare vertices and dressed quarks reproduces the result expected for bare constituent quarks of mass $M = 0.3 GeV$ (last line of table 6.1)

Table 6.2: Results for the quark loop LBL contribution using the 1BC vertex dressing (6.54) and various dynamical and averaged or constant quark dressings. In the case of dynamical Z and M we always took the solutions of the quark DSE for up/down quarks.

	Dressing	$\langle p \rangle [GeV]$	$\langle Z \rangle$	$\langle M \rangle [GeV]$	$a_\mu \times 10^{11}$
1	Z and M dynamical	1.55	0.76	0.13	104
2	$Z = 1$, M dynamical	1.04	1	0.17	206
3	$Z = 1$, $M = 0.21$	1.55	1	0.21	196

which seems reasonable at first sight [148]. This agreement is, however, a non-trivial one. The dynamical quark mass is tested in a region where $M(p^2) \approx 0.2 GeV$ which is considerably smaller. This results in a contributions that is larger by a factor two. The non-trivial wave function Z on the other hand counteracts that effect and leads to a reduction by roughly the same factor again. It is thus the interplay between mass function and wave function that determines the result in the end.

Comparing this now to the ENJL calculations [29] the question arises how this effect would be seen there. In this calculation they consider the low-energy and the high-energy contribution separately, where the VMD vertex dressing is used for the low-energy part only. Since we are not interested in the VMD influence right now we will discuss these results later and instead only consider the effective quark masses that are tested in these two contributions. For the low-energy part a constituent mass of $M \approx 0.3 GeV$ is used together with a momentum cutoff of $0.5 GeV$ in the photon legs. For the high-energy part a bare perturbative quark-loop is taken. Instead of a small current quark mass, however, they use a mass of $1.5 GeV$ which is supposed to be an effective infrared cutoff for the integral. Taking now into account that our quark, that is defined on all scales and looks very similar to lattice results, is tested mainly at masses of $0.2 GeV$ it seems clear that the NJL model is missing some contribution since effectively their mass is always $M > 0.3 GeV$. That is it seems that increasing the cutoff for the low-energy part beyond $0.5 GeV$ while at the same time allowing $M < 0.3 GeV$ opens new important integration regions.

Gauge part of the vertex. Now we look into the gauge part of the vertex that is demanded by the WTI. We restrict ourselves to the 1BC dressing (6.54) of the γ_μ term for reasons explained already above. All the results we discuss in this paragraph can be found in table 6.2. First of all we look into the influence of the vertex dressing. Therefore we compare bare and 1BC dressings as well as trivial and an non-trivial wave function Z , but use only full dynamical masses M . The result for fixed $Z = 1$ and dynamical mass (second line of the table) is roughly twice as big as the corresponding bare vertex result we just presented in the second line of table 6.1. Here the enhancing influence of the 1BC vertex dressing is clearly

visible. The same is true for the cases with dynamical Z function (first lines of both tables).

Next we look into the effective quark mass that is seen in this contribution. In particular we take the case with $Z = 1$ in the second line of table 6.2 as a reference since there the dynamical mass only interacts with the vertex dressing. Again we find that a bare mass of $M \approx 0.2 \text{ GeV}$ does the same job as shown in the table in the third line. This seems in rough agreement with the averaged mass $\langle M \rangle = 0.17 \text{ GeV}$ from the dynamical case in line two. A bare mass corresponding to the infrared plateau of the mass function $M(0) = 0.477 \text{ GeV}$ fails completely and even gives negative results (not shown). This could indicate some inconsistency since the 1BC vertex is only strictly valid for one particular mass function which has only one particular averaged value (0.2 GeV in our case).

Finally we answer the questioned posted in the last section whether the effects of the 1BC vertex dressing and the quark wave function do compensate to some extent. Quarks with $Z = 1$ and bare vertices yield (second line of table 6.1) $a_\mu \approx 100 \times 10^{-11}$. Taking the dynamical wave function into account (first line of the same table) reduces this two $a_\mu \approx 50 \times 10^{-11}$ while the 1BC dressing increases a_μ to $\approx 100 \times 10^{-11}$ again as can be seen in the first line of table 6.2. Alternatively we can take into account the 1BC dressing before employing the dynamical wave function which brings us to the second line of table 6.2 with $a_\mu \approx 200 \times 10^{-11}$. Then the non-trivial wave function in addition yields again the result of the first line in that table. The compensation of momentum dependent wave function $Z(p^2)$ and the 1BC vertex dressing thus happens quite accurately.

The suppression due to the wave function can be explained via an average effect at least qualitatively in the case of 1BC dressing. The average $\langle Z \rangle = 0.76$ in the first line one of table 6.2 yields a suppression of $0.76^4 \approx 0.33$ whereas the actual suppression compared to the second line with $Z = 1$ is 0.5. The suppression from the averaged Z would thus be too strong. Comparing the averaged masses in the first and second line of that same table seems to suggest that the suppression of 0.33 is softened by a smaller effective mass $\langle M \rangle = 0.13$ in the case of dynamical Z . Clearly the different dynamical dressings interact in a non-linear way and the interpretation of averaged dressing effects has to be made careful. Nevertheless the simplified viewpoint gives insight into the dynamics at work.

The full Ball-Chiu vertex. We do not give final results for vertex constructions concerning the second and third BC vertex components (3.58) in this work. In fact it turned out that there was a sign mistake in our results published in [20] despite the fact that two independent numerical evaluations have been done. In both numerical programs different mistakes have been made that effectively changed the signs of the second and third terms of the BC vertex. This happened since there was a misunderstanding in terms of the conventions used for the

propagator and the vertex basis (e.g. (E-4)) used. From the corresponding WTI (3.56) it is clear that a convention for the quark (6.50) fixes the gauge part of the vertex (3.58) including pre factors. This relation was violated in both numerical treatments.

Furthermore, one might expect some stability of the results under (at least mild) variations of the quark dressing functions used. As an example take our results for the compensation of wave function and 1BC dressings just studied above. Another example is the $\pi\gamma\gamma$ transition form factor. In a simple truncation, where the BC Vertex is used as approximation for the quark photon vertex, the (correct) infrared normalisation $F_{\pi\gamma\gamma}(0,0) = 1$ (see Eq. (6.16) is even independent of the details of the quark dressing, as can be shown analytically [149]. For this reason one might expect some stability of the contribution a_μ^{LBL} with respect to the quark dressing, which we found for the BC Vertex with wrong sign by using a quark propagator from a different, even much more sophisticated truncation. Correcting the sign mistake in the second and third BC dressings, however, resulted in negative contributions to a_μ^{LBL} which is rather unexpected. Furthermore the result is quite sensitive to the quark input used. We take this as a sign that numerical stability is not reached for this case. We were not yet able to locate the source of the problem. Unfortunately the three-loop integrand is very complicated and thus very difficult to search for problematic regions.

On the other hand we started a calculation of the quark loop LBL contribution a_μ^{LBL} using the naive projector (2.14). This technique seems to be inferior. First of all more integration variables are needed since there is one more external scale (that is the external photon momentum k) such that the convergence of the Monte Carlo routine is much slower. Furthermore the singularity of the projector (2.14, 2.13) as a function of k has to be cancelled numerically against the full photon four-point function $\Pi_{\mu\nu\alpha\beta}(q_1, -q_1 - q_2 - k, q_2)$ in the limit $k \rightarrow 0$. After all we were not able to reliably perform this limit numerically yet in a satisfactory way. We did this calculation for the bare muon loop LBL contribution and for various dressed quark loop contributions. We found rather strong dependence on k and were able to reproduce the corresponding results (using the projector (2.12)) at best on the 20 – 30% level. Since these results are not under control and since we have not performed a detailed study of them yet we do not cite any numbers here. We found a hierarchy of quark loop results very similar to the results quoted in this section. But surprisingly the result for the BC Vertex was different there. In fact it was very similar to the 1BC result shown in line one of table 6.2 probably slightly larger. Now since this numerical treat is very premature it would be wrong to jump to conclusions here. But if this were to be the case this could be an indication were to look for the numerical problem. In fact the two projection methods pronounce different momentum regions. Both methods differ in the dimension of the integral of the quark loop. The naive projection (2.14, 2.13) calculates $\Pi_{\mu\nu\alpha\beta}$ directly, in which case the integral is $\log \Lambda$ divergent with the cut off. The divergence cancels, however, in the final integration [25] between the six different diagrams. The other method (2.12) takes instead the momentum derivative of the four-point function (6.6) which is manifestly convergent.

The former method thus pronounces the UV, while the latter focuses more on the IR. This can in fact be observed by plotting the momentum range mapped out by the Monte Carlo routine. It might thus be possible that the numerical problem with the BC vertex dressing is located in the IR. In fact the integrand becomes constant in the IR, as function of the radial Euclidean loop momenta, for fixed angular coordinates. A cancellation of the angular integral thus seems to be necessary. Furthermore we carried the derivative of the quark loop diagrams also analytically for the case of BC vertices. The results were similar and did not provide additional insight besides that the numerical derivative we use (6.35) works as expected.

In fact we find results 1BC and BC in the calculation to HVP that differ by about 5% (not shown in the corresponding chapter). There seems thus to be the possibility that our BC results in [20] are just a numerical fluke and the result should be close to the 1BC result. We emphasize, however, that any conclusion on this subject is premature at the moment. For this reason we proceed step by step with the transverse vertex dressings in the following and give simple arguments in favour of the different results we obtain.

Transverse vertex components. We now look into the transverse vertex components. As discussed above a suppression of the LBL contribution to $g - 2$ is expected due to the transverse structures in analogy to the ENJL case [29]

$$a_{\mu}^{\text{LBL,ql,ENJL}} = 21(3) \times 10^{-11}. \quad (6.58)$$

In the following we compare our results to (6.58). In order to proceed slowly and carefully we look into the potentially leading transverse structure γ_{μ}^T first. We combine this structure with a bare vertex and the 1BC dressing. In addition we use the NJL-like dressing (transverse piece of (6.48)) for the transverse vertex and look into the dependence on the relative momentum. To make the comparison to the NJL case as good as possible we approach the NJL case from the DSE side by neglecting the relative momentum dependence in the transverse dressing. In addition we introduce a relative momentum suppression like the one in Eq. (6.53) $\sim 1/(1 + k^4/\omega^4)$ in the NJL dressing to make sure we understand its effect. The results to be discussed can be found in table 6.3. All calculations are done with fully dynamical quarks that is mass function and wave function momentum dependent.

Bare vertex and transverse structures. First of all we see in line five of table 6.3 that using the NJL-VMD transverse dressing from Eq. (6.48) gives the desired suppression. This result is close to what was found in the NJL model (6.3). Adding ten percent as a rule of thumb to take into account the heavier flavours (strange and charm) we get $a_{\mu}^{\text{LBL}} \approx 19 \times 10^{-11}$. Obviously we can reproduce the ENJL results numerically. Taking instead the leading transverse structure $\lambda^{(1)}$ from the BSE solution of the vertex (4.19) yields $a_{\mu} = 47 \times 10^{-11}$, as shown in

Table 6.3: Bare and leading transverse vertex as well as bare and full transverse vertex compared to NJL dressings. Quarks are always fully dynamical. $\lambda^{(1)}$ is the dressing of the γ_μ^T part obtained from the vertex BSE and $\lambda_{\text{NJL}} = -P^2/(P^2 + M_V^2)$. In addition $f(k^2) = 1/(1 + k^4/0.66^4)$. P and k are the total and relative momenta of the vertices, L_1 is the dressing of the bare vertex (one is this case) and T_1 is the leading transverse dressings corresponding to γ_μ^T (either $\lambda^{(1)}$ or λ_{NJL}). P , k and M are given in units of GeV .

	Dressing	$\langle M \rangle$	$\langle P \rangle$	$\langle k \rangle$	$\langle L_1 \rangle$	$\langle T_1 \rangle$	$a_\mu \times 10^{11}$
1	$\gamma_\mu + \gamma_\mu^T \lambda^{(1)}(k^2 = 0)$	0.029	0.022	25.7	1	-0.1	16
2	$\gamma_\mu + \gamma_\mu^T \lambda^{(1)}$	0.062	0.029	3.3	1	-0.029	47
3	$\gamma_\mu + \Gamma_\mu^T(k^2 = 0)$	0.029	0.023	25.6	1	-0.106	13
4	$\gamma_\mu + \Gamma_\mu^T$	0.077	0.03	2.68	1	-0.03	46
5	$\gamma_\mu + \gamma_\mu^T \lambda_{\text{NJL}}$	0.035	0.022	19.9	1	-0.098	17
6	$\gamma_\mu + \gamma_\mu^T \lambda_{\text{NJL}} \times f(k^2)$	0.067	0.031	3.05	1	-0.013	51

line two of that table. This is only marginally smaller than the pure bare vertex result from line one of table 6.1. In addition we also show a calculation that takes the full transverse vertex with eight tensor structures into account, shown in line four of table 6.3. This gives only a small correction to the leading transverse terms such that the γ_μ^T part seems to be leading in this case. In order to get an understanding of the difference to the NJL case we simply neglect the relative momentum dependence of the transverse terms. They are evaluated at $k^2 = 0$ and $k \cdot P = 0$. No matter whether the leading (line one) or the full transverse structure (line three) is used we get a result that is close and even below the NJL case. A strong suppression is observed. To approach the same idea from the opposite side we attach the suppression factor to the NJL dressing as already mentioned above. The result, shown in line six, again brings us very close to the picture obtained from DSE's with a result that is only marginally smaller than the bare vertex case. The dependence on the relative momentum is thus crucial for the amount of suppression that is to be expected from the transverse vertex parts or in other words from VMD-like influences. In fact the results of table 6.3 can be nicely split into two groups, those with, and those without relative momentum dependence in the transverse dressings.

The reason for the effect in more technical terms can also be seen in table 6.3. For transverse terms that are not suppressed in the relative momentum it is beneficial to accumulate integration strength at high relative momenta. As can be seen in the table the average relative momenta $\langle k \rangle$ are quite high for all cases without suppression. The same is true for the quark momentum which is of course coupled to k . In the cases where the k^2 damping is included, that is the DSE dressings with full kinematics or the 'improved' NJL version, the relative momenta are clearly smaller on average. This seems plausible since the integrand is damped in these regions such that no integration strength can be found there. If we wanted

to be quirky we could say that the suppression expected on the grounds of the NJL results is strongly suppressed in more realistic cases. The picture is completed by looking at the average of the leading transverse dressing $\langle T \rangle$ that is tested in the integration. It is always negative but larger in magnitude for the cases without relative momentum dependence. And the magnitude seems always to be explained by exactly that k dependence. That is all results in table 6.3 fall basically in one of two groups. Either with or without k -dependence.

It has to be noted, however, that the average masses $\langle M \rangle$ found in all cases are quite small compared to the mass of $M = 0.3 \text{ GeV}$ used in ENJL model calculations. The relations between the quark masses, momentum regimes, vertex dressings and phase space are thus quite non-trivial.

1BC vertex and transverse structures. Now we analyze the same situation with the transverse structures combined with a 1BC vertex instead of a bare one. The corresponding results are shown in table 6.4. Again the NJL dressing provides significant suppression whereas the leading transverse DSE structure does not. Neglecting the k -suppression in the transverse DSE vertex components is able to reproduce the NJL result also in combination with a 1BC dressing. Introducing the k -suppression in the NJL vertex on the other hand comes close to the DSE case again. The reasoning of the k -suppression does apply once more as in the case of a bare vertex for the 'gauge' part. One important difference is however present for the case of the full transverse vertex structure including the full kinematics (that is no k -suppression). In this case the additional transverse components beyond the γ_μ^T part are important. They give a suppression the 'leading' part cannot manage on its own. The leading part does not reduce the 1BC contribution at all whereas the full transverse vertex seems to do.

Summary of LBL results so far. In the following we summarize our LBL quark loop results obtained so far. We formulated some expectations we had of the influence of the different vertex dressing present in the self-consistent solution of the quark-photon vertex as well as the self consistently dressed quark propagator. Our findings are most easily summarized in bullet points

- Both the NJL model and the DSE/BSE approach have to some extent similar structures. Both have a quark photon vertex that has a part that is dictated by the WTI and a part that is reminiscent of vector-meson dominance. They differ in that mesons-amplitudes and the quark-photon vertex are functions of one kinematic variable in the NJL case whereas the DSE/BSE approach has the full kinematic dependence on three degrees of freedom in the vertices. The vertex has a very simple structure in the NJL model whereas the functional point of view takes into account all structures that are present in full QCD.
- The momentum dependent quark mass is not tested at its infrared plateau $M(0) = 0.477 \text{ GeV}$ but rather in the mid-momentum regime where $M \approx 0.2 \text{ GeV}$.
- This results in an enhancement of the LBL contribution precisely due to the rather small effective mass
- The non-trivial wave function of the quark causes a suppression that together with the dynamical mass cause the dressed quark/bare vertex result to be close to what is expected for bare constituent quarks of $M = 0.3 \text{ GeV}$.
- The suppression due to the wave function can be reasonably explained by taking $Z(p^2) \rightarrow \langle Z \rangle = \text{const.}$
- The 1BC dressing causes enhancement that has roughly the opposite effect than the quark wave function. It can also be approximately explained as an averaged effect. The 1BC vertex dressing and the non-trivial quark wave function Z cancel to quite some extent.
- The transverse parts of the vertex have the tendency reduce the overall result
- This reduction is supposed to be smaller than in the NJL case due to the fact that the DSE/BSE vertex is suppressed for high relative momenta $\rightarrow k$ -suppression.
- The difference of the influence of the transverse vertex parts can be explained by the k -suppression on the quantitative level
- In the end the reasons for our larger LBL contribution to $g - 2$ are twofold:
 - The quark mass function is tested on scales where it is considerably smaller (0.2 GeV) than a naive constituent mass of 0.3 GeV (The vertex dressing from the 1BC part is important but partially cancelled by the wave function)
 - The reduction from VMD-like effects hidden in the transverse vertex structure are smaller than in the NJL case due to suppression of the subtractive contributions at high relative momenta.

The vertex

$$\Gamma_\mu = \gamma_\mu L_1 + \Gamma_\mu^T \quad (6.59)$$

is the closest we can come to the full vertex at the moment. It yields

$$a_\mu^{\text{LBL,1BC+T}, N_f=2} = 64 \times 10^{-11}, \quad (6.60)$$

as quark-loop LBL-contribution to the muon $g-2$ for the two lightest flavours. This is our best estimate for the not yet obtained full result.

Table 6.4: 1BC and leading transverse vertex as well as 1BC and full transverse vertex compared to NJL dressings. Quarks are always fully dynamical. $\lambda^{(1)}$ is the dressing of the γ_μ^T part obtained from the vertex BSE and $\lambda_{\text{NJL}} = -P^2/(P^2 + M_V^2)$. In addition $f(k^2) = 1/(1 + k^4/0.66^4)$. P and k are the total and relative momenta of the vertices, L_1 is the dressing of the bare vertex and T_1 is the leading transverse dressings corresponding to γ_μ^T (either $\lambda^{(1)}$ or λ_{NJL}). P , k and M are given in units of GeV .

	Dressing	$\langle M \rangle$	$\langle P \rangle$	$\langle k \rangle$	$\langle L_1 \rangle$	$\langle T_1 \rangle$	$a_\mu \times 10^{11}$
1	$\gamma_\mu L_1 + \gamma_\mu^T \lambda^{(1)}(k^2 = 0)$	0.08	0.021	7.4	1.19	-0.105	41
2	$\gamma_\mu L_1 + \gamma_\mu^T \lambda^{(1)}$	0.12	0.026	1.67	1.29	-0.046	96
3	$\gamma_\mu L_1 + \Gamma_\mu^T(k^2 = 0)$	0.079	0.021	7.3	1.19	-0.106	45
4	$\gamma_\mu L_1 + \Gamma_\mu^T$	0.13	0.028	1.53	1.32	-0.051	64
5	$\gamma_\mu L_1 + \gamma_\mu^T \lambda_{\text{NJL}}$	0.092	0.021	5.5	1.22	-0.095	43
5	$\gamma_\mu L_1 + \gamma_\mu^T \lambda_{\text{NJL}} \times f(k^2)$	0.11	0.027	1.65	1.3	-0.022	103

7 Discussion

In this chapter we summarize our results for the hadronic vacuum polarisation (HVP, chapter 5) and the light-by-light scattering (LBL, chapter 6) contributions to the anomalous magnetic moment of the muon a_μ . Furthermore we discuss these results and compare them to other approaches.

Hadronic vacuum polarisation. In chapter 5 we presented details about our calculational scheme for HVP as well as the results obtained for this contribution within the rainbow-ladder truncation of QCD. We used a model for the quark-gluon interaction that has been successfully applied to hadronic physics for more than a decade. Besides masses and decay constants for the mesonic states that are most relevant for the problem at hand (e.g. pseudo-scalar mesons and vector mesons) it gives satisfying results for form factors and charge radii. Although not directly related to the present work it is worth noting that also nucleons, including their form factors, are part of the impressive list of the observables that have been calculated (see the overview in table 4.3). The HVP calculation adds another two observables to this list. The Adler function that is a non-trivial observable since it allows for a detailed diagnoses of the interplay of high- and low-energy QCD effects is one of them. The other is the contribution to the muon $g - 2$. Using among others a parameter set that is completely fixed by meson phenomenology (the standard parameter set for this approach) we are able to reproduce the HVP contribution on the less than ten percent level. In that way this result is dynamically linked to many other observables which in our view adds lots of credibility to this result. This deviation is clearly to be expected within this relatively simple truncation of QCD. We believe to have presented plausible arguments that this should be closely related to the fact that the ρ meson in this model, which plays a dominant rôle here, is about four percent too light. In fact fixing our parameters to the physical ρ mass improved our results significantly (5.13). The results for the standard parameter set I and the set II with optimized ρ mass are

$$a_\mu^{HVP,I} = 7440(77) \times 10^{-11} , \quad (7.1)$$

$$a_\mu^{HVP,II} = 6760(74) \times 10^{-11} . \quad (7.2)$$

Light-by-light scattering. Given the fact that the employed truncation worked well for HVP we are confident that light-by-light scattering can be dealt with in a comparable satisfying way. As shown in app. F the definition of the photon four-point function follows

unambiguously from the (truncated) photon two-point function. This derivation rests upon the rainbow-ladder truncation and on the photon field being a non-dynamical background as far as the hadronic two- and four-photon correlators are concerned. As already argued above the usefulness of the first assumption is strengthened by the successful application of the DSE method in the HVP case and many other meson and baryon observables. The second assumption only neglects contributions which are $\mathcal{O}(\alpha_{\text{QED}})$ suppressed. Our prescription for the photon four-point function (6.9) thus rests on the same ground as the hadronic photon self-energy (5.1) shown in fig. 5.1.

Instead of the representation (6.9) that is fully comparable to HVP we use an approximation for the time being. This is the resonance expansion shown in Eq. (6.12), a picture comparable to many calculations done within the framework of effective theories (see tab. 7.1). For the pseudo-scalar meson-exchange contribution we find results that are comparable to these model calculations (6.42). A comparison can be found in table 7.1. For the quark-loop contribution we find potentially strong influence of momentum dependent quark propagators as well as enhancement due to certain vertex dressings. This is explained in great detail in section 6.4. On the one hand we see that the momentum dependent quark mass function is not dominantly tested in the infrared where $M(0) \approx 450 \text{ MeV}$ but rather in the mid-momentum range where $M(p^2) \approx 200 \text{ MeV}$. This leads to an enhancement of the contribution which increases simply for decreasing quark mass. On the other hand the non-trivial wave function leads to a suppression of 50% taking all four quarks into account. Furthermore we have the 'gauge' part of the quark-photon vertex that is dictated by the Ward-Takahashi identity. In this work we considered only the leading one of the three components since the other two are numerically delicate and our results for those are not trustworthy at the moment. This leading part causes an enhancement that basically cancels the suppression caused by the quark wave function. Furthermore we analysed the transverse vertex components that are supposed to yield a suppression on the grounds of results within the NJL model. Indeed we find this suppression, but it is much less dramatic, than in the NJL case. The reason is that mesons are bilocal fields in the DSE/BSE approach and the full momentum dependence of vertices is taken into account. This simply reduces the contributions from kinematic regions where the NJL dressings collect the contributions that make the quark-loop contribution so small. All this is discussed in detail in section 6.4.

In order to obtain the complete LBL result we add the contributions of meson exchange and quark loop

$$\begin{aligned} a_{\mu}^{\text{LBL}} &= a_{\mu}^{\text{quarkloop}} + a_{\mu}^{\text{PS-exchange}} + a_{\mu}^{\pi/\text{K-loop, scalar, axial-vector}} \\ &= 64(30) \times 10^{-11} + 81(12) \times 10^{-11} + 0(20) \times 10^{-11}, \end{aligned} \quad (7.3)$$

where the systematic uncertainty of the quark-loop result is taken to be 50 percent, due to the fact that potentially important contributions have been neglected. The error estimate for

Table 7.1: A comparison of the DSE results for the LBL contributions to the muon anomaly with various other approaches. Details can be found in the text.

Group	Model	$a_\mu^{\text{LBL}} (\pi^0)$	$a_\mu^{\text{LBL}} (\pi^0, \eta \text{ and } \eta')$	$a_\mu^{\text{LBL}} (\text{quark-loop})$	a_μ^{LBL}
BPP [29, 31]	ENJL	59(11)	85(13)	21(3)	83(32)
HKS [33, 34, 35]	HLS	57(4)	83(6)	9.7(11.1)	89(16)
KN [36]	LMD+V	58(10)	83(12)	–	83(12)
MV [37]	LMD+V	77(5)	114(10)	†	114(10)
N [143]	LMD+V	72(12)	99(16)	†	99(16)
PdRV [38]	LMD+V	–	114(10)	†	105(26)
DB [130]	NL χ QM	65(2)	–	–	–
DRZ [131]	NL χ QM	50.1(3.7)	58.5	–	–
GdR [129]	C χ QM	68(3)	–	82(4)	150(5)
This work	DSE	58(7)	81(12)	64(30)	145(62)

the meson-exchange is based on the quality of the meson phenomenology of the truncation used and on the off-shell prescription for the meson amplitudes (6.27). Furthermore we infer the estimate of the contribution of higher mesons from results obtained within the ENJL model. In [31] the pion and kaon loop contribution as well as scalar and axial-vector meson exchange contributions amount in sum to

$$a_\mu^{\pi/\text{K-loop, scalar, axial-vector, NJL}} = -23.3 \times 10^{-11},$$

which we use as a base for our estimate of the contributions we did calculate explicitly so far. All uncertainties within LBL are added linearly. Our final result obtained through the addition of the meson-exchange (6.42) and the quark-loop result (6.60) is

$$a_\mu^{\text{LBL}} = 145(62) \times 10^{-11}. \quad (7.4)$$

We think that our estimate is rather conservative but can be improved once a full calculation along the lines of Eq. (6.9) is performed. Ultimately an uncertainty on the sub ten percent level like in the case of HVP seems reasonable. A comparison to other approaches is given in table 7.1.

The different approaches used are the Extended-NJL model, the Hidden Local Symmetry approach (HLS), the non-local chiral quark model (NL χ QM), the constituent chiral quark model (C χ QM) and various approaches based on vector meson dominance (VMD) together with lowest meson dominance (LMD+V). In general the agreement in the pion or PS-meson exchange contributions is rather good. Some of the VMD models have larger contributions here, which to some extent can be traced back to the fact that off-shell constraints are

imposed on the $\pi - \gamma\gamma$ transition form factor that cause an enhancement [150, 37]. It has been argued [38] that these additional contributions which correspond to high-energy can be found e.g. in the quark-loop contribution in other approaches. The VMD approaches typically restrict the consideration to purely mesonic degrees of freedom such that no quark-loop is present such as in the case of the other approaches. The comparison of the meson exchange contribution is thus to some extent comparing apples with oranges as far as the contribution coming from high-energy regions is concerned. Another interesting observation is the fact that in the NL χ QM [131] the contribution of the η and η' mesons is much reduced. This suppression comes from a consistent treatment of meson off-shell effects. These are much stronger for the η and η' mesons than for the pion. This is due to the fact that the decay width, which defines the normalisation of the corresponding form factor, is defined in the time-like region. Often form factors are used that are defined to reproduce the physical decay width of mesons at the Euclidean origin. This seems to be a reasonable approximation for the π^0 but might fail in the case of η and η' . For the quark loop contribution we see quite some difference of the DSE approach to the HLS and ENJL results. This discrepancy has been discussed already. For the summed up results we see quite some spread. Most approaches give consistently lower numbers than the result we obtained. It has to be noted, however, that there is agreement withing error bars. It is interesting to note that recently obtained result within the C χ QM also give rise to an enhanced LBL contribution, including a rather large quark loop result [129].

Finally we think that the DSE approach holds the promise to yield a description that ultimately makes the usually applied distinction into high- and low-energy regions super fluent. In fact our results indicate that it might even be crucial to have the transition region between these two regimes tightly under control. Our treatment is not yet at the final stage such that no last conclusion can be drawn. We think, however, that our approach can be combined with efforts that are currently undertaken withing lattice calculations. In fact there are good examples where a combination of DSE and lattice methods yield an improved understanding.

A Euclidean conventions

In Euclidean field theory the conventions are far less established than in the Minkowski space formulation and tend to differ a lot from author to author. We thus find it useful to lay out the conventions used in this thesis in every detail. The basic idea of Euclidean quantum field theory is to take the well known Wick rotation a step further and perform it on the level of the generating functional in order to avoid the continuation of every single loop integral. In the end one can come up with solutions of Euclidean Green's functions that are considered to be analytically continued versions of functions at space-like Minkowski momenta. Formally the back-rotation is then possible since the functions are usually decomposable into a sum over known covariants and scalar dressing functions e.g. $S(p) = i\not{p}\sigma_V(p^2) + \sigma_S(p^2)$. The back rotation of the covariants like \not{p} can be worked out while for the functions that contain the dynamics one just has to identify the Euclidean momentum with a space-like Minkowski momentum: $\sigma(p_M^2 < 0) := \sigma(p_E^2)$ with $p_E^2 = -p_M^2$. The question of whether the back rotation is possible is governed by the Osterwalder-Schrader axioms of Euclidean field theory [151]. The conventions are chosen such as to correspond to those of Ref. [24] as closely as possible.

In particular the following analytical continuation is adopted:

- $x^0 \longrightarrow -ix_0^E \quad \vec{x} \longrightarrow \vec{x}^E$
- $\gamma^0 \longrightarrow \gamma_0^E \quad \gamma^i \longrightarrow i\gamma_i^E$
- $\partial_0 \longrightarrow i\partial_0^E \quad \partial_i = \frac{\partial}{\partial x^i} \longrightarrow \frac{\partial}{\partial x_i^E} = \partial_i^E$
- $\not{\partial} = \partial^0\gamma^0 - \partial^i\gamma^i \longrightarrow (i\partial_0^E\gamma_0^E) + \partial_0^E(i\gamma_i^E) =: i\not{\partial}^E$
- $\not{p} = p^0\gamma_0 + p^i\gamma_i = p^0\gamma^0 - p^i\gamma^i \longrightarrow (ip_0^E)\gamma_0^E - (-p_i^E)(i\gamma_i^E) = ip_\mu^E\gamma_\mu^E =: i\not{p}^E$
- $x^\mu p_\mu = x^0p_0 + x^ip_i = x^0p^0 - x^ip^i \longrightarrow (-ix_0^E)(ip_0^E) - x_i^E(-p_i^E) = x_\mu^E p_\mu^E \quad (\text{A-1})$
- $f(x) = \int_k \tilde{f}(k) e^{-ik^\mu x_\mu} \longrightarrow f(x^E) = i \int_{k^E} \tilde{f}(k^E) e^{-ix_\mu^E p_\mu^E},$
- $A_0(x) \longrightarrow iA_0^E(x^E)$
- $A_i(x) \longrightarrow A_i^E(x^E)$
- $F_{\mu\nu}F^{\mu\nu} \longrightarrow F_{\mu\nu}^E F_{\mu\nu}^E$

- $\partial^\mu A_\mu \longrightarrow -\partial_\mu^E A_\mu^E$
- $A^\mu A_\mu \longrightarrow -A_\mu^E A_\mu^E$
- $\not{A} \longrightarrow i\not{A}^E$

where E labels Euclidean quantities. In this way the algebra of gamma-matrices is

$$\{\gamma_\mu, \gamma_\nu\} = 2\delta_{\mu\nu} \quad (\text{A-2})$$

We take the Minkowski space generating functional now to be

$$Z = \int \mathcal{D}\mu \, e^{iS_M}, \quad (\text{A-3})$$

with Lagrangian \mathcal{L}_M

$$\mathcal{L}_M = \bar{\psi}(i\not{D} - m)\psi - \frac{1}{2}\text{Tr}(F_{\mu\nu}F^{\mu\nu}). \quad (\text{A-4})$$

Here $D_\mu = \partial_\mu - igA_\mu$, $A_\mu = A_\mu^a t^a$, $F_{\mu\nu} = F_{\mu\nu}^a t^a$, $F_{\mu\nu} = \partial_\mu A_\nu - \partial_\nu A_\mu - ig[A_\mu, A_\nu]$. So we have

$$F_{\mu\nu}^a = \partial_\mu A_\nu^a - \partial_\nu A_\mu^a + gf^{abc}A_\mu^b A_\nu^c \quad (\text{A-5})$$

written explicitly the Lagrangian is

$$\mathcal{L}_M = \bar{\psi}(i\not{\partial} - m)\psi + \frac{1}{2}A_\mu[g^{\mu\nu}\partial^2 - \partial^\mu\partial^\nu]A_\nu + g\bar{\psi}\not{A}\psi \quad (\text{A-6})$$

$$-gf^{abc}(\partial^\mu A^{\mu,a})A_\mu^b A_\nu^c - \frac{g^2}{4}f^{abc}f^{ade}A_\mu^a A_\nu^b A_\mu^d A_\nu^e. \quad (\text{A-7})$$

We now apply the rules shown in Eq. (A-1) to the action corresponding to Eqs. (A-7,A-4) to obtain $iS_M \rightarrow -S_E$:

$$\begin{aligned} S_E = \int_x \left\{ \bar{\psi}(\not{\partial} + m)\psi + \frac{1}{2}A_\mu[-\partial^2\delta_{\mu\nu} + \partial^\mu\partial^\nu]A_\nu - ig\bar{\psi}\not{A}\psi \right. \\ \left. + gf^{abc}(\partial_\mu A_\nu^a)A_\mu^b A_\nu^c + \frac{g^2}{4}f^{abc}f^{ade}A_\mu^a A_\nu^b A_\mu^d A_\nu^e \right\} \end{aligned} \quad (\text{A-8})$$

Applying in addition the standard Feddeev-Popov gauge fixing procedure for covariant gauges [24] we get

$$\begin{aligned} S_E = \int_x \left\{ \bar{\psi}(\not{\partial} + m)\psi + \frac{1}{2}A_\mu[-\partial^2\delta_{\mu\nu} + (1 - \frac{1}{\xi})\partial^\mu\partial^\nu]A_\nu + \bar{c}\partial^2 c - ig\bar{\psi}\not{A}\psi \right. \\ \left. + gf^{abc}\bar{c}^a\partial_\mu(A_\mu^c c^b) + gf^{abc}(\partial_\mu A_\nu^a)A_\mu^b A_\nu^c + \frac{g^2}{4}f^{abc}f^{ade}A_\mu^a A_\nu^b A_\mu^d A_\nu^e \right\}. \end{aligned} \quad (\text{A-9})$$

From this we obtain the quark and gluon propagators as

$$\begin{aligned} D_{\mu\nu}^{-1}(x, y) &= \frac{\delta^2 \mathcal{S}_E}{\delta A_\nu(x) \delta A_\mu(y)} \Big|_{g=0} = [-\partial^2 \delta_{\mu\nu} + (1 - \frac{1}{\xi}) \partial_\mu \partial_\nu] \delta(x - y) \\ &= \int_k [k^2 \delta_{\mu\nu} - (1 - \frac{1}{\xi}) k_\mu k_\nu] e^{-ik \cdot (x-y)}, \end{aligned}$$

so that

$$D_{\mu\nu}^{-1}(k) := [k^2 \delta_{\mu\nu} - (1 - \frac{1}{\xi}) k_\mu k_\nu] = k^2 T_{\mu\nu} + \frac{1}{\xi} k_\mu k_\nu, \quad (\text{A-10})$$

and

$$\begin{aligned} S^{-1}(x, y) &= \frac{\delta^2 \mathcal{S}_E}{\delta \psi_y \delta \bar{\psi}_x} \Big|_{g=0} = (\not{\partial}_x + m) \delta(x - y) \\ &= \int_p (-i\not{p} + m) e^{-ip \cdot (x-y)}, \end{aligned}$$

which yields

$$S^{-1}(p) = -i\not{p} + m. \quad (\text{A-11})$$

The propagators itself then read

$$\begin{aligned} D_{\mu\nu}(k) &= \left[\delta_{\mu\nu} - \frac{k_\mu k_\nu}{k^2} \right] \frac{1}{k^2} + \xi \frac{k_\mu k_\nu}{k^4} \\ S(p) &= \frac{i\not{p} + m}{p^2 + m^2}. \end{aligned} \quad (\text{A-12})$$

Renormalization The renormalized form of the Lagrangian is

$$\begin{aligned} \mathcal{L} &= Z_\psi \bar{\psi} (\not{\partial} + Z_m m) \psi + \frac{Z_A}{2} A_\mu [-\partial^2 \delta_{\mu\nu} + (1 - \frac{1}{\xi}) \partial^\mu \partial^\nu] A_\nu + Z_c \bar{c} \partial^2 c \\ &\quad - i g Z_{\psi A} \bar{\psi} \not{A} \psi + g Z_{cA} f^{abc} \bar{c}^a \partial_\mu (A_\mu^c c^b) \\ &\quad + g Z_{3A} f^{abc} (\partial_\mu A_\nu^a) A_\mu^b A_\nu^c + \frac{g^2}{4} Z_{4A} f^{abc} f^{ade} A_\mu^b A_\nu^c A_\mu^d A_\nu^e. \end{aligned} \quad (\text{A-13})$$

B Derivation of the photon DSE

In order to give a specific example of how to use the generating functional of Dyson-Schwinger equations (3.15) we derive the photon DSE explicitly in this appendix. We write the action of QCD and QED in the form

$$S = Z_\psi \int_{xy} \bar{\psi}_x S_0^{-1}(x, y) \psi_y + ie Z_{\psi A}^{\text{QED}} \int_x \bar{\psi}_x A_x \psi_x + \frac{Z_A^{\text{QED}}}{2} \int_{xy} A_{\mu, x} [D_0^{-1}(x, y)]_{\mu\nu} A_{\mu, y} + \tilde{S}_{\text{QCD}}[\bar{\psi}, \psi], \quad (\text{B-1})$$

where the term \tilde{S}_{QCD} is just the QCD action (A-13) excluding the kinetic energy of the quarks. The dependence on the gluon and ghost fields is not shown explicitly. They are assumed to be present implicitly in e.g. the quark propagator. But on the formal level they do not concern us in this appendix. In addition we neglected the source terms in Eq. (B-1) to be more compact but we will assume them to be present.

In order to proceed we need

$$\frac{\delta S}{\delta A_{\mu, x}} = ie Z_{\psi A}^{\text{QED}} \bar{\psi}_x \gamma_\mu \psi_x + \int_y [D_0^{-1}(x, y)]_{\mu\nu} A_{\mu, y}. \quad (\text{B-2})$$

In order to get the corresponding derivative of the effective action Γ we have to make the replacement $\psi \rightarrow \psi + (\Gamma'')^{-1} \delta/\delta\psi$. Here again ϕ is a placeholder for any field. The only realization that will contribute in our case is

$$\bar{\psi}_x \rightarrow \bar{\psi}_x + \int_u S(x, u) \frac{\delta}{\delta \psi_u}, \quad (\text{B-3})$$

where S is the full quark propagator e.g.

$$S(x, y) = \left(\frac{\delta^2 \Gamma}{\delta \bar{\psi}_y \delta \psi_x} \right)^{-1}.$$

This is actually the expression where the dynamical content of QCD enters implicitly since the full quark propagator does involve the gluon fields. In the spirit of the generating functional for DSE's (3.15) we use (B-3) in (B-2) to obtain

$$\frac{\delta \Gamma}{\delta A_{\mu, x}} = ie Z_{\psi A}^{\text{QED}} \bar{\psi}_x \gamma_\mu \psi_x + ie Z_{\psi A}^{\text{QED}} \text{Tr}[S(x, x) \gamma_\mu] + Z_A^{\text{QED}} \int_y [D_0^{-1}(x, y)]_{\mu\nu} A_{\mu, y}. \quad (\text{B-4})$$

Taking an additional derivative with respect to the photon field we get

$$D_{\mu\nu}^{-1}(x, y) := \frac{\delta^2 \Gamma}{\delta A_{\nu, y} \delta A_{\mu, x}} = Z_A^{\text{QED}} [D_0^{-1}(x, y)]_{\mu\nu} - ie Z_{\psi A}^{\text{QED}} \int_{u, w} \text{Tr}[S(x, u) (-ie \Gamma_\nu(u, y, w)) S(w, x) \gamma_\mu], \quad (\text{B-5})$$

which is already the photon DSE in coordinate space. We used the relation

$$\delta M^{-1} = -M^{-1}(\delta M)M^{-1},$$

as well as

$$\frac{\delta \Gamma}{\delta \bar{\psi}_u \delta A_{\nu, y} \delta \psi_w} = -ie \Gamma_\nu(u, y, w). \quad (\text{B-6})$$

The propagators are straightforwardly transformed into momentum space. For the self energy we have

$$\begin{aligned} \Pi_{\mu\nu}(x, 0) &= -e^2 Z_1 \int_{uw} \text{Tr}[S_{xu} \Gamma_\mu(u, 0, w) S_{wx} \gamma_\nu] \\ &= -e^2 \int_{uw} \int_{p, q, k_1, k_2} \text{Tr}[S_p e^{-ip \cdot (x-u)} \Gamma_\mu(k_1, k_2) e^{-ik_1 \cdot u} e^{-ik_2 \cdot w} S_q e^{-iq \cdot (v-x)} \gamma_\nu] \\ &= -e^2 \int_{uw} \int_{p, q, k_1, k_2} e^{-ix \cdot p} e^{-iu \cdot (-p-k_1)} e^{-iw \cdot (q+k_2)} \text{Tr}[S_p \Gamma_\mu(k_1, k_2) S_q \gamma_\nu] \\ &= -e^2 \int_{p, q} e^{-ix \cdot (p-q)} \text{Tr}[S_p \Gamma_\mu(p, q) S_q \gamma_\nu] \\ &\stackrel{p \rightarrow p+q}{=} \int_p e^{-ip \cdot x} \underbrace{\left\{ -e^2 Z_1 \int_q \text{Tr}[S_{(p+q)} \Gamma_\mu(p+q, q) S_q \gamma_\nu] \right\}}_{\Pi_{\mu\nu}(p)}, \end{aligned} \quad (\text{B-7})$$

such that the self energy in momentum space is defined and the DSE in momentum space reads

$$D_{\mu\nu}^{-1}(p) = Z_A^{\text{QED}} (p^2 T_{\mu\nu} + \frac{1}{\xi} p_\mu p_\nu) + Z_{\psi A}^{\text{QED}} \Pi_{\mu\nu}(p). \quad (\text{B-8})$$

This DSE looks formally the same for pure QED. The effects of QCD are hidden in the precise form of the quark propagator S and the quark photon vertex Γ_μ (B-6). Their DSE's include the effects of QCD explicitly (3.20,3.48). The truncated DSE's used in the present approach are (4.14, 4.19).

C Derivation of Ward-Takahashi identities

In this appendix we derive the WTI shown in Eq. (3.52). We consider the global $U_A(3) \simeq U_A(1) \times SU_A(3)$ transformations which are generated in the fundamental representation by the eight Gell-Mann matrices λ^a and the three dimensional unit matrix. That is the Lie algebra given through

$$[T^a, T^b] = i f^{abc} T^c \quad a, b, c = 1, \dots, 8 \quad (\text{C-1})$$

$$T^a T^b = \frac{1}{6} \delta_{ab} + \frac{1}{2} (i f^{abc} + d^{abc}) T^c \quad \text{Tr}(T^a T^b) = \frac{1}{2} \quad (\text{C-2})$$

$$(T^a)^\dagger = T^a \quad \text{Tr} T^a = 0, \quad (\text{C-3})$$

where f^{abc} are the totally skew symmetric structure constants and the d^{abc} are symmetric in the indices. The generators are $T^a = \lambda^a/2$. In addition we call the generator of the of the $U_A(1)$ symmetry T^0 .

The transformations in the fundamental representation are now generated by the elements g of $U_A(3)$

$$g(\theta) = e^{i\theta^a T^a \gamma_\mu}, \quad (\text{C-4})$$

where θ^0 parametrize the element g and the Dirac matrix γ_μ (3.51) ensures that left-handed and right-handed spinors are transformed with opposite angles

$$\psi \rightarrow e^{i\theta^a T^a \gamma_5} \psi \quad \bar{\psi} \rightarrow \bar{\psi} e^{i\theta^a T^a \gamma_5} \quad (\text{C-5})$$

$$\psi_L \rightarrow e^{i\theta T^a} \psi_L \quad \psi_R \rightarrow e^{-i\theta T^a} \psi_R \quad (\text{C-6})$$

$$\psi_{R/L} = \frac{1 \pm \gamma_5}{2} \psi \quad \bar{\psi}_{L/R} = \bar{\psi} \frac{1 \mp \gamma_5}{2}. \quad (\text{C-7})$$

In order to derive WTI's we start with the observation that the path integral is invariant under the transformation $\psi \rightarrow \psi'$

$$\int \mathcal{D}\bar{\psi} \psi e^{-S} = \int \mathcal{D}\psi' \bar{\psi}' \mathcal{J} e^{-S'}, \quad (\text{C-8})$$

where \mathcal{J} is the Jacobian of the transformation. This must be the case since $U(N)$ acts as an automorphism on the space of the quark spinors such that the integration variables are

just labeled in a different way in (C-8). Now we explicitly carry out the infinitesimal version of (C-7) $\delta\psi = i\theta^a(z)T^a\gamma_5\psi$ using a space time dependent $\theta^a(z)$ for the moment. It can be shown that the Jacobian \mathcal{J} evaluates to [24]

$$\mathcal{J} = \exp \left[i \int_z \theta^a(z) \frac{e^2}{16\pi^2} \text{Tr}[T^a Q^2] \epsilon_{\mu\nu\alpha\beta} F_{\mu\nu} F_{\alpha\beta} + i \int_z \theta^a(z) \frac{g^2}{16\pi^2} \text{Tr}[T^a t^i t^j] \epsilon_{\mu\nu\alpha\beta} F_{\mu\nu}^i F_{\alpha\beta}^j \right], \quad (\text{C-9})$$

where the Abelian photon field is represented by $F_{\mu\nu}$ and $F_{\mu\nu}^i$ is the non-Abelian gluon field tensor. The matrices t^i are the generators of the $SU(3)$ gauge group of QCD, $Q = \text{diag}(2/3, -1/3, -1/3)$ is the charge matrix of the quarks ¹ and e and g are the electromagnetic and strong couplings. The traces are defined in flavour and colour space. These do contribute only to selective channels a . The anomaly term involving the gluons does only contribute if $a = 0$ since for all other channels $\text{Tr}[T^a] = 0$. This term plays a rôle in the $U_A(1)$ problem that concerns the properties of the η' meson [82, 83, 84]. The other term evaluates to non-zero exactly for the diagonal flavour generators $a = 0, 3, 8$. This concerns the π^0 , η and η' mesons and is linked to their decay into photons [80, 87]. These origin of these traces is easily understandable if one thinks of the one-loop triangle diagrams which correspond to matrix elements of these operators. Attaching the bi-local quark currents that function as interpolating operators for the corresponding mesons fields as well as the currents coupling to the gauge fields to the quark triangle, the matrices inside the traces in (C-9) just come automatically from the definition of these currents, or alternatively from the structure of the corresponding vertices which is the same.

Now we have to care about the remaining change of the action S' in Eq. (C-8) under the infinitesimal local variation, which evaluates to

$$\delta S = -i \int_z \theta^a(z) \partial_\mu (\bar{\psi} \gamma_\mu \gamma_5 T^a \psi) + i \int_z \theta^a(z) \bar{\psi} \gamma_5 \{M, T^a\} \psi, \quad (\text{C-10})$$

where M is the quark mass matrix. Taking the infinitesimal version of (C-8), that is $|\theta|$ small we get

$$0 = \langle -\delta S + \log \mathcal{J} \rangle.$$

In addition we approach the limit of a global symmetry transformation again ($\theta^a = \text{const.}$)

$$\langle \partial_\mu j_{\mu,5}^a \rangle_z = -\langle j_5^a \rangle_z + \frac{e^2}{16\pi^2} \text{Tr}[T^a Q^2] \epsilon_{\mu\nu\alpha\beta} \langle F_{\mu\nu} F_{\alpha\beta} \rangle_z + \frac{g^2}{16\pi^2} \text{Tr}[T^a t^i t^j] \epsilon_{\mu\nu\alpha\beta} \langle F_{\mu\nu}^i F_{\alpha\beta}^j \rangle_z, \quad (\text{C-11})$$

¹Here we only take the three light quarks

with

$$\begin{aligned} j_{\mu,5,z}^a &= \bar{\psi}_z \gamma_\mu \gamma_5 T^a \psi_z \\ j_{5,z}^a &= \bar{\psi}_z \gamma_5 \{M, T^a\} \psi_z. \end{aligned} \quad (\text{C-12})$$

Next we insert an operator \mathcal{O} into Eq. (C-8) and carry out the infinitesimal variation as before

$$0 = \langle \delta \mathcal{O} \rangle + \langle -\mathcal{O} \delta S \rangle + \langle \mathcal{O} \log \mathcal{J} \rangle. \quad (\text{C-13})$$

If we take $\mathcal{O} = \psi_x \bar{\psi}_y$ we get

$$\frac{\delta \mathcal{O}}{\delta \theta_z^a} = i \gamma_5 T^a \delta_{zx} \psi_x \bar{\psi}_y + i \psi_x \bar{\psi}_y \delta_{yz} \gamma_5 T^a, \quad (\text{C-14})$$

while the remaining terms of Eq. (C-13) are just obtained by the insertion of this operator into (C-11)

$$\begin{aligned} \langle \partial_\mu j_{\mu,5,z}^a \psi_x \bar{\psi}_y \rangle &= \gamma_5 T^a \delta_{zx} \langle \psi_x \bar{\psi}_y \rangle + \langle \psi_x \bar{\psi}_y \rangle \delta_{yz} \gamma_5 T^a - \langle j_5^a \psi \bar{\psi} \rangle \\ &+ \frac{e^2}{16\pi^2} \text{Tr}[T^a Q^2] \epsilon_{\mu\nu\alpha\beta} \langle (F_{\mu\nu} F_{\mu\nu})_z \psi_x \bar{\psi}_y \rangle \\ &+ \frac{g^2}{16\pi^2} \text{Tr}[T^a t^i t^j] \epsilon_{\mu\nu\alpha\beta} \langle (F_{\mu\nu}^i F_{\mu\nu}^j)_z \psi_x \bar{\psi}_y \rangle, \end{aligned} \quad (\text{C-15})$$

where $\psi = \psi_x$, $\bar{\psi} = \bar{\psi}_y$ and the currents and anomalous operators are evaluated at a different point z . Next we note that $\langle \psi \bar{\psi} \rangle$ is the full quark propagator and that all three point functions that are involved in Eq. (C-15) have external leg dressing on their quark legs as shown in (3.53,3.54,3.55). We contract by appropriate inverse quark propagators S^{-1} two times exactly such that all external quark legs become amputated and Fourier transform to momentum space in order to arrive at Eq. (3.52). The derivation of the vector WTI (3.56) proceeds very similar. There instead of the $U_A(N_f)$, a $U(1)$ symmetry is used and since it is a gauge symmetry the current is truly conserved.

D Dispersion relations

The method of dispersion relations is an analytic tool that allows for example the determinations of certain correlation functions in the Euclidean region from experimental input that is obtained (of course) for time-like momenta. Unitarity of the S-Matrix entails the optical theorem which relates the imaginary part of a correlation function to a matrix element of a physical process. An object that is not a well-defined observable in the sense of quantum mechanics thus becomes directly measurable. For the case of the hadronic photon vacuum polarisation the optical theorem states

$$\text{Im}\Pi(p^2) \sim \sigma(\gamma^* \rightarrow \text{hadrons})(p^2), \quad (\text{D-1})$$

where σ is the total cross-section of an electron- positron pair annihilation into hadrons and p^2 is a time-like momentum. Since this cross section is measurable, $\text{Im}\Pi$ can be obtained in the time-like region.

Causality on the other hand implies that the momentum-space representation the hadronic photon two-point correlation- function $\Pi(p^2)$ is analytic in the complex p^2 -plane up to a line segment on the positive real axis extending from $4m_\pi^2$ to ∞ . Thus the Cauchy integral formula

$$\Pi(p^2) = \frac{1}{2\pi i} \int_c \frac{d\xi \Pi(\xi)}{p^2 - \xi}, \quad (\text{D-2})$$

for a closed contour c can be applied. Deforming c to a large circle that avoids the non-analytic region following the real axis for $\xi > 4m_\pi^2$ closely, only the integration along the non-analyticity contributes

$$\Pi(p^2) = \frac{1}{\pi} \int_{4m_\pi^2}^{\infty} \frac{d\xi \text{Im}\Pi(\xi)}{p^2 - \xi}. \quad (\text{D-3})$$

In addition

$$\Pi(\xi + i\epsilon) - \Pi(\xi - i\epsilon) = 2i \text{Im}\Pi(\xi),$$

for $\xi \in \mathbb{R}^+$, has been used. Furthermore the subtracted dispersion relation reads

$$\Pi_R(p^2) = \Pi(p^2) - \Pi(0) = \frac{p^2}{\pi} \int_{4m_\pi^2}^{\infty} \frac{d\xi \text{Im}\Pi(\xi)}{\xi(p^2 - \xi)}. \quad (\text{D-4})$$

Now the optical theorem in the version of Eq. (D-1) is used to define $\text{Im}\Pi$ in terms of measurable quantities. The exact identification of these quantities is subtle since the process $e^+e^- \rightarrow \gamma^* \rightarrow \text{hadrons}$ is the experimentally available one and the cross section for $\gamma^* \rightarrow \text{hadrons}$ has to be deduced. This is elaborated for in example in [1]. The result is

$$\Pi_R(p^2) = \frac{\alpha p^2}{3\pi} \int_{4m_\pi^2}^{\infty} d\xi \frac{R_{\text{had}}(\xi)}{\xi(\xi - p^2)}, \quad (\text{D-5})$$

where

$$R_{\text{had}}(\xi) = \frac{\sigma(e^+e^- \rightarrow \text{hadrons})}{\frac{4\pi\alpha(\xi)}{3\xi}}.$$

E Quark-photon vertex

The quark photon can be defined as the connected part of the matrix element

$$\int_{u,w} S(x,u) i e \Gamma_\mu(u,w,z) S(w,y) = \langle (\bar{\psi} \gamma_\mu \psi)_z \psi_x \bar{\psi}_y \rangle \quad (\text{E-1})$$

The basis for the quark-photon vertex $\Gamma_\mu(P, k)$ consists of twelve independent basis elements

$$\Gamma_\mu(P, k) = \sum_i^{12} \lambda^i(P^2, k^2, P \cdot k) V_\mu^i \quad (\text{E-2})$$

. These are generated by

$$\{\gamma_\mu, P_\mu, k_\mu\} \otimes \{\mathbb{1}, \not{P}, \not{k}, [\not{P}, \not{k}]\}. \quad (\text{E-3})$$

In particular we use

$$\begin{aligned} V_\mu^1 &= \gamma_\mu \\ V_\mu^2 &= 2k_\mu \not{k} \\ V_\mu^3 &= 2i k_\mu \\ V_\mu^4 &= i[\gamma_\mu, \gamma_\nu] k_\nu \\ V_\mu^5 &= \gamma_\mu^T \\ V_\mu^6 &= [k_\mu^T \not{k}^T - \frac{1}{3} \gamma_\mu^T (k^T)^2] / k^2 \\ V_\mu^7 &= k_\mu^T \not{P} P \cdot k / (k^2 P^2) \\ V_\mu^8 &= -(\gamma_\mu^T [\not{P}, \not{k}^T] + 2k_\mu^T \not{P}) / 2k \\ V_\mu^9 &= i k_\mu^T / q \\ V_\mu^{10} &= i[\gamma_\mu^T, \not{k}^T] P \cdot k / k^2 \\ V_\mu^{11} &= i[\gamma_\mu^T, \not{P}] \left(1 - \frac{(P \cdot k)^2}{P^2 k^2} \right) - 2V_\mu^{12} \\ V_\mu^{12} &= i k_\mu^T \not{k}^T \not{P} / k^2 \end{aligned} \quad (\text{E-4})$$

as basis.

In order to be able to project any contribution to the vertex onto the basis elements we have to construct the corresponding projectors. Considering the V_μ as linearly independent elements spanning a vector space, the projectors P_μ are just the dual basis

$$\delta_j^i = \langle P^{(i)}, V_{(j)} \rangle = \text{Tr}[P_\mu^{(i)} V_{(j)\mu}]. \quad (\text{E-5})$$

Here $\langle \cdot, \cdot \rangle$ is the scalar product that is defined as contraction of Lorentz indices and trace in Dirac space. The metric tensor M of this space is then

$$M_{ij} = \langle V_{(i)}, V_{(j)} \rangle, \quad (\text{E-6})$$

which can be used to construct the projectors via its inverse $M^{ij} = [M^{-1}]_{ij}$

$$P^{(i)} = M^{ij} V_{(j)}. \quad (\text{E-7})$$

The projectors constructed via (E-7) do obey relation (E-5).

In the course of the numerical solution of Eq. (4.19) we use direct numerical iteration. We use the bare vertex as an initial guess and then perform the numerical integration procedure defined by the right hand side of the equation and add the bare vertex. This gives the result corresponding to the next iteration step. Symbolically we have

$$\Gamma_\mu^{(i)} = \gamma_\mu + \Gamma_\mu^{(i-1)} SSK, \quad (\text{E-8})$$

where the index i counts the iteration step. The symbols denote the quark propagator S and the interaction kernel K . In order to perform the calculation efficiently the numerical integration is cast into a matrix multiplication. This is straight forward with a standard Gaussian quadrature. The vertex is then written as one dimensional array

$$\text{Tr}[P_\mu^{(i)} \Gamma_\mu^P(k^2, k \cdot P)] = \Gamma_{\{k^2, k \cdot P, i\}}, \quad (\text{E-9})$$

that is labelled via the super index $\{k^2, k \cdot P, i\}$. It depends on the relative momentum k^2 , the angle $k \cdot P$ and the index labelling the basis component i . The total momentum P can be kept fixed and is considered to be an external parameter for the time being. The kernel SSK can be cast into a similar form. Starting from the vertex-BSE (4.19) we project onto component $\lambda_{(i)}$ via the projector $P^{(i)}$ just constructed

$$\lambda_{(i)}(k^2, k \cdot P) = \langle P^{(i)}, \gamma_\mu \rangle + \int_q \langle P^{(i)}, \gamma_\alpha S_+ \sum_j \lambda_j V_{(j)\mu} S_- \gamma_\beta \rangle D_{\alpha\beta}, \quad (\text{E-10})$$

where the momentum dependence of most parts is not shown explicitly. The effective interaction including all prefactors is just called $D_{\alpha\beta}$. The matrix kernel K is then defined

as

$$K_{\{q^2, q \cdot P, j\}, \{k^2, k \cdot P, i\}} = \int_{k \cdot q} \langle P^{(i)}(k, P), \gamma_\alpha S(k_+) V_{(j)}(q, P) S(k_-) \gamma_\beta \rangle D_{\alpha\beta}(q - k) w_{q^2} w_{q \cdot P}. \quad (\text{E-11})$$

Here we show explicitly the momentum dependence of all parts including the basis elements $V_{(j)}$ and the projectors $P^{(i)}$. All momenta are now taken on a fixed grid defined by the Gaussian quadrature rule and the kinematic dependence is organized into a super index together with the label i of the basis element. The q integration is trivial in one angle. The angle $q \cdot k$ can also be integrated beforehand since it enters only in the effective interaction $D_{\alpha\beta}(k - q)$ which is known in this approach. The remaining two integration variables q^2 and $q \cdot P$ are now open indices in (E-11) and can be performed by matrix multiplication (see below). The w 's are the weights of the quadrature rule used. The vertex BSE can now be written as

$$\lambda_I = \delta_{i1} + \lambda_J K_{JI}, \quad (\text{E-12})$$

where the inhomogeneous part arises from $\langle P_\mu^{(i)}, \gamma_\mu \rangle = \delta_{i1}$ and the super indices are labelled as $I = \{k^2, k \cdot P, i\}$ and $J = \{q^2, q \cdot P, j\}$. The kinematics that have been chosen are

$$\vec{P} = \begin{pmatrix} 0 \\ 0 \\ 0 \\ P \end{pmatrix} \quad \vec{k} = k \begin{pmatrix} 0 \\ 0 \\ \sin \alpha \\ \cos \alpha \end{pmatrix} \quad \vec{q} = q \begin{pmatrix} \sin \psi \sin \theta \cos \phi \\ \sin \psi \sin \theta \sin \phi \\ \sin \psi \cos \theta \\ \cos \psi \end{pmatrix}, \quad (\text{E-13})$$

where ϕ is the trivial angle, θ is the one that only appears in $q \cdot k$ and can be integrated before iteration in (E-11), $\alpha \rightarrow k \cdot P$ and $\psi \rightarrow q \cdot P$. Equation (E-12) can now be solved efficiently via iteration with the bare vertex as initial guess $\lambda_I^{(0)} = \delta_{i1}$.

F Photon four-point function

In the present chapter we present the derivation of the photon four-point function that is needed in the light-by-light scattering contribution to the muon $g-2$. The four-point function is obtained by taking two derivatives of the full inverse photon propagator

$$\begin{aligned}\Pi_{\mu\nu\alpha\beta} &= \frac{\delta^4 \Gamma[A]}{\delta A_\mu \delta A_\nu \delta A_\alpha \delta A_\beta} \\ &= \frac{\delta^2}{\delta A_\mu \delta A_\nu} \frac{\delta^2 \Gamma[A]}{\delta A_\alpha \delta A_\beta} = \frac{\delta^2}{\delta A_\mu \delta A_\nu} (D_{\alpha\beta})^{-1}.\end{aligned}\tag{F-1}$$

In order to proceed we consider again the photon DSE (3.28) that is presented again in fig. F.1 for the convenience of the reader. We now take two further derivatives of the photon DSE. By the virtue of the approximation we consider, namely rainbow-ladder truncation of QCD, the photon is not a dynamical field in our formalism. The photon self-energy that we calculate is performed using quark and quark-photon vertex equations that do not take into account the photon as a dynamical object, but rather as an external background field. Internally all objects just include dynamical quarks and model-gluons. This is why the application of further derivatives on the photon DSE is consistent within our approximation. Furthermore this operation leaves the internal consistency of the truncation intact. In particular the consistency with chiral symmetry and electro-magnetic current-conservation in form of WTI's is not destroyed.

An object that will be needed on several occasions is the quark anti-quark photon-photon vertex. Within rainbow-ladder approximation this object can be exactly written in terms of

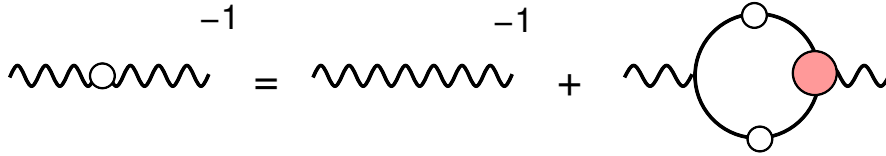


Figure F.1: The photon DSE defined in Eq. (3.30). Full Propagators are denoted by white blobs and the red blob marks the full 1PI fermion-photon vertex.

quark-photon vertices and the T-matrix

$$\text{quark-photon vertex} = 2 \text{ [T-matrix diagram]} \quad (\text{F-2})$$

where the factor of two is not a symmetry factor but rather a convenient way to denote that the two possible photon permutations are included. Application of one derivative to the photon DSE in fig. F.1 gives

$$\text{photon DSE} = \text{quark loop} + 2 \text{ [crossed quark loop]}$$

The bare inverse photon does not contribute. The derivative has to be applied to the quark-photon vertex and the two dressed quarks of the photon self energy. Since there are two quarks in the loop the second diagram comes again with two permutations that correspond to one diagram with straight photon legs and one with crossed ones. This is signaled by the factor 2. Now the application of the relation shown in Eq. (F-2) results in

$$\text{photon DSE} = 2 \text{ [T-matrix diagram]} + 2 \text{ [crossed quark loop]}$$

Next we take into account the relation between the T-matrix and the G-matrix shown graphically in fig. 3.3. The inhomogeneous part that involves just two propagators cancels the second diagram on the right side of the last equation above and we are left with

$$\text{photon DSE} = 2 \text{ [G-matrix diagram]}$$

Now the final step is to remember that the bare quark-photon vertex together with the G-matrix corresponds to a dressed quark-photon vertex and to external quark-leg dressings. Finally we obtain the consistent representation of the hadronic part of the three-photon vertex

$$\text{three-photon vertex} = 2 \text{ [dressed quark loop]}$$

which is not zero as long as the external photon background-field is present. The factor 2 can also be interpreted as representing the two possible orientations of the quark loop.

Now the four-point function is obtained by taking a further derivative with respect to the external photon field. Again the derivative can act on quark-photon vertices and the quark propagators. The result is

$$\text{Diagram} = 6 \times \text{Diagram 1} + 6 \times \text{Diagram 2},$$

where the additional factor three is caused by the three possible vertices and three propagators respectively. Using again relation (F-2) we arrive at

$$\text{Diagram} = 6 \times \text{Diagram 1} + 12 \times \text{Diagram 2} \times T,$$

Up to this point no approximations on top of rainbow-ladder truncation of QCD have been made. The last two representations of the four-point function are thus truly consistent with the rainbow-ladder photon self-energy shown in fig. F.1.

Now we approximate the T-matrix by its pole-structure. This approximation is exact on the respective meson mass-shell. If the poles of the lightest mesons are dominant features of the function even in the low-momentum Euclidean domain, this approximation is also reasonable there

$$\text{Diagram} = 6 \times \text{Diagram 1} + 12 \times \text{Diagram 2} \times \text{Diagram 3},$$

Taking now the two quark triangles as $\pi\gamma\gamma$ form factors we arrive at

$$\text{Diagram} = 6 \times \text{Diagram 1} + 3 \times \text{Diagram 2} \times \text{Diagram 3}, \quad (\text{F-3})$$

where the form factor definition is

$$\text{Diagram 3} = 2 \times \text{Diagram 4},$$

The two permutations that are included in each form factor reduce the permutations of meson insertion in the photon four-point function to three. These are the three meson permutations that are usually considered in this kind of approximation. The representation (F-3) is well known from effective field theory approaches.

Bibliography

- [1] F. Jegerlehner, *The anomalous magnetic moment of the muon*. Springer, 2008.
- [2] F. Jegerlehner and A. Nyffeler *Phys.Rept.* **477** (2009) 1–110, arXiv:0902.3360 [hep-ph]. 134 pages, 68 figures.
- [3] F. Farley and Y. Semertzidis *Prog.Part.Nucl.Phys.* **52** (2004) 1–83.
- [4] S. Schweber, *QED and the men who made it: Dyson, Feynman, Schwinger, and Tomonaga*. Princeton University Press, 1994.
- [5] S. Goudschmidt and G. Uhlenbeck *Nature* **117** (1926) 264–265.
- [6] P. A. Dirac *Proc.Roy.Soc.Lond.* **A117** (1928) 610–624.
- [7] P. Dirac *Proc.Roy.Soc.Lond.* **A118** (1928) 351.
- [8] P. Kusch and H. M. Foley *Phys. Rev.* **72** (Dec, 1947) 1256–1257.
<http://link.aps.org/doi/10.1103/PhysRev.72.1256.2>.
- [9] J. Schwinger *Phys. Rev.* **73** (Feb, 1948) 416–417.
<http://link.aps.org/doi/10.1103/PhysRev.73.416>.
- [10] T. Aoyama, M. Hayakawa, T. Kinoshita, and M. Nio arXiv:1205.5368 [hep-ph].
- [11] D. Hanneke, S. Fogwell, and G. Gabrielse *Phys.Rev.Lett.* **100** (2008) 120801, arXiv:0801.1134 [physics.atom-ph].
- [12] T. Lee and C.-N. Yang *Phys.Rev.* **104** (1956) 254–258.
- [13] *E989 experiment at fermilab*: <http://gm2.fnal.gov/>.
- [14] X. Feng, K. Jansen, M. Petschlies, and D. B. Renner *Phys.Rev.Lett.* **107** (2011) 081802, arXiv:1103.4818 [hep-lat]. added paragraph on chiral extrapolation and additional references, other minor changes, version accepted by PRL.
- [15] P. Boyle, L. Del Debbio, E. Kerrane, and J. Zanotti arXiv:1107.1497 [hep-lat]. * Temporary entry *.

- [16] M. Della Morte, B. Jager, A. Juttner, and H. Wittig *JHEP* **1203** (2012) 055, arXiv:1112.2894 [hep-lat]. Version accepted for publication in JHEP. Discussions extended in sections 3.1 and 3.2, results unchanged. 19 pages, 7 figures, 3 tables.
- [17] C. Aubin and T. Blum *PoS LAT2005* (2006) 089, arXiv:hep-lat/0509064 [hep-lat].
- [18] M. Hayakawa, T. Blum, T. Izubuchi, and N. Yamada *PoS LAT2005* (2006) 353, arXiv:hep-lat/0509016 [hep-lat].
- [19] C. S. Fischer, T. Goecke, and R. Williams *Eur.Phys.J.* **A47** (2011) 28, arXiv:1009.5297 [hep-ph].
- [20] T. Goecke, C. S. Fischer, and R. Williams *Phys.Rev.* **D83** (2011) 094006, arXiv:1012.3886 [hep-ph].
- [21] T. Goecke, C. S. Fischer, and R. Williams *Phys.Lett.* **B704** (2011) 211–217, arXiv:1107.2588 [hep-ph]. 9 pages, 8 figures.
- [22] **Muon G-2 Collaboration** Collaboration, G. Bennett *et al.* *Phys.Rev.* **D73** (2006) 072003, arXiv:hep-ex/0602035 [hep-ex]. Summary of E821 Collaboration measurements of the muon anomalous magnetic moment, each reported earlier in Letters or Brief Reports. Revised version submitted to Phys.Rev.D.
- [23] B. Roberts *Chin.Phys.* **C34** (2010) 741–744, arXiv:1001.2898 [hep-ex].
- [24] M. E. Peskin and D. V. Schroeder, *An Introduction To Quantum Field Theory (Frontiers in Physics)*. Westview Press, 1995.
- [25] J. Aldins, T. Kinoshita, S. J. Brodsky, and A. Dufner *Phys.Rev.* **D1** (1970) 2378.
- [26] T. Aoyama, M. Hayakawa, T. Kinoshita, and M. Nio arXiv:1205.5370 [hep-ph].
- [27] A. Czarnecki, W. J. Marciano, and A. Vainshtein *Phys.Rev.* **D67** (2003) 073006, arXiv:hep-ph/0212229 [hep-ph].
- [28] K. Hagiwara, R. Liao, A. D. Martin, D. Nomura, and T. Teubner *J.Phys.G* **G38** (2011) 085003, arXiv:1105.3149 [hep-ph].
- [29] J. Bijnens, E. Pallante, and J. Prades *Nucl.Phys.* **B474** (1996) 379–420, arXiv:hep-ph/9511388 [hep-ph].
- [30] J. Bijnens, E. Pallante, and J. Prades *Phys.Rev.Lett.* **75** (1995) 1447–1450, arXiv:hep-ph/9505251 [hep-ph].
- [31] J. Bijnens, E. Pallante, and J. Prades *Nucl.Phys.* **B626** (2002) 410–411, arXiv:hep-ph/0112255 [hep-ph].

- [32] M. Hayakawa, T. Kinoshita, and A. Sanda *Phys.Rev.Lett.* **75** (1995) 790–793, arXiv:hep-ph/9503463 [hep-ph].
- [33] M. Hayakawa, T. Kinoshita, and A. Sanda *Phys.Rev.* **D54** (1996) 3137–3153, arXiv:hep-ph/9601310 [hep-ph].
- [34] M. Hayakawa and T. Kinoshita *Phys.Rev.* **D57** (1998) 465–477, arXiv:hep-ph/9708227 [hep-ph].
- [35] M. Hayakawa and T. Kinoshita arXiv:hep-ph/0112102 [hep-ph].
- [36] M. Knecht and A. Nyffeler *Phys.Rev.* **D65** (2002) 073034, arXiv:hep-ph/0111058 [hep-ph].
- [37] K. Melnikov and A. Vainshtein *Phys.Rev.* **D70** (2004) 113006, arXiv:hep-ph/0312226 [hep-ph].
- [38] J. Prades, E. de Rafael, and A. Vainshtein arXiv:0901.0306 [hep-ph].
- [39] L. von Smekal, A. Hauck, and R. Alkofer *Annals Phys.* **267** (1998) 1, arXiv:hep-ph/9707327 [hep-ph].
- [40] C. Fischer and R. Alkofer *Phys.Lett.* **B536** (2002) 177–184, arXiv:hep-ph/0202202 [hep-ph]. 11 pages, 4 figures Report-no: UNITUE-THEP-07/2002 Journal-ref: *Phys. Lett.* B536 (2002) 177.
- [41] J. C. Bloch *Few Body Syst.* **33** (2003) 111–152, arXiv:hep-ph/0303125 [hep-ph].
- [42] C. S. Fischer, A. Maas, and J. M. Pawłowski *Annals Phys.* **324** (2009) 2408–2437, arXiv:0810.1987 [hep-ph].
- [43] A. Aguilar, D. Binosi, and J. Papavassiliou *Phys.Rev.* **D78** (2008) 025010, arXiv:0802.1870 [hep-ph].
- [44] C. S. Fischer and R. Alkofer *Phys.Rev.* **D67** (2003) 094020, arXiv:hep-ph/0301094 [hep-ph].
- [45] C. S. Fischer, D. Nickel, and J. Wambach *Phys. Rev. D* **76** no. 9, (Nov, 2007) 094009.
- [46] C. S. Fischer, A. Maas, J. M. Pawłowski, and L. von Smekal *Annals Phys.* **322** (2007) 2916–2944, arXiv:hep-ph/0701050 [hep-ph].
- [47] C. Fischer, R. Alkofer, T. Dahm, and P. Maris *Phys.Rev.* **D70** (2004) 073007, arXiv:hep-ph/0407104 [hep-ph].

- [48] T. Goetze, C. S. Fischer, and R. Williams *Phys.Rev.* **B79** (2009) 064513, arXiv:0811.1887 [hep-ph].
- [49] C. S. Fischer and J. A. Mueller *Phys.Rev.* **D80** (2009) 074029, arXiv:0908.0007 [hep-ph].
- [50] C. S. Fischer, J. Luecker, and J. A. Mueller *Phys.Lett.* **B702** (2011) 438–441, arXiv:1104.1564 [hep-ph].
- [51] T. Moroi *Phys.Rev.* **D53** (1996) 6565–6575, arXiv:hep-ph/9512396 [hep-ph].
- [52] S. Heinemeyer, D. Stockinger, and G. Weiglein *Nucl.Phys.* **B699** (2004) 103–123, arXiv:hep-ph/0405255 [hep-ph].
- [53] D. Stockinger arXiv:0710.2429 [hep-ph].
- [54] V. P. Nair, *Quantum Field Theory A Modern Perspective*. Springer, 2005.
- [55] L. Faddeev and V. Popov *Phys.Lett.* **B25** (1967) 29–30.
- [56] L. Baulieu and J. Thierry-Mieg *Nucl.Phys* **B197** (1982) 477.
- [57] A. A. Slavnov *Theor. Math. Phys.* **10** (1972) 99–107.
- [58] J. C. Taylor *Nucl. Phys.* **B33** (1971) 436–444.
- [59] L. von Smekal, K. Maltman, and A. Sternbeck *Phys.Lett.* **B681** (2009) 336–342, arXiv:0903.1696 [hep-ph].
- [60] R. Alkofer and L. von Smekal *Phys. Rept.* **353** (2001) 281, arXiv:hep-ph/0007355.
- [61] C. S. Fischer *J. Phys.* **G32** (2006) R253–R291, arXiv:hep-ph/0605173.
- [62] R. Alkofer, M. Q. Huber, and K. Schwenzer *Comput.Phys.Commun.* **180** (2009) 965–976, arXiv:0808.2939 [hep-th].
- [63] A. Krassnigg, *Relativistic Bound states*, 2010.
- [64] E. E. Salpeter and H. A. Bethe *Phys. Rev.* **84** (1951) 1232–1242.
- [65] J. M. Cornwall, R. Jackiw, and E. Tomboulis *Phys. Rev.* **D10** (1974) 2428–2445.
- [66] J. Berges *AIP Conf.Proc.* **739** (2005) 3–62, arXiv:hep-ph/0409233.
- [67] J. Berges, S. Borsanyi, U. Reinosa, and J. Serreau *Annals Phys.* **320** (2005) 344–398, arXiv:hep-ph/0503240.
- [68] N. Nakanishi *Phys. Rev.* **138** no. 5B, (Jun, 1965) B1182–B1192.

- [69] A. Krassnigg *Phys. Rev. D* **80** (Dec, 2009) 114010, arXiv:0909.4016 [hep-ph].
- [70] P. Maris and P. C. Tandy *Phys.Rev.* **C61** (2000) 045202, arXiv:nuc1-th/9910033 [nuc1-th].
- [71] J. J. Sakurai *Annals Phys.* **11** (1960) 1–48.
- [72] Y. Nambu *Phys.Rev.Lett.* **4** (1960) 380–382.
- [73] S. Weinberg *Phys.Rev.Lett.* **18** (1967) 188–191.
- [74] S. R. Coleman, J. Wess, and B. Zumino *Phys.Rev.* **177** (1969) 2239–2247.
- [75] J. Callan, Curtis G., S. R. Coleman, J. Wess, and B. Zumino *Phys.Rev.* **177** (1969) 2247–2250.
- [76] H. Munczek *Phys.Rev.* **D52** (1995) 4736–4740, arXiv:hep-th/9411239 [hep-th].
- [77] P. Maris, C. D. Roberts, and P. C. Tandy *Phys. Lett.* **B420** (1998) 267–273, arXiv:nuc1-th/9707003.
- [78] Y. Nambu and G. Jona-Lasinio *Phys.Rev.* **122** (1961) 345–358.
- [79] Y. Nambu and G. Jona-Lasinio *Phys.Rev.* **124** (1961) 246–254.
- [80] S. L. Adler *Phys.Rev.* **177** (1969) 2426–2438.
- [81] M. S. Bhagwat, L. Chang, Y.-X. Liu, C. D. Roberts, and P. C. Tandy *Phys. Rev.* **C76** (2007) 045203, arXiv:0708.1118 [nuc1-th].
- [82] E. Witten *Nucl.Phys.* **B156** (1979) 269.
- [83] G. Veneziano *Nucl.Phys.* **B159** (1979) 213–224.
- [84] R. Alkofer, C. S. Fischer, and R. Williams *Eur.Phys.J.* **A38** (2008) 53–60, arXiv:0804.3478 [hep-ph].
- [85] J. B. Kogut and L. Susskind *Phys.Rev.* **D10** (1974) 3468–3475.
- [86] T. Umekawa, K. Naito, M. Oka, and M. Takizawa *Phys.Rev.* **C70** (2004) 055205, arXiv:hep-ph/0403032 [hep-ph].
- [87] J. Bell and R. Jackiw *Nuovo Cim.* **A60** (1969) 47–61.
- [88] J. S. Ball and T.-W. Chiu *Phys.Rev.* **D22** (1980) 2542.
- [89] P. Maris and P. C. Tandy *Phys.Rev.* **C60** (1999) 055214, arXiv:nuc1-th/9905056 [nuc1-th].

- [90] G. Eichmann.
- [91] V. Miransky *Phys.Lett.* **B165** (1985) 401–404.
- [92] P. Maris and C. D. Roberts *Phys.Rev.* **C56** (1997) 3369–3383, arXiv:nuc1-th/9708029 [nuc1-th].
- [93] R. Alkofer, C. S. Fischer, F. J. Llanes-Estrada, and K. Schwenzer *Annals Phys.* **324** (2009) 106–172, arXiv:0804.3042 [hep-ph].
- [94] P. C. Tandy *Prog.Part.Nucl.Phys.* **39** (1997) 117–199, arXiv:nuc1-th/9705018 [nuc1-th].
- [95] P. Maris and P. C. Tandy *Phys.Rev.* **C65** (2002) 045211, arXiv:nuc1-th/0201017 [nuc1-th].
- [96] M. Bhagwat and P. Maris *Phys.Rev.* **C77** (2008) 025203, arXiv:nuc1-th/0612069 [nuc1-th].
- [97] G. Eichmann, I. Cloet, R. Alkofer, A. Krassnigg, and C. Roberts *Phys.Rev.* **C79** (2009) 012202, arXiv:0810.1222 [nuc1-th].
- [98] G. Eichmann, R. Alkofer, A. Krassnigg, and D. Nicmorus *EPJ Web Conf.* **3** (2010) 03028, arXiv:0912.2876 [hep-ph].
- [99] H. Sanchis-Alepuz, G. Eichmann, S. Villalba-Chavez, and R. Alkofer *Phys.Rev.* **D84** (2011) 096003, arXiv:1109.0199 [hep-ph]. 9 pages, 4 figures, 3 tables.
- [100] G. Eichmann and C. Fischer *Eur.Phys.J.* **A48** (2012) 9, arXiv:1111.2614 [hep-ph].
- [101] G. Eichmann and D. Nicmorus arXiv:1112.2232 [hep-ph].
- [102] P. Maris and C. D. Roberts *Int.J.Mod.Phys.* **E12** (2003) 297–365, arXiv:nuc1-th/0301049 [nuc1-th].
- [103] D. Jarecke, P. Maris, and P. C. Tandy *Phys.Rev.* **C67** (2003) 035202, arXiv:nuc1-th/0208019 [nuc1-th]. Submitted for publication: 10x2-column pages, REVTEX 4, 3 .eps files making 3figs.
- [104] P. Maris *PiN Newslett.* **16** (2002) 213–218, arXiv:nuc1-th/0112022 [nuc1-th].
- [105] C.-R. Ji and P. Maris *Phys.Rev.* **D64** (2001) 014032, arXiv:nuc1-th/0102057 [nuc1-th]. 8 pages, 3 figures, Revtex.
- [106] S. R. Cotanch and P. Maris *Phys.Rev.* **D66** (2002) 116010, arXiv:hep-ph/0210151 [hep-ph].

- [107] G. Eichmann, R. Alkofer, A. Krassnigg, and D. Nicmorus *Phys.Rev.Lett.* **104** (2010) 201601, arXiv:0912.2246 [hep-ph].
- [108] G. Eichmann *Phys.Rev.* **D84** (2011) 014014, arXiv:1104.4505 [hep-ph]. 23 pages, 10 figures, 2 tables.
- [109] A. Krassnigg, *Talk given at Schladming Winterschool 2010*
http://physik.uni-graz.at/itp/iutp/iutp_10/talks/krassnigg.pdf.
- [110] **NA7 Collaboration** Collaboration, S. Amendolia *et al.* *Nucl.Phys.* **B277** (1986) 168.
- [111] H. Ackermann, T. Azemoon, W. Gabriel, H. Mertiens, H. Reich, *et al.* *Nucl.Phys.* **B137** (1978) 294.
- [112] P. Brauel, T. Canzler, D. Cords, R. Felst, G. Grindhammer, *et al.* *Z.Phys.* **C3** (1979) 101.
- [113] **Jefferson Lab F(pi) Collaboration** Collaboration, V. Tadevosyan *et al.* *Phys.Rev.* **C75** (2007) 055205, arXiv:nuc1-ex/0607007 [nuc1-ex].
- [114] **Jefferson Lab F(pi)-2 Collaboration** Collaboration, T. Horn *et al.* *Phys.Rev.Lett.* **97** (2006) 192001, arXiv:nuc1-ex/0607005 [nuc1-ex].
- [115] L. Barkov, A. Chilingarov, S. Eidelman, B. Khazin, M. Y. Lelchuk, *et al.* *Nucl.Phys.* **B256** (1985) 365–384.
- [116] C. Lerche and L. von Smekal *Phys.Rev.* **D65** (2002) 125006, arXiv:hep-ph/0202194 [hep-ph].
- [117] C. S. Fischer and R. Williams *Phys.Rev.* **D78** (2008) 074006, arXiv:0808.3372 [hep-ph].
- [118] C. S. Fischer and R. Williams *Phys.Rev.Lett.* **103** (2009) 122001, arXiv:0905.2291 [hep-ph].
- [119] A. Bashir, L. Chang, I. C. Cloet, B. El-Bennich, Y.-x. Liu, *et al.* arXiv:1201.3366 [nuc1-th].
- [120] A. Bender, C. D. Roberts, and L. Von Smekal *Phys.Lett.* **B380** (1996) 7–12, arXiv:nuc1-th/9602012 [nuc1-th].
- [121] J. C. Collins, *Renormalization. An Introduction to renormalization, the Renormalization Group, and the Operator Product Expansion*. Cambridge University Press, 1984.
- [122] E. de Rafael *Phys.Lett.* **B322** (1994) 239–246, arXiv:hep-ph/9311316 [hep-ph].

- [123] S. Eidelman, F. Jegerlehner, A. Kataev, and O. Veretin *Phys.Lett.* **B454** (1999) 369–380, arXiv:hep-ph/9812521 [hep-ph].
- [124] M. Gourdin and E. De Rafael *Nucl.Phys.* **B10** (1969) 667–674.
- [125] A. E. Dorokhov *Phys.Rev.* **D70** (2004) 094011, arXiv:hep-ph/0405153 [hep-ph].
- [126] C. Aubin, T. Blum, M. Golterman, and S. Peris arXiv:1205.3695 [hep-lat].
- [127] J. Aldins, T. Kinoshita, S. J. Brodsky, and A. Dufner *Phys.Rev.Lett.* **23** (1969) 441–443.
- [128] M. Knecht arXiv:hep-ph/0307239v1 [hep-ph].
- [129] D. Greynat and E. de Rafael arXiv:1204.3029 [hep-ph].
- [130] A. E. Dorokhov and W. Broniowski *Phys.Rev.* **D78** (2008) 073011, arXiv:0805.0760 [hep-ph].
- [131] A. Dorokhov, A. Radzhabov, and A. Zhevlakov *Eur.Phys.J.* **C71** (2011) 1702, arXiv:1103.2042 [hep-ph].
- [132] L. Cappiello, O. Cata, and G. D'Ambrosio *Phys.Rev.* **D83** (2011) 093006, arXiv:1009.1161 [hep-ph].
- [133] P. Bicudo, S. Cotanch, F. J. Llanes-Estrada, P. Maris, E. Ribeiro, and A. Szczepaniak *Phys.Rev.* **D65** (2002) 076008, arXiv:hep-ph/0112015 [hep-ph].
- [134] S. Weinberg *Phys.Rev.Lett.* **17** (1966) 616–621.
- [135] G. 't Hooft *Nucl.Phys.* **B72** (1974) 461.
- [136] E. Witten *Nucl.Phys.* **B160** (1979) 57.
- [137] A. Dorokhov, A. Radzhabov, and A. Zhevlakov arXiv:1204.3729 [hep-ph].
- [138] J. Wess and B. Zumino *Phys.Lett.* **B37** (1971) 95.
- [139] E. Witten *Nucl.Phys.* **B223** (1983) 422–432.
- [140] M. Frank, K. Mitchell, C. D. Roberts, and P. Tandy *Phys.Lett.* **B359** (1995) 17–22, arXiv:hep-ph/9412219 [hep-ph].
- [141] T. Feldmann, P. Kroll, and B. Stech *Phys.Rev.* **D58** (1998) 114006, arXiv:hep-ph/9802409 [hep-ph].
- [142] T. Feldmann, P. Kroll, and B. Stech *Phys.Lett.* **B449** (1999) 339–346, arXiv:hep-ph/9812269 [hep-ph].

- [143] A. Nyffeler *PoS CD09* (2009) 080, arXiv:0912.1441 [hep-ph].
- [144] T. Hahn *Comput.Phys.Commun.* **168** (2005) 78–95, arXiv:hep-ph/0404043 [hep-ph].
- [145] J. Bijnens and J. Prades *Z.Phys.* **C64** (1994) 475–494, arXiv:hep-ph/9403233 [hep-ph].
- [146] P. O. Bowman, U. M. Heller, D. B. Leinweber, M. B. Parappilly, A. G. Williams, *et al.* *Phys.Rev.* **D71** (2005) 054507, arXiv:hep-lat/0501019 [hep-lat].
- [147] C. S. Fischer, D. Nickel, and J. Wambach *Phys.Rev.* **D76** (2007) 094009, arXiv:0705.4407 [hep-ph].
- [148] T. Kinoshita, B. Nizic, and Y. Okamoto *Phys.Rev.* **D31** (1985) 2108.
- [149] P. Maris and C. D. Roberts *Phys.Rev.* **C58** (1998) 3659–3665, arXiv:nuc1-th/9804062 [nuc1-th].
- [150] A. Nyffeler *Phys.Rev.* **D79** (2009) 073012, arXiv:0901.1172 [hep-ph].
- [151] K. Osterwalder and R. Schrader *Commun.Math.Phys.* **31** (1973) 83–112.